This electronic thesis or dissertation has been downloaded from Explore Bristol Research, http://research-information.bristol.ac.uk

Author:
Gilroy, Emma R

Title:
Uranium-based Spintronics

General rights
Access to the thesis is subject to the Creative Commons Attribution - NonCommercial-No Derivatives 4.0 International Public License. A copy of this may be found at https://creativecommons.org/licenses/by-nc-nd/4.0/legalcode This license sets out your rights and the restrictions that apply to your access to the thesis so it is important you read this before proceeding.

Take down policy
Some pages of this thesis may have been removed for copyright restrictions prior to having it been deposited in Explore Bristol Research. However, if you have discovered material within the thesis that you consider to be unlawful e.g. breaches of copyright (either yours or that of a third party) or any other law, including but not limited to those relating to patent, trademark, confidentiality, data protection, obscenity, defamation, libel, then please contact collections-metadata@bristol.ac.uk and include the following information in your message:

- Your contact details
- Bibliographic details for the item, including a URL
- An outline nature of the complaint

Your claim will be investigated and, where appropriate, the item in question will be removed from public view as soon as possible.

Uranium-based Spintronics

Emma Rose Gilroy

University of Bristol
July 2020

A thesis submitted to the University of Bristol in accordance with the requirements for award of the degree of Doctor of Philosophy in the Faculty of Science, School of Physics.

31,844 Words

Abstract

Spintronics research often relies on the large spin-orbit coupling of heavy materials in conjunction with ferromagnetism to provide novel solutions for the next generation of computational memory and logic devices. The combination of these heavy metals with ferromagnets can provide low energy, efficient switching of magnetisation through the spin Hall effect and spin-orbit torque, or can result in interesting new chiral spin textures such as skyrmions through the interfacial Dzyaloshinskii-Moriya interaction. This thesis presents preliminary studies of uranium-based structures to evaluate the suitability of uranium for spintronics applications. Uranium is an interesting candidate for spintronic devices due to its large spin-orbit coupling and $5f$ electrons. Magnetometry, ferromagnetic resonance and transport measurements on bilayers systems unveiled oscillations in a number of magnetic properties, which likely arise from quantum well states in the uranium layer. The strength of these oscillations varies with the choice of ferromagnet and is likely a consequence of variations in the strength of $3d$-$5f$ orbital hybridisation. This thesis also introduces preliminary studies of dilute uranium alloys.

Declaration

I declare that the work in this dissertation was carried out in accordance with the requirements of the University's Regulations and Code of Practice for Research Degree Programmes and that it has not been submitted for any other academic award. Except where indicated by specific reference in the text, the work is the candidate's own work. Work done in collaboration with, or with the assistance of, others, is indicated as such. Any views expressed in the dissertation are those of the author.

SIGNED: .... DATE:..........................

Acknowledgements

I want to start by thanking my supervisors Chris Bell and Ross Springell for all the help, guidance, and encouragement they have given me over the course of this PhD. In particular, I would like to thank Chris for being so understanding throughout. I also want to thank Stephen Hayden, Sven Friedemann, and Anthony Carrington for the advice and wisdom shared with me.

Within the university there have been many staff members who have supported this work. Thank you to Andrew Murray for all his help in the cleanroom, and to all the technicians in the workshop for everything they have made and fixed for me. From the CMP-CDT, I want to thank Jude Laverock and Briony Spraggon for helping make the transition into postgraduate life so easy and enjoyable. I also want to thank all those within the IAC who have helped me and taught me so much during this project; Sophie, Dan, Ellie, Joe, Lottie and Ed. Thank you also to Jason in the School of Chemistry for his help with the EPR system.

Within CES and and the CDT-CMP there are many people I would like to thank for more than just their scientific contributions. A huge thank you to Maud for being wonderful friend and climbing partner - even when I drop you. A special mention as well to Owen for providing friendship, support and endless memes when we should both be working. Thank you to Lauren and Richard for all your wonderful company from the start of the CDT and beyond. To Matt for all his support, wisdom and advice throughout, to Harry for his helpful suggestions and sharing his knowledge with me and to Alice and Sara for being some of the most wonderful, welcoming people and helping me through so much. And a big thank you to all my friends who have helped keep my spirits up along the way: Joe, Torsten, Jarrod, Jake, Paolo, Mara, Israel, and Alex.

I want to extend my gratitude to my friends outside of physics who have kept me sane and grounded, including, but in no way limited to, Eve, Jo, and Emily.

Thank you to my family for all your support. To my Dad, Mum, and Gran for always looking after me and encouraging me in everything I do. A special thank you to my Grandpa, whose belief in me was unwavering and who always knew this is where I would end up even before I did.

Finally, I want to thank Ewan for everything he has done to help and support me over the last three years, including putting up with me when I'm not always so fun to be around and, most importantly, making sure I am fed. You've always believed in me even when I don't always believe in myself.

Contents

Chapter 1

Introduction

Spin electronics, or spintronics, are devices which utilise the spin of the electron rather than the charge. These devices have played an integral role in the development of technology due to the dual nature of the z component of electron spin, which is highly suited for use with the binary machine code on which computers run. The stable, yet easy to manipulate, character of magnetic materials resulted in spintronics becoming a cornerstone in the development of computer memory. The 1980s saw the discovery of giant magnetoreisistance [1, 2], oscillatory exchange coupling [3–5], and perpendicular magnetic anisotropy in thin film structures [6] which have revolutionised hard drive technology over the last three decades, with GMR-based read heads which benefited from increased sensitivity being introduced in 1997 [1] [7] and the perpendicular magnetic recording hard drive first appearing in 2005 [8]. The implementation of these resulted in a reduction of the physical size of the drive while increasing the capacity of the magnetic hard disk drive, with the introduction of perpendicular magnetic recording alone increasing the areal density from $70\,\text{megabit}\,\text{mm}^{-2}$ to $206\,\text{megabit}\,\text{mm}^{-2}$ between subsequent releases from Toshiba [8].

The field of spintronics continues to evolve and is constantly exploring novel ways to improve the speed and efficiency of storage technology [9] as well as challenging the fundamental architecture of the standard computer by expanding into logic processes and even potentially integrating logic and memory into a single device [10]. There are many aspects of spintronics; spin-torque driven devices, magnonics, spin caloritronics, topological spin textures, silicon-based spintronics, and topological insulator spintronics to name just a few [9–11]. A number of these research areas often focus on combining thin films of ferromagnetic materials with metals

---

[1] While GMR-based heads were incredibly important to the evolution of the hard drive, they were subsequently replaced with the tunnelling magnetoresistance (TMR) head in 2004.

which have a large spin-orbit coupling, such as platinum and palladium, as this can enhance the desired behaviour of the device. For example, thin film structures which incorporate these materials benefit from the increased ability to produce and detect spin currents for efficient switching of magnetisation or movement of domain walls within the ferromagnetic layer [10].

However, the interface between a ferromagnet and a normal metal can behave in unexpected manners. For example, it has been well documented that growth of a normal metal on a ferromagnet can result in an induced magnetic moment in the non-magnetic metal due to magnetic proximity effects. The presence of such induced magnetic moments in the normal metal can have undesirable consequences for spintronic applications [12]. Therefore, it is crucial to understand the interfacial physics between ferromagnetic and heavy metal thin films in addition to the spin-orbit related phenomena. The question then becomes, is it possible to understand and separate the roles of the magnetic proximity effects and the spin-orbit coupling?

In this thesis, uranium is studied as an alternative to traditional heavy metals. This choice, while unusual, is motivated by a number of factors. As uranium is the heaviest naturally occurring element it is expected to have a proportionally large spin-orbit coupling, which makes it interesting for spintronic research. Additionally, the $5f$ electron states within uranium may introduce unusual and unexpected aspects to the well documented phenomena in $5d$ materials. While there has been little previous exploration into U/FM systems, the research which has been carried out provides yet more justification for this unconventional choice. These previous studies discovered that for U/Fe multilayers an induced magnetic moment is present within the uranium layers [13]. On the other hand, no moment was detected for Ni or Co based structures [14]. This dependence of the induced moment on the ferromagnet makes uranium as an interesting material to answer the question set out above. By comparing and contrasting the behaviour of U/Fe and U/Ni, it may be possible to disentangle a large spin-orbit coupling contribution from the induced magnetic moments.

This thesis will primarily focus on the magnetic behaviour of U/FM bilayer systems, explored using three main techniques. For each technique, a series of systematic measurements as a function of uranium thickness are carried out. In addition to the bilayer measurements, this work includes some preliminary data on the magnetic properties of metals containing uranium impurities. This thesis will be laid out as follows;

To begin, chapter 2 will introduce relevant background theory for concepts in magnetism important for this work as well as a brief look at the existing relationship between uranium and magnetism. In chapter 3, the growth of both bilayer and alloy samples by the process of DC magnetron sputtering is detailed. Additionally, this chapters discusses the x-ray techniques used for characterisation of the samples. Chapter 6.13 aims to understand the anisotropy of both Fe/U and Ni/U thin films and its evolution with uranium thickness through vibrating sample magnetometry. Studies of the anisotropic magntoresistance of the bilayer samples can be found in chapter 5. This chapter includes a short discussion of the theory behind anisotropic magnetoresistance, details of the fabrication process for patterning and etching of the thin films, as well as a comparison of the results from Fe/U and Ni/U. The magnetisation dynamics of the Ni/U bilayers were investigated through ferromagnetic resonance. The details and results of these studies are presented in chapter 6. Finally, chapter 7 introduces dilute alloy systems. This chapter presents preliminary measurements of Cu and Ni thin films alloyed with low percentages of U, obtained through transport and ferromagnetic resonance studies.

Chapter 2

Theory and Background

2.1 Magnetism

Typically, a magnetic material consists of ordered magnetic moments. Classically, a magnetic moment μ can be thought of as a charge current around a loop of area **dS** and is given by

$$\boldsymbol{\mu} = I \int \mathbf{dS}. \tag{2.1}$$

For an orbiting electron, the magnetic moment is related to the its angular momentum **L** by

$$\mu = \gamma \mathbf{L}, \tag{2.2}$$

where γ is the gyromagnetic ratio which is given by $\gamma = g\mu_B/\hbar$, with g being the g-factor and $\mu_B = e\hbar/2m_e$ is the Bohr magneton. When an external magnetic field is applied to a magnetic moment, the energy of the system can be described by the Zeeman energy,

$$E_{\mathrm{Z}} = -\boldsymbol{\mu} \cdot \mathbf{B}. \tag{2.3}$$

This results in the magnetic moment aligning with the field direction in order to minimise this energy [15]. However, magnetism cannot be fully described using just the classical picture. An electron is inherently quantum mechanical in nature and has an intrinsic angular momentum, known as *spin*, in addition to its orbital angular momentum. This intrinsic angular momentum results in an intrinsic magnetic moment

$$\mu = -g\mu_B m_s, \tag{2.4}$$

where $m_s = \pm 1/2$ depending whether the electron is *spin up* or *spin down.* The Zeeman energy then becomes dependent on the electron spin

$$E_{\mathrm{Z}} = g\mu_B m_s B. \tag{2.5}$$

This results in the splitting of the spin up and spin down bands in the density of states. Spins which are moved above the Fermi level E_F then flip to occupy empty states, resulting in a magnetisation in the majority spin direction. This is known as paramagnetism.

In a ferromagnet, the moments are aligned parallel to one another despite the absence of an applied magnetic field. This results in a spontaneous magnetisation $\mathbf{M}$ which is the magnetic moment per unit volume. This spontaneous ordering can be related to an internal exchange field, which is analogous to the applied field in paramagnetism, known as the Weiss field [16],

$$\mathbf{B}_{\mathrm{Ex}} = \lambda \mathbf{M}, \tag{2.6}$$

where λ is a constant which is material dependent. This constant is essentially a measure of the orbital overlap. The energy of this exchange interaction is given by the Heisenberg Hamiltonian

$$\varepsilon_{\mathrm{Ex}} = -\sum_{ij} J_{ij} \mathbf{S}_i \cdot \mathbf{S}_j, \tag{2.7}$$

where J_{ij} is the exchange constant and $\mathbf{S}_{i,j}$ are spins at sites i and j respectively. When J_{ij} is positive (negative) the spins are ordered ferromagetically (antiferromagetically).

In the band structure picture, the exchange field results in the splitting of the spin up and spin down states of the ferromagnet without the applied field required in the paramagnetic case. This is illustrated in fig.2.1. The splitting of the spins is important as the position of the bands at the Fermi energy can result in a variety of behaviours. For example, if the spin up band in fig.2.1 were to sit below the Fermi energy only electrons in the spin down orientation would participate in conduction. Materials which exhibit this behaviour are known as half metals. The splitting of spin bands in the density of states also results in a spin polarisation at the Fermi level. Referring again to the picture presented in fig.2.1, there is a negative polarisation at the Fermi energy, despite a majority of spins being in the up orientation. This is related to the position of the bands with respect to the Fermi energy, i.e. the Fermi energy cuts through a larger section of the spin down band than the spin up band.

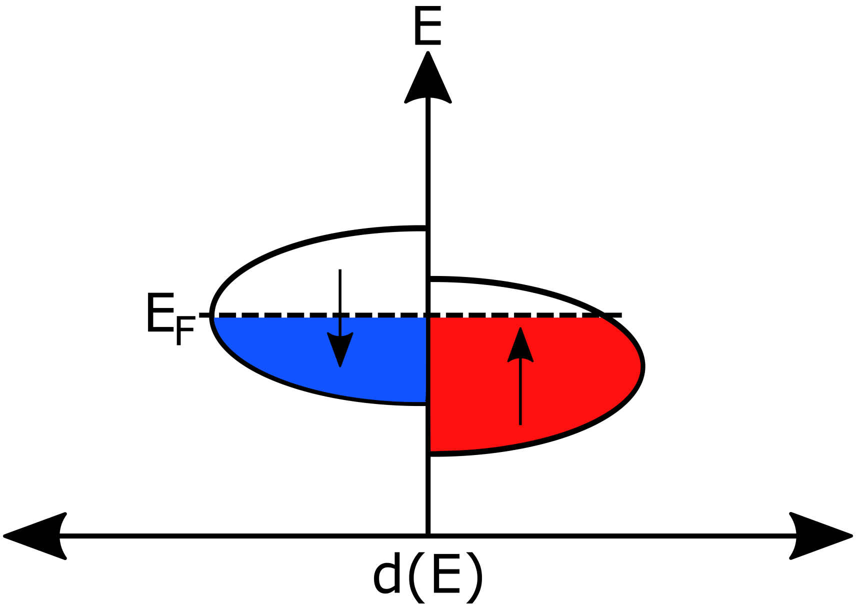

Figure 2.1: Representation of the spontaneous splitting of the spin up and down d bands in a ferromagnet. Having a majority of spins in one band results in a net magnetisation. In this picture, the majority of spins are in the up band, but the net polarisation at the Fermi energy is spin down.

2.1.1 Magnetic Anisotropy

In a magnetic material, the magnetisation tends to lie along a preferred direction, known as the *easy axis*. There is also a corresponding *hard axis* along which it is energetically unfavourable for the magnetisation to lie. This is known as magnetic anisotropy. There are many contributions to the magnetic anisotropy energy depending on the structure of the systems. In this thesis, the magnetic anisotropy of the uranium/ferromagnet systems is extensively studied. It is therefore important to understand the various phenomena which can contribute to the magnetic anisotropy energy.

2.1.1.1 Magnetocrystalline Anisotropy

In crystalline structures, the axes of magnetic anisotropy may correspond to one of the crystallographic directions which is known as *magnetocrystalline anisotropy* [17]. This form of anisotropy is a consequence of the spin-orbit interaction. In a crystal, the electron orbitals are associated with the crystal's structure. The spin-orbit coupling then causes the spins to align along specific crystal axes [18]. There are a number of distinct types of magnetocrystalline anisotropy, with the two most common being the *uniaxial anisotropy* and *cubic anisotropy*.

In the unaxial case, the magnetocrystalline energy density is given by

$$\varepsilon_u = K_{u1}\sin^2(\theta) + K_{u2}\sin^4(\theta) + K_{u3}\sin^6(\theta) + \cdots , \tag{2.8}$$

where K_{ui} are the anisotropy coefficients, and θ is the angle between the direction of magnetisation and the easy axis. Often this can be simplified to the first two terms,

$$\varepsilon_u = K_{u1}\sin^2(\theta) + K_{u2}\sin^4(\theta). \tag{2.9}$$

The most common example used to illustrate uniaxial magnetocrystalline anisotropy is cobalt. Cobalt has a hexagonal structure with its easy direction of magnetisation generally aligned along the *c*-axis.

The energy in a cubic system is described in terms of the direction cosines α_x,α_y, and α_z of the magnetisation with respect to the co-ordinate axes of the crystal, usually defined as the cube edges,

$$\varepsilon_c = K_{c1}(\alpha_x^2\alpha_y^2 + \alpha_y^2\alpha_z^2 + \alpha_z^2\alpha_x^2) + K_{c2}(\alpha_x^2\alpha_y^2\alpha_z^2) + \cdots , \tag{2.10}$$

with K_{ci} being a cubic anisotropy coefficient. Again this tends to be simplified to just the first two terms. The ratio and signs of K_{c1} and K_{c2} can reveal which of the three principle directions [100], [110], and [111] contains the easy axis of magnetisation in the crystal [19]. Both iron and nickel exhibit cubic anisotropy.

In a thin film system, epitaxial growth results in a single crystal layer which has a distinct orientation. In a magnetic film, this ordering results in a magnetocrystalline anisotropy.

2.1.1.2 Shape Anisoptropy

Another important contribution to the anisotropy energy comes from the *shape anisotropy.* When there are discontinuities in the magnetisation of a sample, i.e. at the sample edges, there is an opposing demagnetisation field $\mathbf{H}_d$ produced, as $\nabla \cdot \mathbf{H} = -\nabla \cdot \mathbf{M}$. As the name suggests, this is a term related to the shape of the sample and the associated demagnetisation energy is given by

$$E_{\mathrm{D}} = -\frac{\mu_0}{2}\int_V \mathbf{M}\cdot\mathbf{H}_d\, d\tau. \tag{2.11}$$

For thin films, the demagnetisation energy becomes [20]

$$E_D = \frac{1}{2}\mu_0 M^2 \cos^2 \phi, \tag{2.12}$$

where ϕ is the angle between the the magnetisation vector and the normal of the sample. This demagnetisation energy is large for the case of perpendicular magnetisation. As a result of this high energy cost, the magnetisation of a magnetic thin film tends to lie in-plane.

2.1.1.3 Interfacial Anisotropy

In thin film systems, often the magnetisation lies in the plane of the sample, as this tends to be energetically most favourable. However in ferromagnet/normal metal heterostructures, it is possible to pull the magnetisation out-of-plane. This is known as perpendicular magnetic anisotropy (PMA). This phenomenon was widely observed in the 1980s, with systems such as Co/Cr [21], Co/Pd [22,23] and Co/Pt [24] systems exhibiting easy axis behaviour in the out-of-plane direction. In these multilayers the Co layer was required to be thin[1], <8 Å in the Co/Pd case [22]. This switch from in-plane to out-of-plane magnetisation is due to an interfacial, or surface, anisotropy. The anisotropy energy of thin film system with surface anisotropy takes the form

$$E_{\mathrm{surface}} = K \sin^2 \phi, \tag{2.13}$$

as it acts like an effective uniaxial anisotropy. Here, ϕ is the angle between the normal of the plane and the magnetisation vector and K is an effective anisotropy coefficient which encompasses the many components of anisotropy present within the system:

$$K = \frac{2K_s}{t} + K_v - \mu_0 M^2. \tag{2.14}$$

The first term is related to the surface anisotropy, with K_s being the surface anisotropy coefficient and where t is the film thickness. The second term is relating to the anisotropy which dominates in the samples volume, such as magnetocrystalline anisotropy. The third term is the shape anisotropy term.

While PMA is commonly associated with Co, it is also present in other ferromagnetic multilayers, such as iron [6, 25]. Draaisma *et al.* suggest that in Pd/Fe systems that at low Fe thicknesses there is a tendency towards perpendicular magnetisation [6]. In their work,

---

[1] It should be noted that this blanket statement may not be true in the case of Co/Cr as the thickness of the samples was not mentioned in ref. [21].

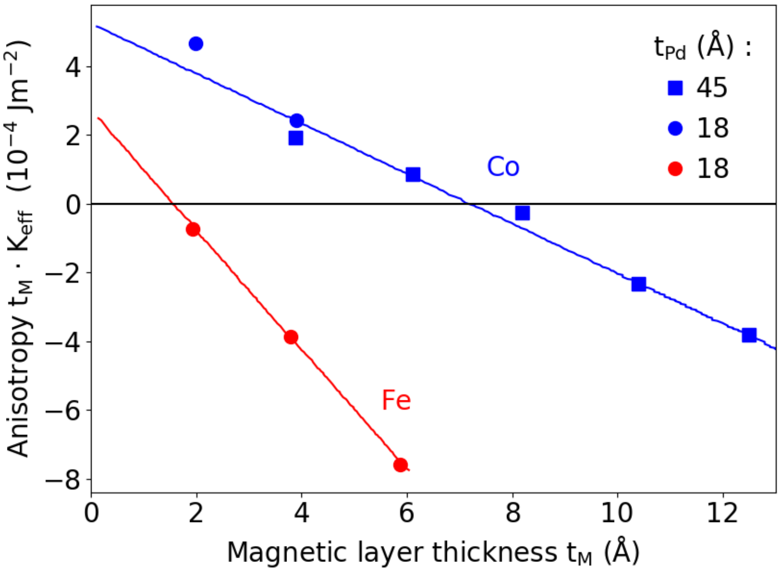

Figure 2.2: Effective anisotropy of Co/Pd and Fe/Pd thin films. At low thicknesses, the magnetisation shifts from a dominant volume contribution to a primarily surface anisotropy. Adapted from ref. [6]

it was suggested that the volume anisotropy contribution favours in-plane magnetisation and the surface term favours out-of-plane. As the thickness of the ferromagnetic layer decreases, the surface term dominates pulling the magnetisation perpendicular to the film plane. This is illustrated by fig.2.2. For both Fe and Co as the thickness of the magnetic layer is decreased, there is a switch from negative to positive anisotropy, which corresponds to a shift from in-plane to out-of-plane[2].

2.1.1.4 Induced Anisotropy

The process by which thin films are grown can often introduce another type of anisotropy unique to the growth conditions, known as *induced anisotropy.* One such condition which can induce magnetic anisotropy is the presence of external magnetic fields during growth [26, 27]. This induced anisotropy takes the form of a uniaxial anisotropy,

$$E_{\text{ind}} = K_{\text{ind}} \sin^2 \theta, \tag{2.15}$$

where θ is the angle between the magnetisation and the field applied during deposition [26].

---

[2] In fig.2.2 there are no Pd/Fe samples tested which exhibit PMA and its presence is suggested based on the Co case. However in ref. [25], PMA was observed for Au/Fe/Au sandwiches at Fe<3 monolayers.

Another source of induced magnetic anisotropy comes from the angle of incidence of ferromagnetic atoms relative to the substrate on which they are grown. When atoms are deposited at an off-normal – or oblique – angle of incidence a uniaxial like anisotropy can be observed [28–32].

2.1.2 Dzyaloshinskii-Moriya Interaction

The Dzyaloshinskii-Moriya interaction (DMI) is an antisymmetric exchange interaction arising from broken inversion symmetry and spin orbit coupling [33–35]. The energy of this interaction is given by

$$E_{\text{DMI}} = \sum_{ij} \mathbf{D}_{ij} \cdot \mathbf{S}_i \times \mathbf{S}_j, \tag{2.16}$$

where $\mathbf{D}_{ij}$ is the Dzyaloshinskii-Moriya vector. This term causes canting of spins away from the direction of alignment, which can result in the twisting of spins into chiral structures. These structures can be twists in single chains of spins, known as helicoids, or more complex structures such as skyrmions.

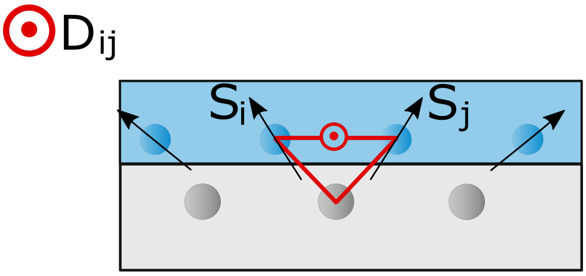

Figure 2.3: Schematic of the interfacial Dzyaloshinskii-Moriya iteraction. The grey underlayer has large spin-orbit coupling which induces an anti-symmetric exchange term. This results in a canting of spins in the magnetic layer (blue) which can form chiral spin textures. The interfacial DMI vector lies parallel to the interface.

In thin films, inversion symmetry is broken due to the presence of an interface. Growing a magnetic thin film adjacent to a non-magnetic material with large spin-orbit coupling can give rise to the interfacial Dzyaloshinskii-Moriya interaction (IDMI) [36], illustrated in fig.2.3. In this thin film picture, the interaction is mediated by the non-magnetic atoms with large spin orbit coupling and is restricted to the region surrounding the interface [37]. The presence of perpendicular magnetic anisotropy within the FM layer is preferred in literature [37, 38] but is not a requirement as it can be observed with in-plane magnetisation [39]. Additionally, it does not depend on the structure of the FM layer, i.e. DMI can be observed in both single crystal and polycrystalline structures [40].

Interfacial spin textures have been imaged using spin polarised scanning tunnelling microscopy [41, 42]. However, the strength of the DM interaction cannot be measured using this technique. Through Brillouin light scattering (BLS) the strength of the interfacial DM interaction can be determined. The presence of DMI within a thin film results in an asymmetric spin wave dispersion [43, 44]. In BLS, Stokes and anti-Stokes peaks, which correspond to the creation and destruction of magnons respectively, result from the propagation of spin waves in opposite directions along the surface of the film [39]. Due to the asymmetry of the spin wave dispersion as a result of IDMI, an asymmetry is subsequently observed in the BLS spectrum. The difference in frequency Δf of the spin waves propagating in opposite directions can then be directly related to the strength of the DM interaction,

$$\Delta f(k) = \frac{2\gamma}{\pi M_s} D_{i,j} k. \tag{2.17}$$

The structure of the film can have important effects on the DMI. When a FM is sandwiched between two identically thick heavy metal (HM) layers, the DMI vector is equal and opposite at each interface, resulting in no interfacial DMI. As a result of this, asymmetric structures tend to be selected when studying IDMI. The thickness of both the FM and HM layers can also influence the DMI. As the thickness of the ferromagnetic layer increases, the strength of the DM interaction is expected to decrease [45]. For the heavy metal layer, it was found that in the case of Pt, the DMI strength increases and then saturates as thickness increases [46].

2.1.3 Ferromagnetic Resonance

In addition to the magnetostatics discussed above, it is also important to understand the dynamics of spins. Ferromagnetic resonance (FMR) is a phenomenon analogous to nuclear magnetic resonance and electron paramagnetic resonance and can be used to understand these spin dynamics within a sample. When a magnetic field $\mathbf{H}_{\text{eff}}$ is applied to a ferromagnet, the magnetization feels a torque

$$\frac{d\mathbf{M}}{dt} = -\gamma \mathbf{M} \times \mathbf{H}_{\text{eff}}, \tag{2.18}$$

which causes precession of the magnetic moment around the direction of the magnetic field. This magnetic field $\mathbf{H}_{\text{eff}}$ contains terms relating to the applied magnetic field, demagnetising field, and magnetic anisotropy. This precession has frequency

$$\omega = \gamma B, \tag{2.19}$$

which is known as the *Lamour precession* frequency. However, this is not sufficient to describe resonance in the presence of an additional applied electromagnetic field.

In 1946, Griffiths observed peaks in $\mu\rho$ (the product of electrical resitivity with the materials magnetic permeability) when a microwave field was applied to Ni, Fe and Co thin films in addition to the external magnetic field [47]. The position of these peaks was found to shift in field as the wavelength of the microwave field was changed and were attributed to resonant absorption by the magnetic moments. However, the resonant frequency could not be obtained through eqn.2.19. Kittel derived a condition for resonance which closely matched the experimental results of Griffiths [48, 49]

$$\omega_{res} = \gamma(BH)^{1/2}. \tag{2.20}$$

While this was able to describe the work of Griffiths, the derivation of this equation does not include any effects from damping or anisotropy. Eqn.2.20 is also specific for a thin film, as the derivation is dependent on the demagnetisation factor [48, 49].

In real systems, a damping term must be included. Eqn.2.18 then becomes

$$\frac{d\mathbf{M}}{dt} = -\gamma \mathbf{M} \times \mathbf{H}_{\text{eff}} + \frac{\alpha}{M_s} \mathbf{M} \times \frac{d\mathbf{M}}{dt}. \tag{2.21}$$

This is known as the Landau-Lifshitz-Gilbert equation. Here α is the damping factor, given as $G/\gamma M$, where G is the Gilbert damping coefficient. Using this, Suhl defined a more rigorous equation for the resonant frequency [50],

$$\omega_{res} = \frac{\gamma}{M \sin\theta} \left[\frac{\partial^2 E}{\partial \theta^2} \frac{\partial^2 E}{\partial \phi^2} - \left(\frac{\partial^2 E}{\partial \theta \partial \phi} \right)^2 \right]^{1/2}. \tag{2.22}$$

In ferromagnet/normal metal systems, an increase in the damping parameter is observed when compared with the damping in a bulk ferromagnetic sample. This is a result of *spin pumping*. As the magnetisation of the ferromagnet precesses, there is a transfer of spins across the interface into the normal metal. By emitting a spin current, the torque on the magnetisation vector is increased, resulting in enhanced damping [51]. The spin current $\mathbf{I}_s$ flowing into the normal metal can be defined as

$$\mathbf{I}_s = \frac{\hbar}{4\pi} g_{\uparrow\downarrow} \mathbf{M} \times \frac{d\mathbf{M}}{dt}, \tag{2.23}$$

where $g_{\uparrow\downarrow}$ is the spin mixing conductance [52].

As the spins are pumped into the normal metal, they can undergo scattering. This can result in flipped spins re-entering the ferromagnet and induces additional damping. In materials with

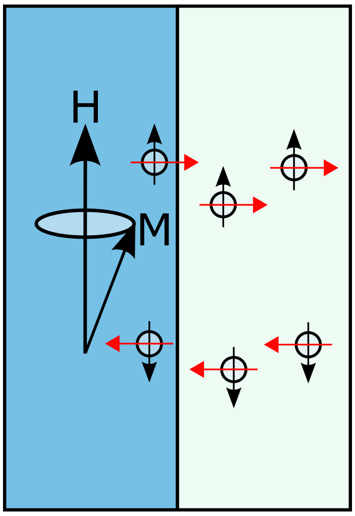

Figure 2.4: Representation of spin pumping across a ferromagnet/normal metal interface. The magnetisation M precesses around the direction of the magnetic field H and spins are transferred from the ferromagnet into the normal metal. Within the normal metal, the spin may undergo spin flip scattering. Flipped spins may flow back into the ferromagnet, damping the precession of M. Black arrows represent spin orientation while red arrows indicate direction of travel.

a long spin coherence length, such as copper, the damping will be much lower than in materials where spin-flip scattering is prevalent, such as heavy metals like platinum. The backflow of spin current is given by

$$\mathbf{I}_s^b = \frac{g_{\uparrow\downarrow}}{2\pi N}[\mathbf{s} - \mathbf{M}(\mathbf{M}\cdot\mathbf{s})], \tag{2.24}$$

where N is the one spin DOS and $\mathbf{s}$ is the spin excess [52]. This process is illustrated in fig.2.4.

2.1.4 Spintronics

Spintronic devices utilise the spin degree of freedom and for many years have played an important role in the storage of information due to their binary nature. Typically, these kind of devices are used as read heads in magnetic storage, but may also lead to novel storage concepts such as domain wall racetrack memory [53]. Current research may also allow spintronics to move from being solely for information storage and towards utilisation in logic operations [54], and neural networks [55].

2.1.4.1 Giant Magnetoresistance and Oscillatory Interlayer Exchange Coupling

In 1988 and 1989, two papers were published demonstrating an interesting magnetic property observed in Fe-Cr superlattices [1, 2]. In the paper by Baibich *et al.*, low temperature magnetoresistance measurements were used to study the change in resistance with field for multiple samples. For samples with antiferromagnetic alignment between magnetic layers, the resistance was found to be a factor of two larger than for the parallel alignment [1]. This phenomenon was dubbed *Giant Magnetoresistance* (GMR). Binasch *et al.* observed the same phenomenon at room temperature, with the change in resistance due to anti-parallel alignment on the order of 1.5% [2].

This increase in resistance has been attributed to the relationship between the direction of the conduction electron spin and the magnetisation direction of the ferromagnetic layers. This can be easily described by a trilayer *spin valve* picture. In a spin valve, one magnetic layer has a fixed magnetisation orientation, while the other is free to flip. As electrons pass through the fixed layer they undergo polarisation and align with the direction of magnetisation. When the two ferromagnetic layers are parallel, the electrons can easily flow into the free magnetic layer, resulting in a low measured resistance. Conversely, layers are aligned anti-parallel, electrons spin-polarised in the fixed layer direction will strongly scatter at the interface of the free magnetic layer, yielding a much higher resistance.

Later, it was observed that the coupling of magnetisation between layers oscillates with non-magnetic spacer thickness [3–5]. These oscillations could be seen in the change in magnetoresistance $\Delta R/R$ and were mirrored in the saturation field H_s determined by magnetometry [3]. These oscillations were observed in a number of different metals [5], with the period of oscillation being related to the spacer metal, as seen in fig.2.5. In some cases, two coinciding oscillations can be observed, one with a short period and one with a longer period [56].

This type of oscillation was initially attributed to an RKKY like interaction, as the interfaces could be treated as coupled magnetic impurities [57]. However, simple RKKY arguments were insufficient to describe this oscillation as it often underestimated the period of the oscillation and coupling strength in transition metal based systems [3, 57, 58]. More complex RKKY-based theories had more success and were able to correctly predict the oscillation period in noble metals such as copper and gold [59], but failed for materials with more complex Fermi surfaces [60]. In order to describe these oscillations, quantum well states (QWS) were introduced as a potential solution. Typically, QWS are associated with semiconductor physics but they are also present in metallic thin films. These quantum well states occur due to confinement of the electrons in the z direction due to the interface between materials. This causes quantisation

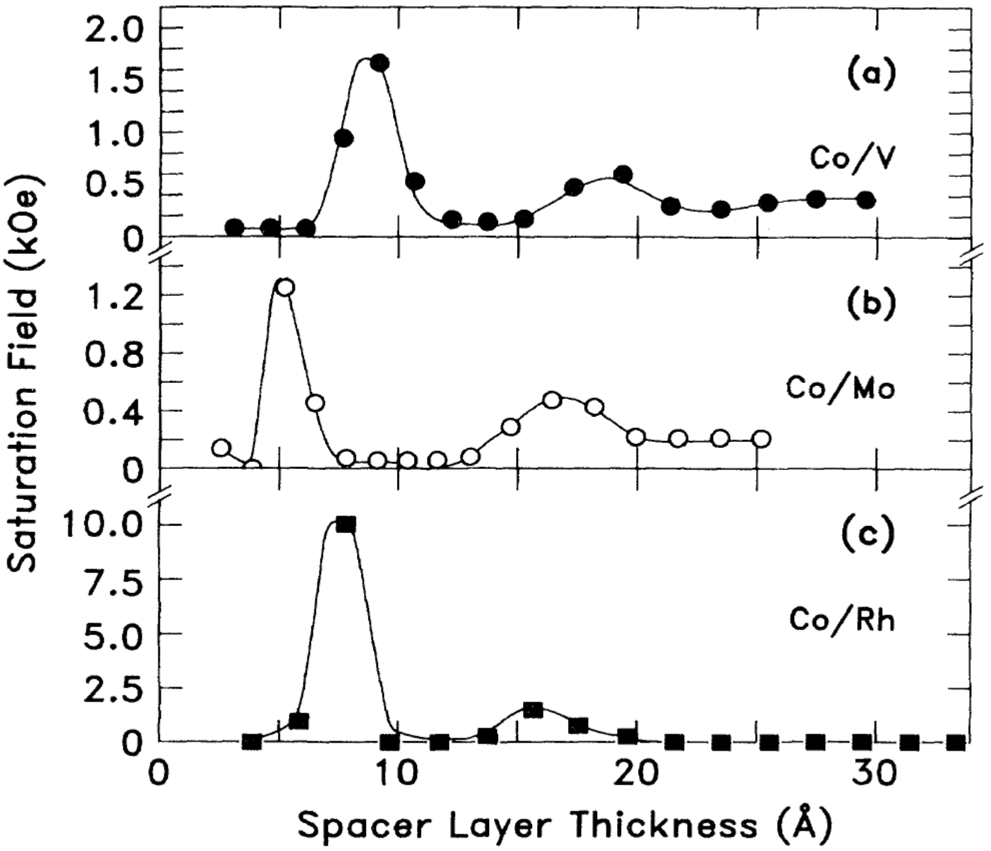

Figure 2.5: Oscillatory behaviour of the saturation field for Co/V, Co/Mo and Co/Rh multilayer systems. This oscillation represents the switching between parallel and anit-parallel alignment of the magnetic layers. Taken from ref. [5].

of the momentum of bands in the direction perpendicular to the interface [61]. Due to the boundary conditions imposed by the interfaces, standing waves are formed. These standing waves are Bloch waves which are modulated by an envelope wave function [62]. A common analogy used to understand QWSs is the Fabry-Perot interferometer. In the interferometer, subsequent maxima are seen when the spacing between plates is increase by $\lambda/2$. This is also true for thin films. By increasing the thickness of the film by $\lambda/2$ the wavefunction will once again fit [63]. The spacing in energy of the quantum well states is inversely related to the thickness of the layer in which they are confined, i.e. the spacing between QWSs increases with decreasing film thickness [61]. Therefore, as the thickness is increased, different quantised states will pass through the Fermi energy, which produces a change in the density of states at E_F. The work of Ortega and Himpsel studied quantum well states in Co/Cu bilayers systems [62]. They observed oscillations in the inverse-photoemission intensity due to changes in the DOS caused by QWSs crossing the Fermi surface, seen in fig.2.6. These oscillations had a period similar to that observed in exchange coupling for Co/Cu systems. Oscillations were also seen in Fe/Au systems [62, 63]. However, there was no coupling seen by Parkin in gold-based multilayers – along with other heavy metals such as Pd, Ag, P,t and Hf. However, later work observed coupling in Co/Pt systems which exhibited PMA [64], suggesting that the orientation of the magnetisation plays a role in the exchange coupling. Work by Tomaz *et al.* confirmed this as variations in coupling were observed between the (110), (211), and (110) orientations of Fe in Fe/Cr multilayers [65].

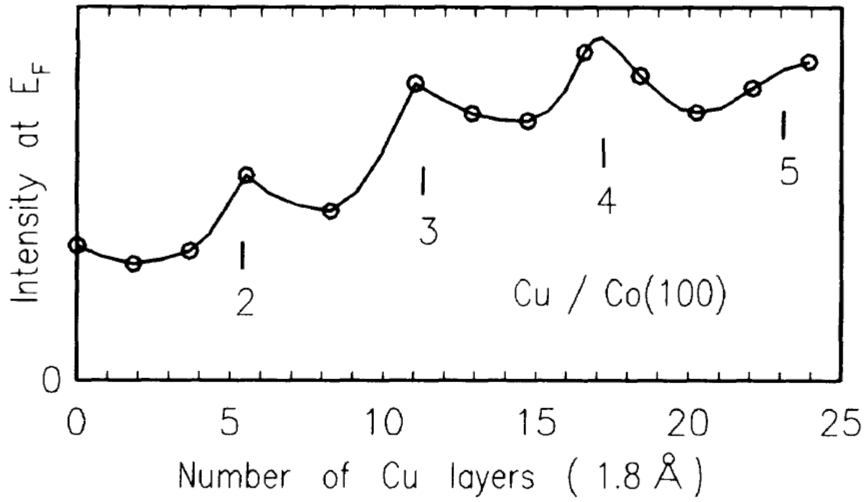

Figure 2.6: Evidence of quantum well states in Cu/Co bilayers from inverse photoemission measurements. The period of oscillation is in agreement with the period of the oscillatory exchange coupling of Cu/Co superlattices. Taken from ref. [62].

Based on semiconductor physics, an expression for the period of the oscillations P was determined by Himpsel and Ortega [62, 63]

$$P = \frac{k_{\mathrm{BZB}}}{k_{\mathrm{BZB}} - k_{\mathrm{F}}} d, \tag{2.25}$$

where k_{BZB} is the Brillouin zone boundary wave vector, k_{F} is the Fermi wave vector, and d is the layer spacing. More complex calculations have since been used to determine the period of oscillations[3] [60, 66]. The theory of QWSs in FM/NM can also accurately describe both the long and short periods that were observed experimentally. These two periods correspond to

---

[3] Often these more involved calculations also include additional terms such as bilinear and biquadratic coupling [57, 60].

wave vectors spanning different parts of the Fermi surface of the given metal [57].

While quantum well states clearly mirror the oscillation period of the interlayer exchange coupling, it is not obvious how this can alter the coupling between ferromagnetic layers. It was suggested by Himpsel *et al.* that in greater than bilayer systems, having a high DOS state is energetically unfavourable. They state that QWSs are only confined when both layers are ferromagnetically aligned. In order to move to a more energetically favourable state, there is a magnetic reordering to an anti-parallel alignment [61]. This is more rigorously described in ref. [67]. Here Bruno suggests that the amplitude of the reflected wave is dependent on whether the spin of the incoming electron is aligned parallel or anti-parallel with the ferromagnetic layer. This results in a standing wave which is dependent on the spin of the electron and therefore there is a spin-polarisation within the normal metal spacer which oscillates with thickness. Full theoretical treatment of quantum well states within thin films provides a thorough explanation of many aspects related to interlayer coupling [60], which are not provided by the RKKY based methods.

While oscillations in interlayer coupling are typically associated with the thickness of the spacer layer, QWSs are also observable by adjusting the thickness of the ferromagnetic layer [68, 69].

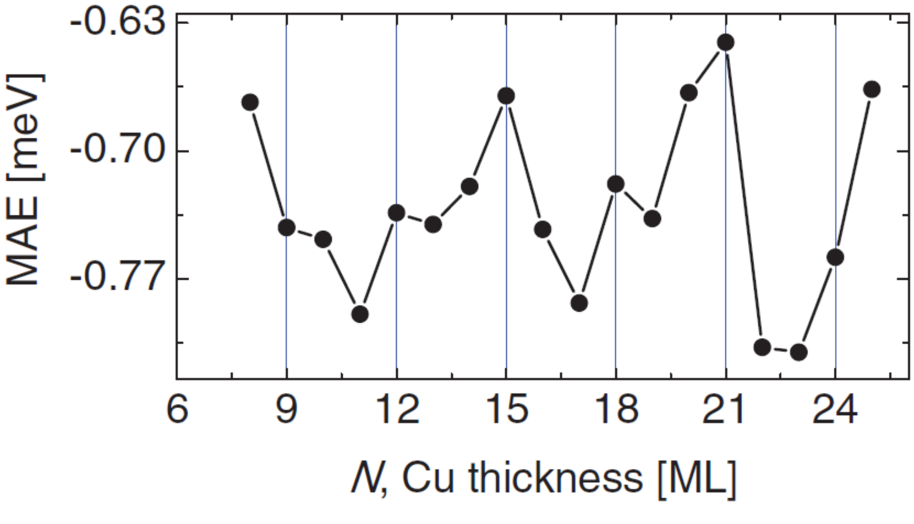

Figure 2.7: Theoretical calculations of the magnetic anisotropy energy of a Co/Cu bilayer system. There are clear oscillations of the anisotropy energy with increasing thickness of copper. Taken for ref. [70].

The presence of quantum well states can also exhibit changes in the magnetic anisotropy energy. As the thickness of the confining layer changes, the changes in the electronic states near the Fermi energy alters the anisotropy. This occurs for the case where the ferromagnetic film thickness is altered [69], as well as the case where the thickness of a non-magnetic over-layer is increased [66, 70, 71]. In both cases oscillations are strongest at low temperature, either presenting weakly at room temperature [69, 70], or disappearing completely [72, 73]. Manna *et al.* state that QWSs cannot be observed at room temperature[4], but the work of Dahmane *et al.* observes clear oscillations in the PMA of Pt/Co/Al(O_x) thin films at room temperature [74].

In a ferromagnetic layer it is straight forward to understand how quantum well states alter the magnetic anisotropy. However, changes in anisotropy due to the changing thickness of a non-magnetic over-layer are not so obvious. QWSs present in non-magnetic layer are thought to hybridise with those present in the ferromagnet. As the QWSs change with increasing over-layer thickness, the hybridisation between the layers is altered resulting in a modification of the magnetic anisotropy within the ferromagnet.

2.1.4.2 Heavy Metals for Spintronic Applications

While oscillatory exchange coupling is observed in heavy metals, they are of little use for GMR. This is due to their short spin coherence length. When electrons pass through a FM layer, they are spin polarised. Within a heavy metal, electrons would experience scattering which may flip the spin. If this occurs, the resultant read out from the GMR device may no longer be reliable, so traditionally heavier materials have been passed over in favour of lighter elements.

However, research into the next generation of spintronic devices often require large spin orbit coupling, for the production of spin currents or formation of chiral spin textures. The SOC is often thought to go as Z^4, where Z is the atomic number [75]. Therefore, heavier elements, such as platinum, gold, and palladium are good choices.

These phenomena are not necessarily limited to elemental heavy metals, and can be observed in silicon, bismuth, and oxides for example. However, for the purposes of this work, comparisons and discussions will usually be limited to the heavy metal cases.

2.1.4.3 Spin Torques and the Spin Hall Effect

One key focus in spintronics research lies in the transfer of spin-angular momentum via spin torques. Using spin torques the direction of magnetisation of a ferromagnet can be altered. When the orientation of the spin current is misaligned with the ferromagnet magnetisation

---

[4] There are some questions about this statement based on the data presented. While this is clearly true for the case of Co/Cu, the Fe/Cu film shows what could be interpreted as an oscillation at 300K. However, the origin of this is not touched on in ref. [70].

vector, spin-angular momentum is transferred from the current to the ferromagnet, causing a rotation of the magnetisation [76]. This transfer of spin-angular momentum can also be utilised for the propagation of domain walls within a magnetic layer, which is the cornerstone for spintronic devices such as magnetic racetrack memory [53].

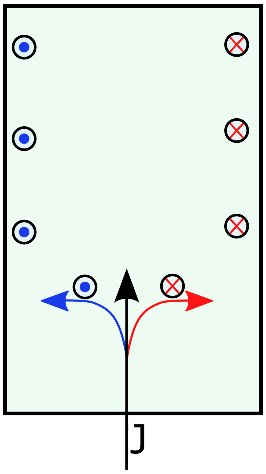

Figure 2.8: Illustration of spin Hall effect. As current J is passed through the material, spin up and spin down electrons are displaced horizontally, in opposite directions.

These torques can be categorised as *spin transfer torque* (STT) and *spin orbit torque* (SOT). The difference between these two phenomena lies in the origin of the spin current. For spin transfer torque, spin polarised currents can be produced by passing a current through a ferromagnetic thin film, or pure spin currents can be produced via spin-pumping through ferromagnetic resonance or from the spin Seebeck effect. For spin orbit torques, pure spin currents are produced via interactions related to spin-orbit coupling, such as the spin Hall effect (SHE).

Spin currents can be efficiently produced using the spin Hall effect. When electrons in a charge current travel along a paramagnetic material or doped semiconductor, spin-orbit effects result in a transverse displacement of the electrons. The direction of this displacement is dependent on whether the electrons are spin up or spin down. There is also a corresponding inverse effect, known as the inverse spin Hall effect (ISHE). In this case, when pure spin currents travel through the non-magnetic material, a transverse charge current is generated. This effect can be used to detect spin currents, even those which do not originate from the SHE [77], such as those generated by ferromagnetic resonance or the spin Seebeck effect.

Depending on the origin of the spin Hall effect, it can be classified as either *intrinsic* or *extrinsic*. In the extrinsic SHE, the splitting of spins is due to spin orbit scattering within the material [78,79]. In works by Niimi *et al.*, this extrinsic spin Hall effect was observed by adding spin-orbit impurities (Ir and Bi) into a Cu layer [80, 81].

The intrinsic SHE, on the other hand, is not rooted in scattering. Rather, in a perfect crystal, a spin dependent velocity along the transverse direction is generated by the spin-orbit field of the crystal [77].

	Spin Hall angle (%)		Spin Hall angle (%)
Al	0.032	Ag	0.7
	0.016	Ta	-12
Cu	0.32	W	-33
CuIr	2.1	Pt	0.37
CuBi	-11		2.1
Nb	-0.87		8.6
Mo	-0.8	Au	11.3
Pd	0.64		7.0
	1.2		0.35

Table 2.1: A small selection of spin Hall angles determined through experiment. Taken from ref. [77].

The efficiency of conversion from charge to spin current in a system is classified by the spin Hall angle. The spin Hall angle is the ratio of spin conductivity to charge conductivity [77]. The spin Hall angles determined for the extrinsic spin Hall effect in CuBi was found to be -11% [81], and work on β-tungsten thin films observed a large spin Hall angle of 33% [82]. Spin Hall angles of these kind of magnitudes are often thought of as "giant". Table 2.1 presents a selection of experimental data collated in ref. [77]. For some materials there are a range of different spin Hall angles due to experimental method and experimental conditions such as temperature. Samples studied using the same techniques and parameters can also result in variations in the spin Hall angles depending on how "clean" the sample is [83]. A full table of experimental spin Hall angles for a variety of metals can be found in refs. [77] & [84].

The presence of the spin Hall effect in a material can be determined by a number of methods, such as spin torque ferromagnetic resonance (ST-FMR) [85], spin Hall magnetoresistance [86] and Kerr rotation measurements [87] to name a few. In the ST-FMR case, the measured curve is composed of a symmetric part, which is due to the spin Hall effect, and an antisymmetric part, which results from torque arising from Oersted fields due to the current in the non-magnetic layer. Such a curve is illustrated in fig.2.9a.

The first instance of the switching of magnetisation by spin torques was observed in tantalum, another material which exhibits a "giant" spin Hall effect [88]. Liu *et al.* observed switching when the magnetic layer was in the in-plane and in the out-of-plane configurations.

The magnetisation reversial of the CoFeB layer from the spin current produced by tantalum can be seen in fig.2.9b.

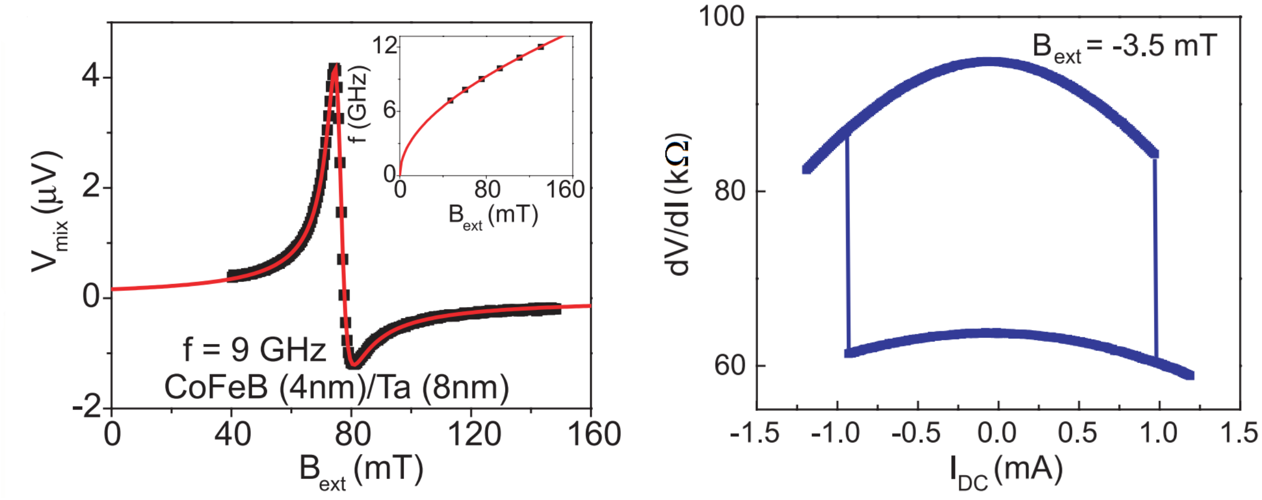

(a)

(b)

Figure 2.9: Asymmetric Lozentzian produced by ST-FMR. The fitting of the symmetric and antisymmetric parts allow the spin Hall angle to be determined b) Magnetisation reversal of a CoFeB layer using spin torque resulting spin currents produced by the spin Hall effect in a tantalum thin film. Both taken from ref. [88]

2.1.5 Proximity Induced Magnetisation

Typically, thin film heterostructures are central to the creation of spintronic devices. One consequence of the FM/NM heterostructures is the formation of a induced magnetic moment within the normal metal layer.

Induced magnetic moments in a non-magnetic material can be easily studied using x-ray circular dichroism (XMCD), which is an element sensitive technique. By tuning the x-ray energies, specific absorption edges can be probed. Left and right circularly polarised x-ray impinge upon a sample and the difference in absorption between the two chiralities is determined [89]. From the spectra obtained through XMCD, the size of the induced orbital μ_L and spin μ_S magnetic moments – in units of μ_B per atom – can be determined.

The presence of induced moments have been well documented in light metals such as copper [91,92] and heavy metals [12,93–97]. In the case of platinum, induced magnetic moments have been observed when grown on both ferromagnetic metals [90,94] – XMCD data shown in fig.2.10

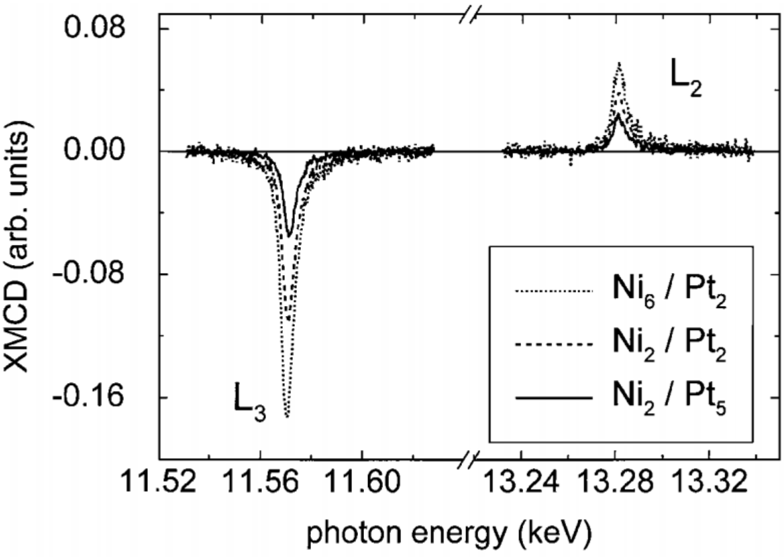

Figure 2.10: XMCD signal from the L_2 and L_3 Pt edges when grown on Ni. XMCD signal increases with increasing Ni and decreasing Pt thickness. Taken from ref. [90].

– and the ferromagnetic insulator $Y_3Fe_5O_{12}$ (YIG) [12,96]. The origin of this magnetic proximity effect is often attributed to hybridisation of electron orbitals of the ferromagnet and the normal metal. This hybridisation can affect the positions of the majority and minority spin bands with respect to the Fermi energy, which can alter the alignment of the induced moment [95, 98]. The induced moment can be aligned parallel or anti-parallel to the ferromagnetic layer. This orientation is dependent on the filling of bands and can be described in terms of a Bethe-Slater curve. As the bands are filled, the distance between the magnetically important electrons increases which results in a switch in the sign of the exchange constant J. This corresponds to a switch from ferromagnetic to antiferromagnetic alignment [95].

Unfortunately, the presence of an induced moment presents issues for spintronic applications. Transport studies by Huang *et al.* concluded that the presence of an induced moment in Pt compromised the metal's ability for spin detection through the ISHE [12].

2.2 Uranium

Uranium is a naturally occurring heavy metal [5] with a variety of interesting properties, including charge density waves and superconductivity [99]. The condensed matter properties of uranium

---

[5] Other popular forms of heavy metal include Black Sabbath, Iron Maiden and Metallica.

are of great interest due to its $5f$ states, as well as its potentially large spin orbit coupling.

There are three main structural phases of uranium: the high temperature stable bcc γ phase, the β phase which is tetragonal, and the room-temperature stable orthorhombic α phase [99]. There is also an additional hcp phase which can be accessed when grown as thin film [100]. However, in this thesis only α-U will be discussed.

As uranium is expected to have a large spin-orbit coupling it may be expected that it would have an appropriately large spin Hall angle. However, work by Singh *et al.* observed a spin Hall angle of only 0.4% for α-U/Py bilayers [101]. The determination of this spin Hall angle was done through spin torque ferromagnetic resonance (ST-FMR), with the decomposition of the FMR curve into its symmetrical and antisymmetric parts shown in fig.2.11. Despite its small spin Hall angle, polycrystalline α uranium presents many potentially interesting avenues to research.

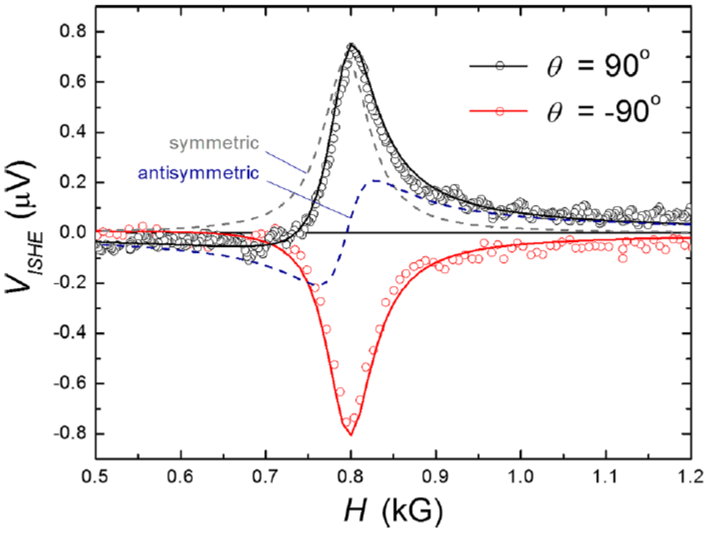

Figure 2.11: Ferromagnetic resonance from a U/Py thin film. The spin Hall angle is determined from the symmetric contribution to the resonance. Taken from ref. [101]

2.2.1 Magnetism in Uranium

There are a number of uranium based compounds which exhibit magnetic ordering, as illustrated by the Hill plot shown in fig.2.12. Magnetic compounds tend to exist around the region where the uranium inter-atomic spacing is 3.5 Å – 4.5 Å.

Elemental uranium appears to exhibit no magnetic ordering. There are theoretical calcu-

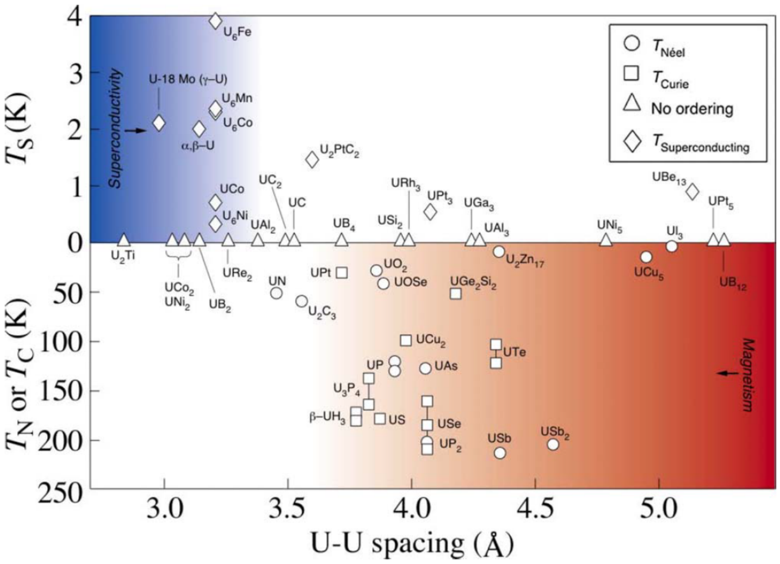

Figure 2.12: Hill plot for uranium and its various compounds. For materials where the interatomic spacing is between 3.5 Å – 4.5 Å, there is likely to be some magnetic ordering. Taken from ref. [102].

lations which suggest that a surface layer of uranium in a vacuum has a magnetic moment of $0.65\,\mu_B$ [103], though it seems that this has yet to be realised experimentally. However, there are some cases experimentally where a magnetic moment can be induced in uranium.

2.2.1.1 Induced Moment in Multilayer Thin Films

Based on the trend given in fig.2.12, it is clear that the interatomic spacing of uranium should not promote magnetism. However, in iron/uranium multilayer systems, a moment was observed in the uranium layers at room temperature though x-ray resonant magnetic scattering [104,105] and XMCD [13]. From the XMCD studies, Wilhelm *et al.* determined that the magnetic moment was a proximity induced magnetisation. They also observed that the XMCD signal was not linear with uranium thickness and proposed that within a U layer grown between two Fe layers, that the induced moment oscillates, as illustrated in fig.2.13. Brown *et al.* compared the relative density of materials within the layered structure with the magnitude of the induced magnetic moment [105]. Here it was found that large moments at the interface are due to the low density of uranium, with the moment decreasing with increasing density through the U layer. Within the layer profile presented, it appears that the induced moment would change both sign and magnitude, though no comment was made on on this.

Further studies found that an induced moment is not present in all ferromagnet/U structures

[14]. When grown on Co or Ni, there are no signs of magnetism in U from the XMCD signal, as illustrated in fig.2.14. Based on this, the induced moment in Fe-based samples is thought to arise from strong hybridisation between the Fe $3d$ and U $5f$ electrons. In both nickel and cobalt systems, the hybridisation is expected to be significantly weaker [106], resulting in no induced moment.

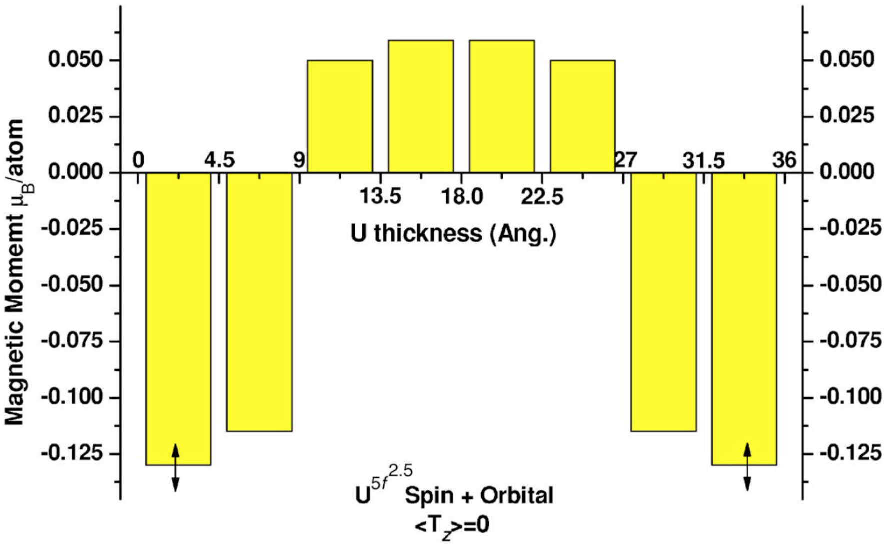

Figure 2.13: Calculations of induced magnetic moment as a function of depth within a U thin film layer. This layer is grown on and capped with iron. Taken from ref [13].

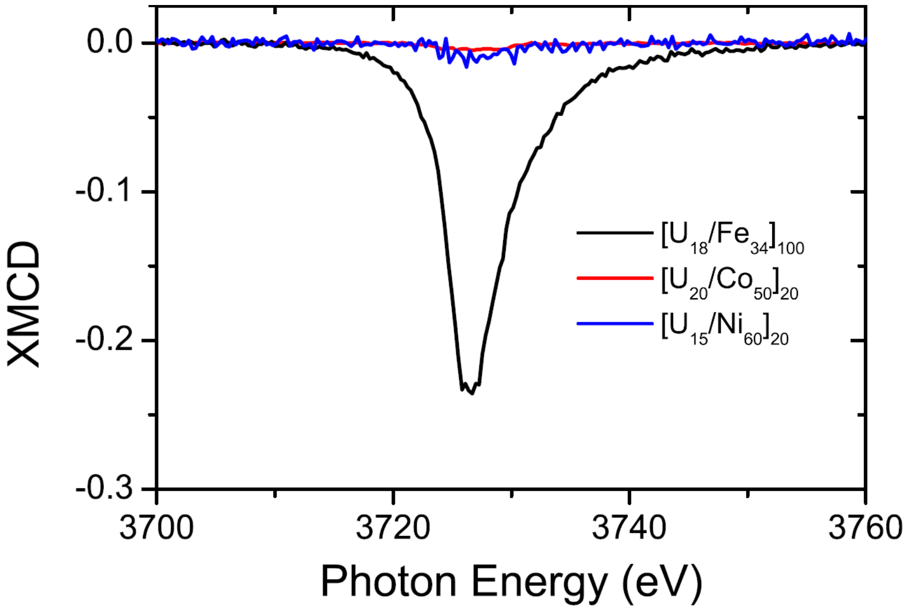

Figure 2.14: XMCD signals for U/FM films. Only iron based multilayers result in a uranium induced moment. Taken from ref [14].

Chapter 3

Sample Growth and Characterisation

3.1 Sample Growth

In the field of spintronics, devices are often formed of a thin layer or *thin films* of the desired material. These thin films can be formed, or grown, in a variety of ways, such as molecular beam epitaxy, pulse laser deposition and magnetron sputtering. In this thesis, thin film samples are grown using DC magnetron sputtering.

3.1.1 DC Magnetron Sputtering

Sputtering is a technique through which thin films can be fabricated with ease. This process involves the ejection of atoms from a target material as argon ions bombard the target's surface. The ejected atoms then condense onto a substrate creating a thin film of material, as illustrated by fig.3.1.

DC magnetron sputtering is carried out in a vacuum chamber, were discs of target material are mounted on "sputtering guns". A constant bias voltage is passed through the target, typically on the order of hundreds of volts, creating a *target cathode* to which ions are attracted. When ions impinge on the target material, atoms are liberated from the surface. However, there is also the production of electrons. These secondary electrons will ionise argon atoms in the chamber, creating a self-sustaining plasma. Underneath the target, the guns contain magnets, which confine the plasma, demonstrated in fig.3.2. This confinement allows for more efficient sputtering and an increased rate of deposition. However, when sputtering magnetic materials, this confinement can be disrupted, resulting in significantly lower sputtering rates than their non-magnetic counterparts.

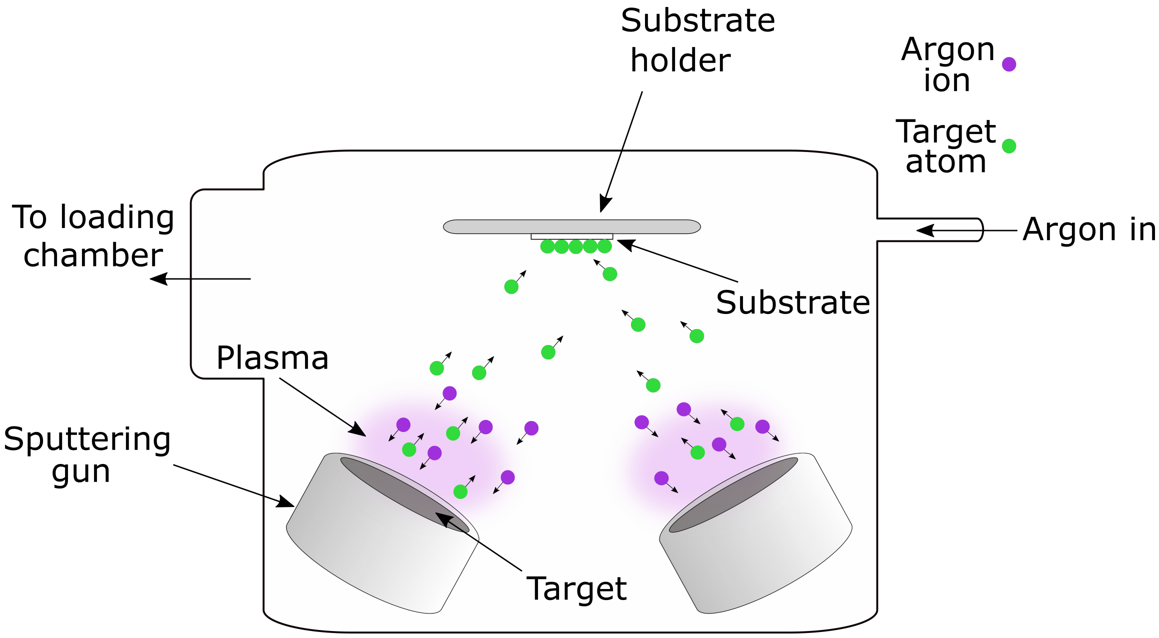

Figure 3.1: Cross-section of sputtering kit main chamber. Argon plasmas are confined above the target material to be sputtered. Incoming ions bombard the target surface and dislodge atoms of the target material which accumulate on the substrate, building up a thin film.

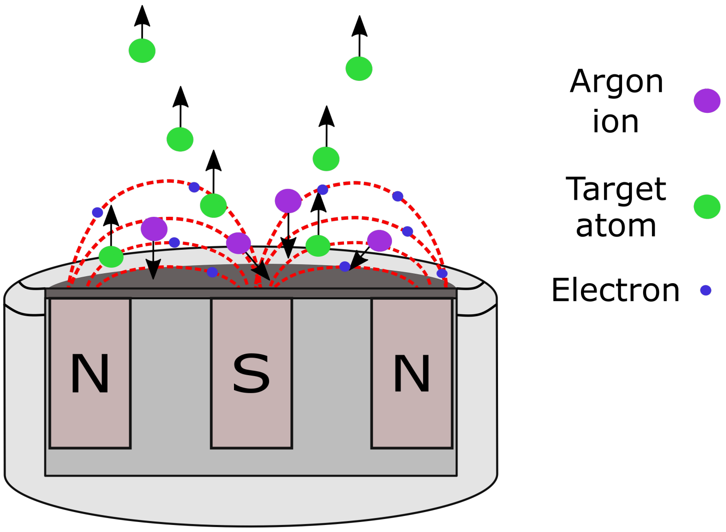

Figure 3.2: Representation of a sputtering gun cross-section. This illustrates the confinement of an argon plasma by magnetic fields created by the magnetic configuration below the target.

Sputtering allows for good control over the deposition rate, which can be advantageous when growing very thin layers or alloy systems. The simplest way to alter the rate is by adjusting the power to the sputtering gun. As the voltage increases (decreases), there will be a corresponding increase (decrease) in the flux of ions at the target's surface. This leads to a larger (smaller) number of ejected target atoms. The sputtering rate can also be controlled by the argon gas pressure within the chamber, though the relationship between gas pressure and deposition rate is complex. Initially an increase in gas pressure will result in an increase in ejection of material due to an increase in flux. However, at a certain point, the ejected atoms will undergo many collisions with the argon gas before reaching the substrate, resulting in a reduced rate.

3.1.2 Set-up and Growth

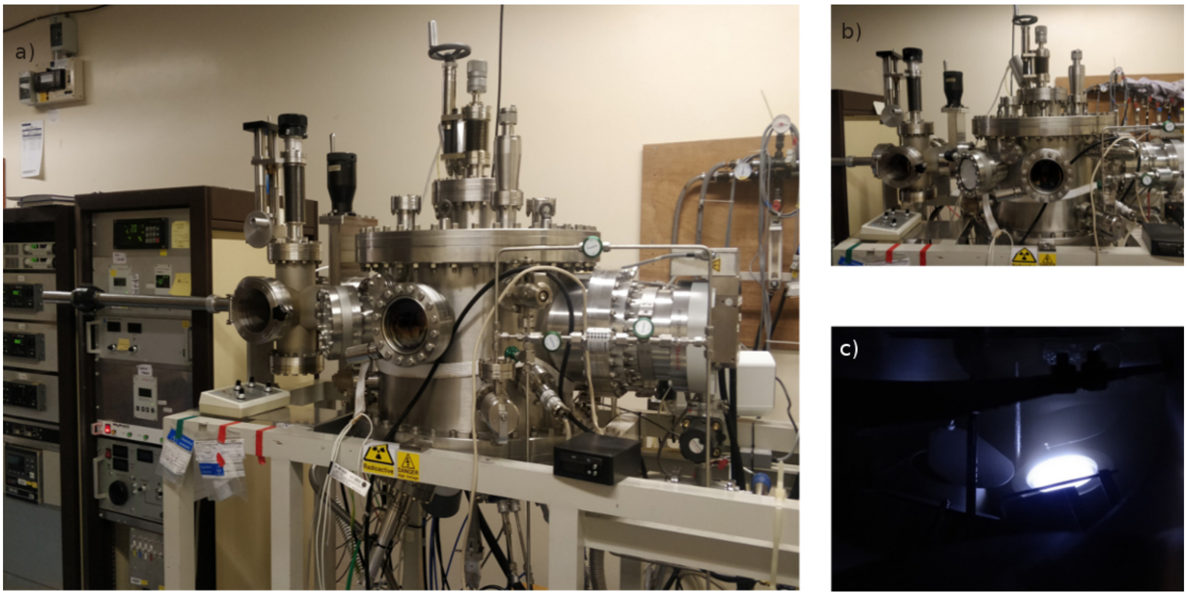

Figure 3.3: Photographs of 4-target DC sputtering kit used to grow thin films. a) Full view of kit including loading arm (left). b) Close-up view of loading (left) and main (right) chambers. c) Image of target during deposition of single element. The plasma (white glow) is confined above the target.

The samples studied in this thesis were grown using an ultra-high vacuum 4-gun DC magnetron sputtering kit, which can be seen in fig.3.3. The kit is composed of two chambers, one for loading substrates and another for sputtering of material, referred to as the loading chamber and main chamber respectively. This two-chamber system is advantageous as targets are not exposed to air with every substrate change. This prevents oxidation of target materials, which is especially important for sputtering of uranium metal as it oxidises readily. The loading chamber is connected to the main chamber through a gate valve. Samples are transferred between chambers using a 3-prong loading arm. The loading chamber can reach a base vacuum of ∼10^{-8} mbar, and the main chamber is kept in a the region of 10^{-9} – 10^{-10} mbar.

Material	Sputtering rate (Å s^{-1})
Iron	0.17
Nickel	0.3
Uranium	1.0
Niobium	1.0

Table 3.1: Sputtering rates of the elements used in bilayer systems, determined by x-ray reflectivity.

During growth it was important that the sputtering rate of each element was constant across each sample series. In order to achieve this, the argon was held at a constant pressure of (7.00 ± 0.05) $\times 10^{-3}$ mbar for all samples. Additionally, for bilayer samples, the power was kept at 50 W for all elements.

Before the growth of the bilayer structures, calibration samples for each element were grown for a fixed period of time. This allowed the determination of sputtering rates for each material, which are detailed in table 3.1. The rate calibration and determination of thickness are discussed in more detail in section 3.2. All samples were grown on Corning glass, 10 mm × 10 mm × 0.7 mm thick, and Suprasil 2 of size 5 mm × 2 mm × 1 mm thick. Bilayer samples were capped with niobium as it creates a passivating oxide layer, expected to be ∼20 Å thick [107], preventing the layers underneath from oxidising. For Fe-based structures, the Nb cap was ∼10 nm and for Ni bilayers it was increased to ∼15 nm[1]. The uranium layer was systematically increased for both types of bilayer. All growth was carried out at room temperature.

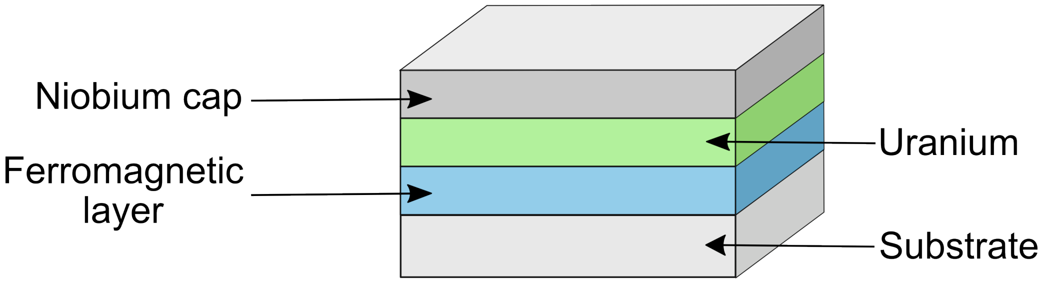

Figure 3.4: Structure of a bilayer sample. The ferromagnetic layer is grown directly on the substrate, with uranium grown on top. The sample is capped with niobium to prevent oxidation.

A schematic of the bilayer structure is shown in fig.3.4. The ferromagnetic layer was grown

---

[1] The niobium thickness was increased as it was initially thought that the Fe-based samples oxidised and degraded over the course of a year. However, the deterioration of Fe-based samples was later attributed to the poor adhesion of Fe to glass.

on the bare substrate, with the uranium layer sputtered on top. This structure was chosen to avoid formation of UO_2 from oxygen in the substrate. A full list of bilayer samples grown can be found in tables 3.2 & 3.3.

Sample ID	Iron thickness (nm)	Uranium thickness (nm)
1239	8.0 ± 0.4	0
1214	8.7 ± 0.2	1.7 ± 0.2
1215	8.8 ± 0.05	2.0 ± 0.05
1216	9.0 ± 0.08	2.2 ± 0.06
1217	8.8 ± 0.07	3.0 ± 0.08
1218	8.7 ± 0.05	3.2 ± 0.1
1219	8.9 ± 0.05	3.8 ± 0.05
1220	8.7 ± 0.07	4.4 ± 0.05
1221	8.8 ± 0.02	5.0 ± 0.02
1222	9.0 ± 0.1	5.3 ± 0.1
1223	8.3 ± 0.1	6.5 ± 0.1

Table 3.2: Sample thicknesses for the iron/uranium bilayer series, as determined by GenX reflectivity simulations. Errors are taken as the value required to change the figure of merit by 5%.

Sample ID	Nickel thickness (nm)	Uranium thickness (nm)
1319	12.6 ± 0.3	0
1320	11.5 ± 0.1	0.6 ± 0.1
1321	11.4 ± 0.2	1.5 ± 0.2
1322	11.7 ± 0.3	1.8 ± 0.4
1323	11.4 ± 0.5	2.9 ± 0.4
1324	10.9 ± 0.1	4.0 ± 0.1
1325	11.3 ± 0.3	4.3 ± 0.2
1326	12.0 ± 0.3	4.6 ± 0.3
1327	11.9 ± 0.3	5.3 ± 0.3
1328	11.7 ± 0.2	6.1 ± 0.2
1329	11.5 ± 0.2	6.9 ± 0.2
1330	11.8 ± 0.2	7.5 ± 0.2

Table 3.3: Nickel/uranium samples series thicknesses.

3.1.2.1 Alloy Samples

In addition to bilayer samples, dilute alloys of Cu-U and Ni-U were produced. To synthesise alloys, elements were co-sputtered. In both cases, the percentage of uranium was varied from

1 at.% – 12 at.%. In order to achieve the desired atomic percentage, the rate of deposition for uranium was altered. The required rate was calculated by determining the volume of U which would be equivalent to the desired percentage, in the time taken to grow a layer of Cu or Ni of 20 nm.

$$l_1 w_1 t_1 \frac{N_A}{M_1} \rho_1 = \frac{\%_1}{\%_2} l_2 w_2 t_2 \frac{N_A}{M_2} \rho_2, \tag{3.1}$$

where l_x, w_x, t_x are the length, width, and thickness of the element, M_x is the molar mass, ρ_x is the density and $\%_x$ is the atomic percentage of the given element. The subscript '1' denotes either Cu or Ni and '2' represents U.

To establish the current required to acquire these rates, a series of U samples were grown at various powers and a current-rate calibration curve was produced.

Copper-Uranium

During growth the Cu power was held constant at 100 W, while the uranium rate was varied between 5 W and 37 W, which allowed access to the percentage range required. The rates for each element used can be found in table 3.4.

Material	Sputtering rate (Å s^{-1})
Si	0.3
Ni	0.28
Cu	3.2
U	0.06–0.77

Table 3.4: Sputtering rates of the elements used in Cu-U systems, determined by x-ray reflectivity.

The Cu-U structures were grown on glass with a 10 nm Si buffer to prevent oxidation of any subsequent layers. On top of the buffer, a 10 nm Ni layer was deposited at 50 W. The Cu-U layer thickness was maintained at ∼20 nm, regardless of the U percentage. Finally, the system was capped with another 10 nm Si layer.

Nickel-Uranium

In order to fabricate samples with low U percentages in Ni, the nickel target was sputtered at 100 W. However, the U deposition rate was determined to be too high to grow the complete range of percentages, even at the lowest available power. To overcome this, a custom shutter for one of the sputtering guns was designed. The new shutter resembled the standard version, but with a 2 cm diameter hole at its centre, rather than a solid cover. This reduced the standard U 50 W rate by a factor of 10. The rates used can be found in table 3.5.

The structure of these samples consists of a 10 nm Si buffer, a Ni-U layer held at 20 nm and a 10 nm Si cap.

Material	Sputtering rate (Å s^{-1})
Si	0.6
Ni	0.66
U	0.013–0.17

Table 3.5: Sputtering rates of the elements used in Ni-U systems, determined by x-ray reflectivity.

3.2 X-Ray Characterisation

X-rays are a useful tool for probing the crystalline structure of materials, due to their short wavelengths, on the order of an Angstrom. X-rays interact with the electrons within a material, in a variety of different processes. In this work, only elastic scattering processes play a role.

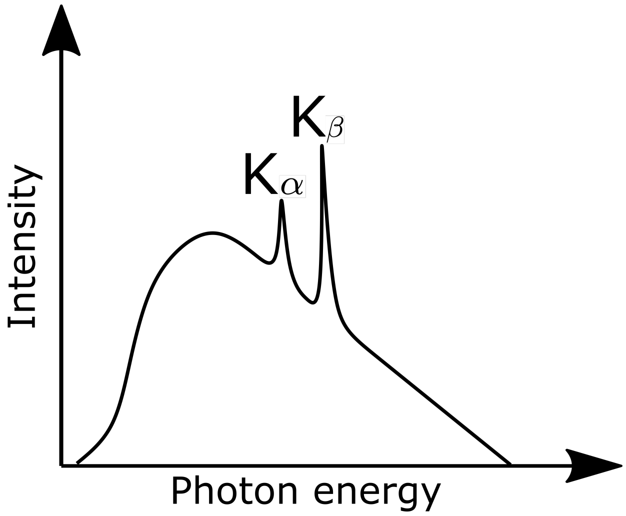

Figure 3.5: Expected X-ray spectrum for a Cu target anode. The broad background is due to Bremsstrahlung. The sharp K_α and K_β lines can be observed above the background.

When using a lab-based tube source, the x-ray spectrum is composed of two parts, Bremsstrahlung and characteristic fluorescence. Bremsstrahlung is caused by the deceleration of electrons due to scattering with the anode, producing a broad spectrum of x-rays. X-ray production by fluorescence occurs when accelerated electrons are incident of the anode target and excite inner shell electrons, leaving a vacancy. When an electron relaxes into that vacancy, an x-ray of specific wavelength is produced. The energy of these characteristic lines corresponds to a distinct electronic transition, e.g. a transition from the L to K orbitals produced a K_α line in the x-ray spectrum and a transition from M to K corresponds to the K_β line. The x-ray spectrum for a copper target is illustrated in fig.3.5.

3.2.1 X-ray Reflectivity

Samples were initially characterised using X-ray reflectivity (XRR). XRR is a non-destructive technique which can provide information about thin film thickness, surface and interface roughness. All reflectivity measurements were carried out using a Philips X'pert diffractometer, the set-up of which can be seen in fig.3.6, which uses a copper target anode with $K_\alpha = 1.540598\,\text{Å}$ and $K_\beta = 1.544426\,\text{Å}$.

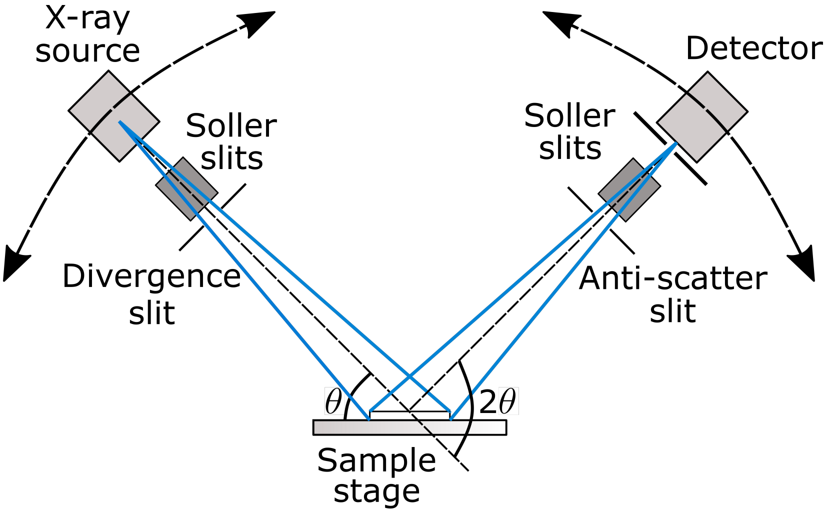

Figure 3.6: Configuration of x-ray diffractometer systems used.

3.2.1.1 Theory

The refractive index of a material is given by:

$$n = 1 - \delta + i\beta, \tag{3.2}$$

where δ and β are related to scattering and absorption respectively and are described as:

$$\delta = \frac{2\pi\rho_e r_0}{k^2}, \tag{3.3}$$

and

$$\beta = \frac{\mu}{2k}, \tag{3.4}$$

where ρ_e is the electron density of the material, r_0 is the Thomson scattering length, k is the wavevector and μ represents the absorption coefficient. For x-rays, the refractive index of a material is often <1. As a consequence of this, when x-rays are incident on a surface at an angle θ_i less than the critical angle θ_c, they undergo total external reflection. Above the critical angle, x-rays are transmitted into the sample.

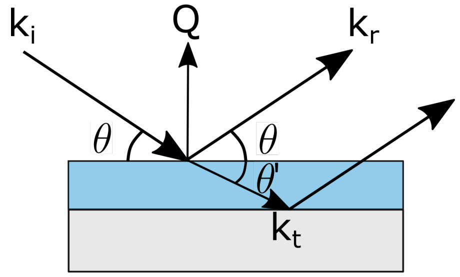

Figure 3.7: Representation of reflectivity geometry for a single layer thin film. In this picture k_i, k_r and k_t are the incident, reflected and transmitted wavevectors respectively. The scattering vector Q is perpendicular to the plane of the film as these are specular scans.

When an x-ray is incident on a material of a differing refractive index, as illustrated by fig.3.7, the following boundary conditions can be applied:

$$A_i + A_r = A_t, \tag{3.5}$$

where these values are the amplitude of the incident, reflected and transmitted waves respectively. This leads to

$$A_i\mathbf{k}_i + A_r\mathbf{k} = A_t\mathbf{k}_t, \tag{3.6}$$

where $|\mathbf{k}_i| = |\mathbf{k}_r| = k$, and $|\mathbf{k}_t| = nk$. Considering the components of k parallel to the material interface gives:

$$A_i k\cos\theta + A_r k_r\cos\theta = A_t nk\cos\theta'. \tag{3.7}$$

This leads to Snell's law:

$$\cos\theta = n\cos\theta', \tag{3.8}$$

which can be expanded to

$$\theta^2 = \theta'^2 + 2\delta - 2i\beta, \tag{3.9}$$

for small incident angles. From eqn.3.8 and 3.9, the critical angle for total external reflection is

$$\theta_c = \sqrt{2\delta}. \tag{3.10}$$

Considering the perpendicular components of k leads to the Fresnel equations for amplitudes of reflection and transmission. The intensity reflectivity and transmittivity are given by $R = r^2$ and $T = t^2$ respectively.

$$-(A_i - A_r)k\sin\theta = -A_t nk\sin\theta', \tag{3.11}$$

$$r = \frac{A_r}{A_i} = \frac{\theta - \theta'}{\theta + \theta'} \text{ and } t = \frac{A_t}{A_i} = \frac{2\theta}{\theta + \theta'}, \tag{3.12}$$

It is more convenient to think about this phenomenon in terms of the wave vector transfer Q, given by

$$Q = 2k\sin\theta \approx 2k\theta, \tag{3.13}$$

which can be used to define the dimensionless wavevectors q and q':

$$q = \frac{Q}{Q_c} = \frac{2k}{Q_c}\theta \text{ and } q' = \frac{Q}{Q_c} = \frac{2k}{Q_c}\theta', \tag{3.14}$$

where Q_c is determined by evaluating eqn.3.13 at $\theta = \theta_c$, and therefore $Q_c = 2k\sqrt{2\delta}$. Eqn.3.9 can be rewritten as

$$q^2 = q'^2 + 1 - 2i\left(\frac{2k}{Q_c}\right)^2\beta \tag{3.15}$$

Combining eqn.3.14 with eqn.3.12 gives both the reflectivity and transmittivity amplitudes as

$$r = \frac{A_r}{A_i} = \frac{q - q'}{q + q'} \text{ and } t = \frac{A_t}{A_i} = \frac{2q}{q + q'}. \tag{3.16}$$

The penetration depth is defined as

$$\Lambda = \frac{1}{Q_c \mathrm{Im}(q')}. \tag{3.17}$$

By evaluating eqns.3.16 & 3.17 for different q, the behaviour of reflectivity curves acquired in this work can be explained. In all cases discussed here it is assumed that $(\frac{2k}{Q_c})^2\beta \ll 1$.

$q \gg 1$: By evaluating eqn.3.15, it can be seen that the real part of q' is given as $\mathrm{Re}(q') \approx q$ and the imaginary part $\mathrm{Im}(q') \approx (\frac{2k}{Q_c})^2/q$. The reflectivity amplitude in equation 3.16 can also be written in the form $r(q) = (q^2 - q'^2)/(q + q')^2$. When in the limit of $q \gg 1$, then this can be approximated as $r(q) \approx 1/(2q)^2$. The intensity reflectivity $R(q)$ then changes with $(2q)^{-4}$, meaning that there is close to total transmission as q increases.

$q \ll 1$: Here, the imaginary part of $q' \approx 1$ and $r(q') \approx -1$. In this case, the incident and transmitted waves are out of phase so the transmitted wave is weak and eqn.3.17 becomes $1/Q_c$. This weak transmitted wave is known as the evanescent wave.

$q = 1$: In this case, the incident wave and reflected wave are in phase. This leads to a increase in the penetration depth Λ.

The behaviour of the reflected intensity described by these three cases is illustrated in fig.3.8a, the reflectivity from an semi-infinitely thick silicon substrate. The dashed red line represents the position of Q_c, before which the incident beam is totally externally reflected. Beyond Q_c, the intensity drops off as q^{-4}.

When x-rays are incident on a series of layers grown on an infinitely thick substrate, there will be reflection and transmission at each interface. Fig.3.7 illustrates this for an ideal single layer system. The reflections from each interfaces interfere, creating fringe patterns, known as Kiessig fringes, which are unique to the sample's structure. The spacing of these fringes is related to the thickness of the layers,

$$d = \frac{2\pi}{L}, \tag{3.18}$$

where d is the film thickness and L is the fringe separation. This relationship is illustrated by fig.3.8b. Both curves come from simulated reflectivity data for an perfectly flat iron layer grown on an infinitely thick silicon substrate. The q^{-4} dependence of the intensity can still be observed, with oscillations superimposed on top.

In reality, thin films will not be perfectly flat. At each interface there will be some roughness which will dampen the oscillations. Fig.3.8c displays the effect of roughness on reflectivity. As this roughness is increased, the oscillations are damped at higher Q.

In multilayer systems, the difference in density between materials results in more complex curves, as shown in fig.3.8d. This curve represents reflectivity from an iron/platinum bilayer.

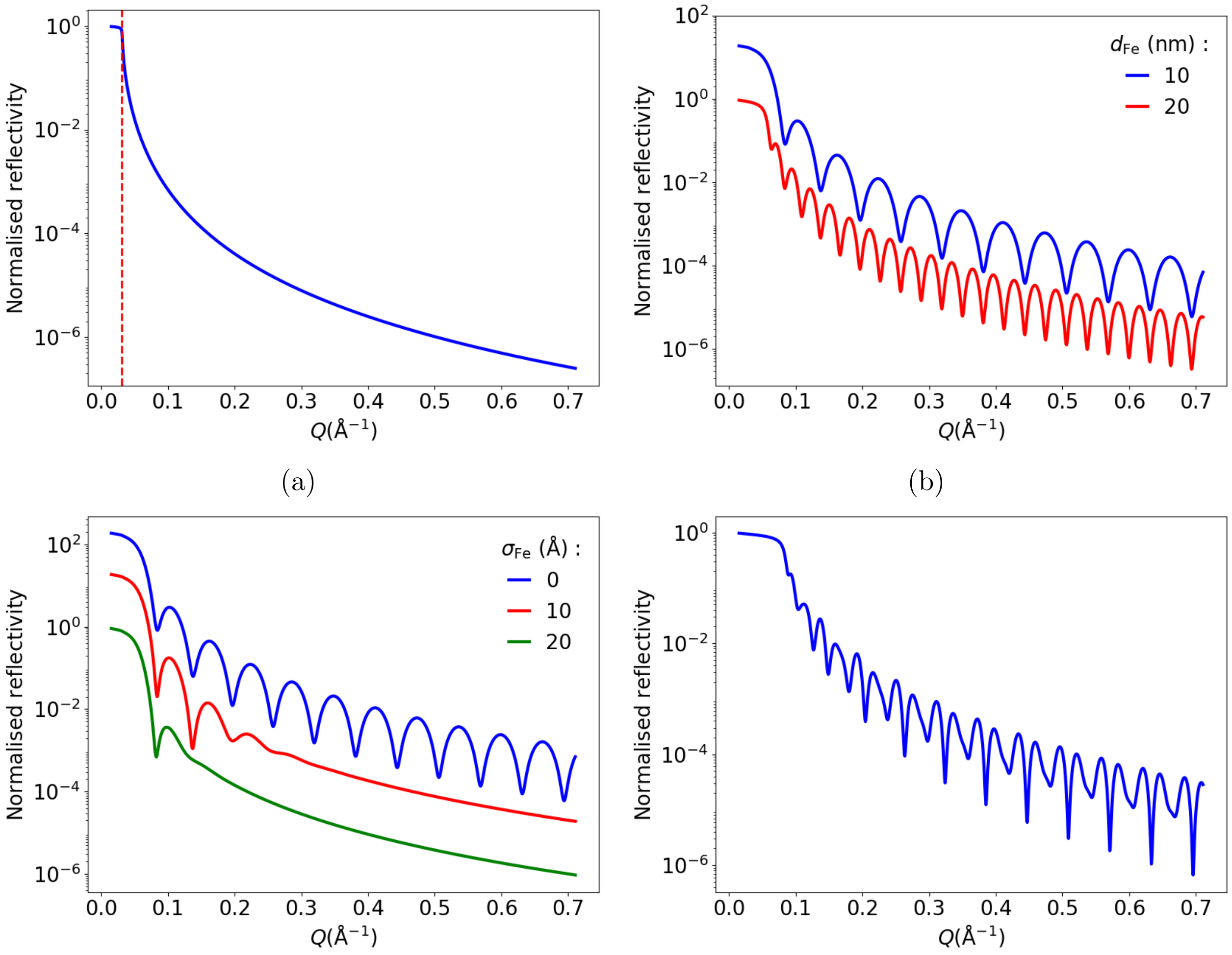

(a) (b) (c) (d)

Figure 3.8: Simulated reflectivity data for a number of different cases. All data was simulated using GenX. Curves offset vertically for clarity. a) X-ray reflectivity (blue) from a silicon substrate. Dashed line represents position of Q_c. Beyond this position, the reflected intensity decreased with q^{-4}. b) Perfectly flat iron layers of 10 nm (blue) and 20 nm (red). There is a clear decrease in fringe separation with the increasing thickness of iron. c) Non-ideal layers of iron (10 nm). Oscillations are damped as the roughness on the top of the iron film is increased. d) Reflectivity for a bilayer system of 20 nm of platinum on top of 10 nm of iron.

3.2.1.2 Reflectivity Modelling

The interference patterns can be fitted to determine the parameters of the structure. GenX reflectivity software, version 2.4.9, was used to determine film thickness and rms roughness [108, 109]. GenX allows the user to create a theoretical sample which is built up as a series of layers, each of which is defined by a number of parameters. The parameters required are the elemental composition of the layer and its density, as well as the expected thickness and roughness. The software produces a simulated reflectivity curve based on the parameters of the sample, using the Parratt recursion method [110]. In order to correctly simulate the reflectivity curve, the parameters of the instrument also need to be taken into account. This includes the x-ray wavelength, the beam footprint and the beam width. The theoretical sample model is altered using a differential evolution algorithm [109], until a sensible fit to the data is obtained. The parameters of the fit can be constrained around expected values. The thickness and rms roughness of the layers of the simulated system are taken as those of the sample to which the model is being compared. A logR1 figure-of-merit was chosen so as to give a more equal weighting to both high and low intensity points. The error on a given quantity is calculated as the change in that quantity required to change the figure of merit by 5%.

This software was employed for calibration of sputtering rates and to determine bilayer thickness. It was not used to characterise alloy samples as the alloy layer cannot be accurately modelled in GenX.

3.2.1.3 Fe-based bilayers

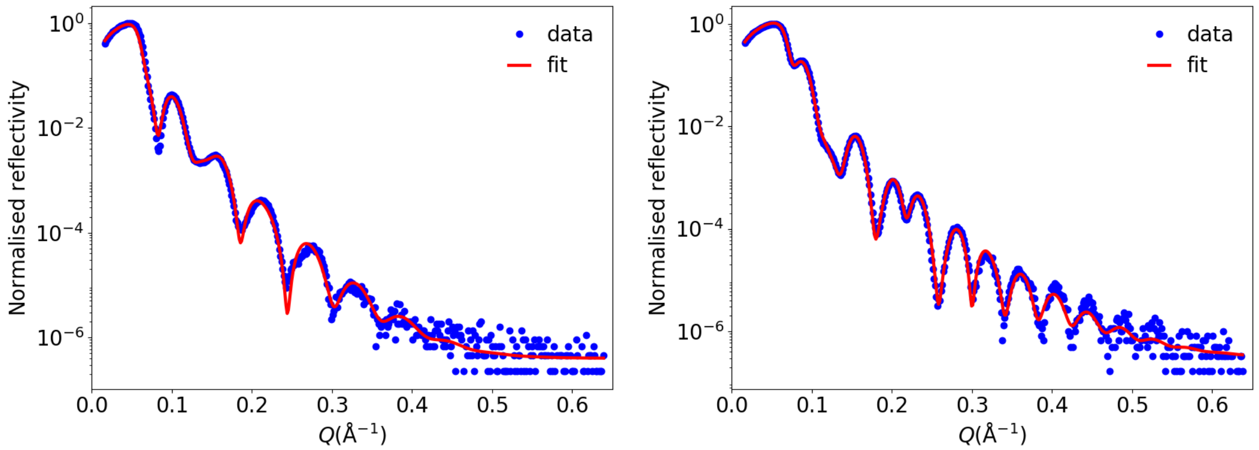

(a) (b)

Figure 3.9: Reflectivity data (blue) with fits (red) from Fe/U series. (a) Reflectivity for thinnest sample SN1214 $d_{\mathrm{U}} = 1.7\,\mathrm{nm}$. (b) Thickest sample SN1223 $d_{\mathrm{U}} = 6.5\,\mathrm{nm}$.

XRR was carried out on all samples in the series after growth. The samples were 10 mm × 10 mm in size. Reflectivity data from two iron-based samples can be seen in fig.3.9. The reflectivity data is represented by blue circles, with the red line representing the fit determined using GenX. Fig.3.9a shows reflectivity data from sample SN1214 which has the thinnest U layer in the series, $d_{\mathrm{U}} = 1.7\,\mathrm{nm}$, and fig.3.9b is from the thickest U layer, SN1239 with $d_{\mathrm{U}} = 6.5\,\mathrm{nm}$. As d_{U} increases there is decrease in the fringe width, as expected from eqn.3.18. Each of these samples were modelled as layers of glass (SiO_2), Fe, U, Nb and Nb_2O_5.

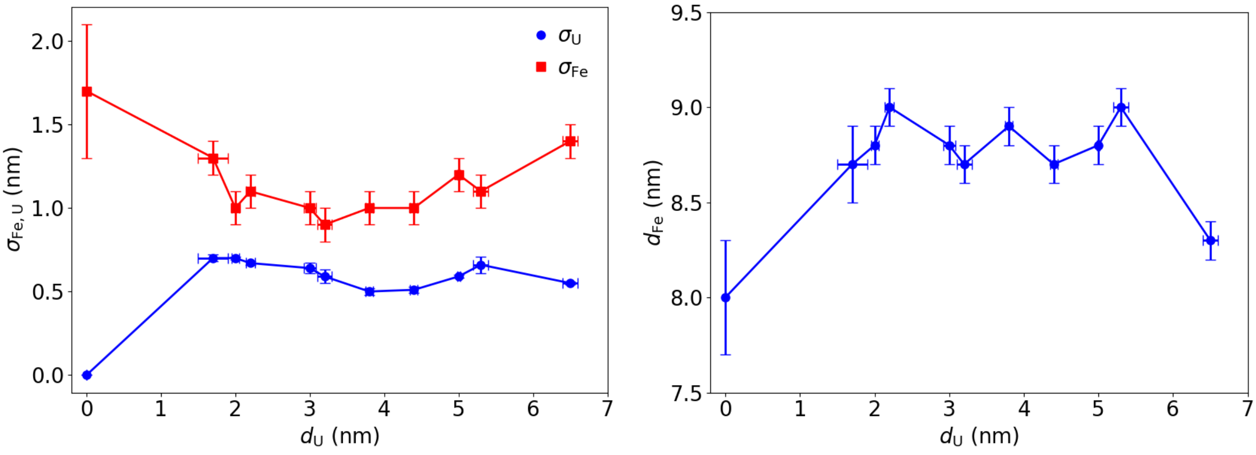

(a) (b)

Figure 3.10: Parameters taken from fitting using GenX modelling. a) Interfacial RMS roughness as a function of uranium thickness. σ_{Fe} and σ_{U} are roughness at interfaces Fe/U (with the exception of d_U=0 which is Fe/Nb) and U/Nb respectively. b) Iron layer thickness throughout the series.

It is important to understand how the rms roughness at the ferromagnet/U and U/cap interfaces changes as a function of thickness. It is expected to be monotonic with d_U, but unusual variations may affect the results of subsequent measurements. The rms roughness for the Fe/U (σ_{Fe}) and U/Nb (σ_{U}) interfaces are illustrated in fig.3.10a. At the U/Nb interface, the roughness is approximately constant. The roughness at the Fe/U interface shows more variation with d_U which is most likely due to the tendency for iron and uranium to interdiffuse [111]. The point at $d_{\mathrm{U}} = 0\,\mathrm{nm}$ can be excluded from this trend as it represents an Fe/Nb interface, which behaves differently from that of Fe/U. Despite the variation being comparably greater in σ_{Fe} than in σ_{U}, σ_{Fe} is still roughly constant.

There is also some deviation in the thickness of iron in the samples, represented in fig.3.10b. This may stem from inconsistencies in growth across the sample set. During growth it was seen that the gas pressure would vary if not closely monitored. A slight increase or decrease in the pressure could affect the rate of deposition resulting in variations in thickness. Additionally, as the rate of deposition is dependent on current, any changes could alter the deposition rate.

3.2.1.4 Ni-based bilayers

Reflectivity was also carried out on the nickel series. Fig.3.11 represents the reflectivity from nickel-based systems, with $d_{\mathrm{U}} = 0.6\,\mathrm{nm}$ in fig.3.11a and $d_{\mathrm{U}} = 7.5\,\mathrm{nm}$ in fig.3.11b. In comparison to the Fe-based layers, there is a clear decrease in fringe separation, even at low d_{U}, which is attributed to the thicker Nb cap.

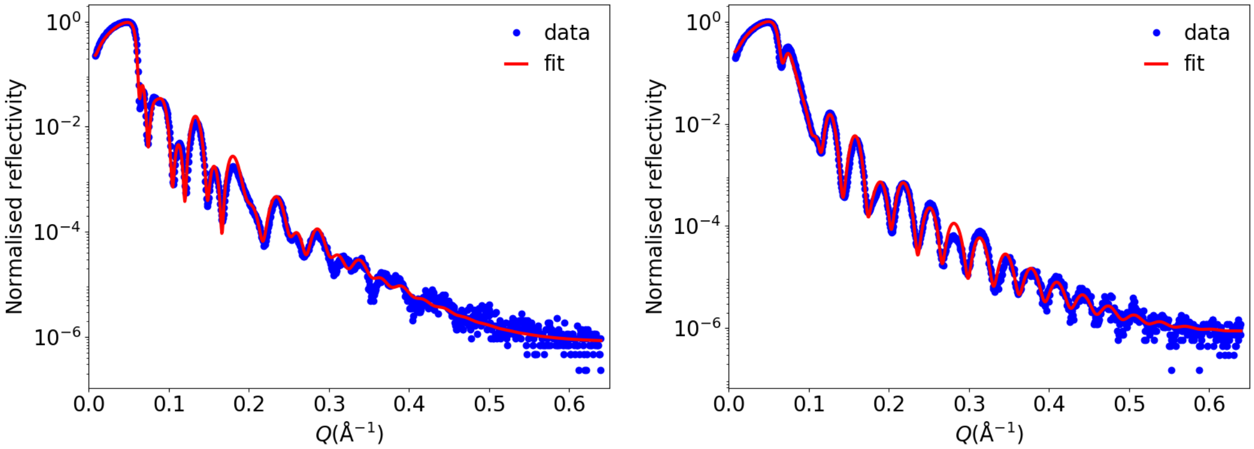

(a)

(b)

Figure 3.11: XRR data (blue circle) with GenX fits (red) for the thinnest and thickest d_{U} in the series. a) $d_{\mathrm{U}} = 0.6\,\mathrm{nm}$. b) $d_{\mathrm{U}} = 7.5\,\mathrm{nm}$.

There is a larger variation in the Ni/U interfacial roughness at low d_{U}, than for thicker samples, shown in fig.3.12a. This is likely due to partial coverage of the nickel layer at very low thickness as well as interdiffusion. This is mirrored in the roughness between U/Nb.

Again, like in the iron series, there is also some variation in nickel thickness across the sample series, fig.3.12b, which may be attributed to fluctuations in gas pressure or power to the sputtering gun. The fluctuations in thickness are small enough that it can be assumed that it will have no profound effect on the magnetic properties of the system.

3.2.2 X-ray Diffraction and Grazing Incidence

X-ray diffraction (XRD) and grazing incidence x-ray diffraction (GIXRD) studies were carried out in order to to provide structural information about individual layers, i.e. whether they are polycrystalline or exhibit a preferred orientation.

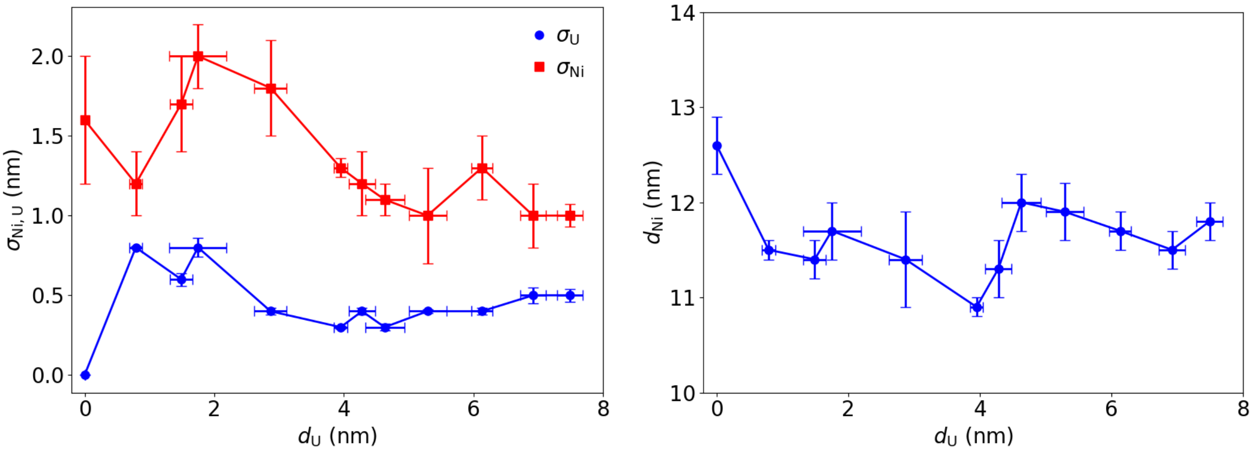

(a) (b)

Figure 3.12: Details of interfacial roughness and nickel thickness taken from GenX fitting. a) Interfactial roughness for the Ni/U interface (red square) and the U/Nb interface (blue circle). For the Ni/U interface, the point at $d_{\mathrm{U}} = 0\,\mathrm{nm}$ actually represents the Ni/Nb interfacial roughness. b) Nickel thickness across the sample series.

3.2.2.1 Theory

In a crystalline material the atoms are periodically arranged, giving parallel atomic planes, with spacing d. When a wave is incident on successive lattice planes constructive interference of the reflected waves occurs if

$$n\lambda = 2d \sin\theta, \tag{3.19}$$

where n is an integer number and θ is the incident angle of the wave. This is known as Bragg's law. However, Bragg's law does not provide full detail of x-ray scattering in a crystal [16, 112].

For a more thorough description of the scattering process, we start with the scattering amplitude from a crystal,

$$F(\mathbf{Q}) = \sum_{l}^{\text{All atoms}} f_l(\mathbf{Q}) e^{i\mathbf{Q}\cdot\mathbf{r}_l}, \tag{3.20}$$

where f_l is the form factor of the atom at a position $\mathbf{r}_l$, which is comprised of lattice vector $\mathbf{R_n} = n_1\mathbf{a}_1 + n_2\mathbf{a}_2 + n_3\mathbf{a}_3$ and the atomic position within the unit cell $\mathbf{r}_j$, i.e. $\mathbf{r}_l = \mathbf{R}_n + \mathbf{r}_j$. Eqn.3.20 can then be decomposed into

$$F(\mathbf{Q}) = \sum_j f_j(\mathbf{Q}) e^{i\mathbf{Q}\cdot\mathbf{r}_j} \sum_n e^{i\mathbf{Q}\cdot\mathbf{R}_n}. \tag{3.21}$$

The first sum in this equation is the unit cell structure factor, where $\mathbf{r}_j$ is the atomic position. This relies on the Miller indices of the plane of reflection. For some combinations of h,k and l this term becomes zero so scattering is said to be forbidden from that plane [113]. The second summation is a lattice site sum. This is related to the phases of the scattered waves and the sum is on the order of unity unless

$$\mathbf{Q} \cdot \mathbf{R}_{\boldsymbol{n}} = 2\pi \times n, \tag{3.22}$$

where n is an integer, in which case the sumis equal to a large number of terms [112]. In order to find a solution, the reciprocal lattice must be considered, which has basis vectors $\mathbf{a}_2^*$, $\mathbf{a}_2^*$ and $\mathbf{a}_3^*$. The reciprocal lattice vector is described by

$$\mathbf{G} = h\mathbf{a}_1^* + k\mathbf{a}_2^* + l\mathbf{a}_3^*. \tag{3.23}$$

This satisfies eqn.3.22 as

$$\mathbf{G} \cdot \mathbf{R}_{\boldsymbol{n}} = 2\pi(hn_1 + kn_2 + ln_3), \tag{3.24}$$

as $\mathbf{a}_i \cdot \mathbf{a}_j^* = 2\pi\delta_{ij}$. Here h, k and l are integers. Therefore,

$$\mathbf{Q} = \mathbf{G}. \tag{3.25}$$

This is known as the Laue condition. Constructive interference can only occur when eqn.3.25 is satisfied, otherwise the scattering amplitude becomes zero.

3.2.2.2 Set-up

XRD measurements were carried out using a $\theta - 2\theta$ geometry, illustrated in fig.3.13a. In this type of scan, both the source and detector are rotated mainaining the $\theta - 2\theta$ ratio, while the sample remains stationary. In this work, the $\theta - 2\theta$ scan is also referred to a high angle scan.

When studying thin films, there is only a small volume of material of interest compared with the large volume of the substrate. In $\theta - 2\theta$ scan, the contribution from the substrate is large, with a much weaker signal from the film. This often means details of the structure are lost. In order to obtain more structural information, grazing incidence x-ray diffraction (GIXRD) is used. GIXRD is a more surface sensitive technique. For GIXRD scan, the incoming beam is fixed at some angle ω, with only the detector rotating around the sample. This angle ω must be greater than the critical angle for total external reflection from the sample. By altering ω, the depth that the x-ray penetrates into the sample can be controlled. While GIXRD can

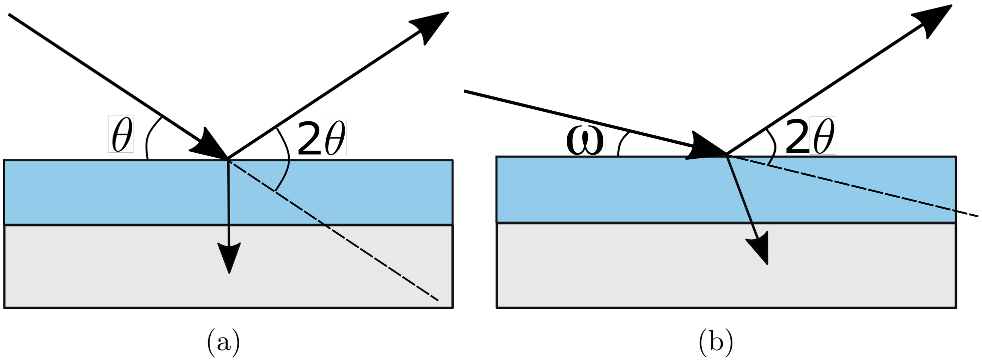

(a) (b)

Figure 3.13: Illustration of the difference between XRD and GIXRD scans a)The $\theta - 2\theta$ geometry. Here both source and detector rotate, maintaining that 2θ is always twice the incident angle. b) In the grazing incidence geometry the detector is fixed at an angle ω, while the detector rotates around the sample. As two theta increases, the angle of the scattering vector will shift so that it always bisects the angle between the incident and detected waves.

provide more information about a film than a typical $\theta - 2\theta$ measurement, there is one caveat; the planes contributing to the diffraction peak are not necessarily parallel to the surface, as illustrated by fig.3.13b. This means that texture observed for small ω is inclined in the x–y plane. However, the largest component of the scattering vector is in the z-direction so GIXRD can still provide some information on the crystallographic orientation of the sample.

XRD and grazing incidence measurements were initially carried out at the ISIS Neutron and Muon Source materials characterisation laboratory using a Rigaku SmartLab rotating anode diffractometer. The rotating anode is advantageous as heat is dissipated more efficiently, allowing for a higher flux than a conventional tube source. This allows for texture in thin films to be studied with reduced counting times, ∼0.8 s per point.

The texture of the films was determined to be important as the results of chapter 6.13 were discussed in depth. However, as samples had been sectioned for other measurements, only 10 mm × 5 mm pieces were available. Due to the low volume of material, and in some cases quality of the remaining samples, high angle and grazing incidence x-ray diffraction were carried out on one sample for each series. These samples are assumed to be representative of the entire series. The samples used were iron-based SN1219, $d_{\mathrm{U}} = 3.8\,\mathrm{nm}$, and nickel-based SN1329, $d_{\mathrm{U}} = 6.9\,\mathrm{nm}$.

After preliminary analysis of the low angle grazing incidence and the high angle $\theta - 2\theta$ scans, it was determined that intermediate angle scans would be important in determining any textural transition between the x–y plane of the film and the z axis. Subsequent GIXRD scans were then carried out in Bristol at 10°. Due to the reduction in flux when using the Philips X'pert system, steps were taken to insure a visible peak in a reasonable time. The range was limited to 30°–45°, as it is the texture of the uranium that is of interest and the detector was set to count for 70 s per point.

3.2.2.3 Fe-based Layers

Fig.3.14 illustrates the differences between an XRD $\theta - 2\theta$ measurement, fig.3.14a and grazing incidence x-ray diffraction, fig.3.14b. In both instances, there is a large background at low 2θ. This is from the amorphous glass substrate. In the high angle data, fig.3.14a, there is only one visible peak, whereas six peaks can be seen in the grazing incidence data, fig.3.14b. The peak observed in the XRD comes from the uranium layer. Despite the low volume of material, this peak is still clear due to the strong scattering of x-rays from this large Z element.

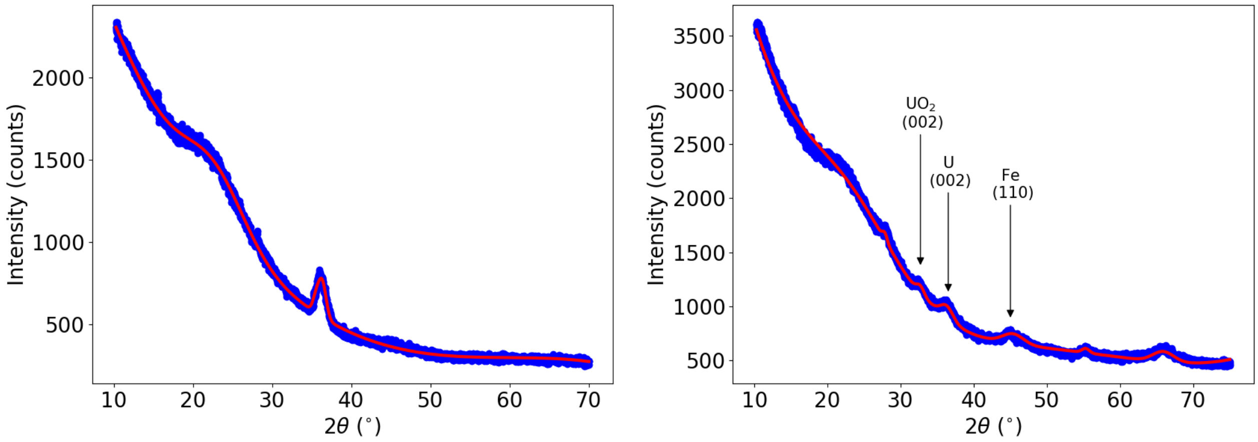

(a) (b)

Figure 3.14: X-ray diffraction from iron-based samples d_U= 3.8 nm. The fit (red) is composed of a fourth order polynomial, to represent the background, and Gaussian peaks. a) High angle $\theta - 2\theta$ scan. b) GIXRD where ω = 1.0°.

As the uranium layer is systematically changing across the sample series, it is this texture in which we are interested. Powder diffraction data for uranium shows three important peaks clustered around 36°. There is (110) centred at 34.8°, (021) at 35.5° and the (002) peak found at 36.3° [114] which is shown in fig.3.15.

As the angle between the incoming x-ray beam and the sample surface is increased, the peak in the region of the uranium triplet becomes more pronounced. However, only one peak is observed. It is expected that any peak observed in a thin film is broadened due to the low

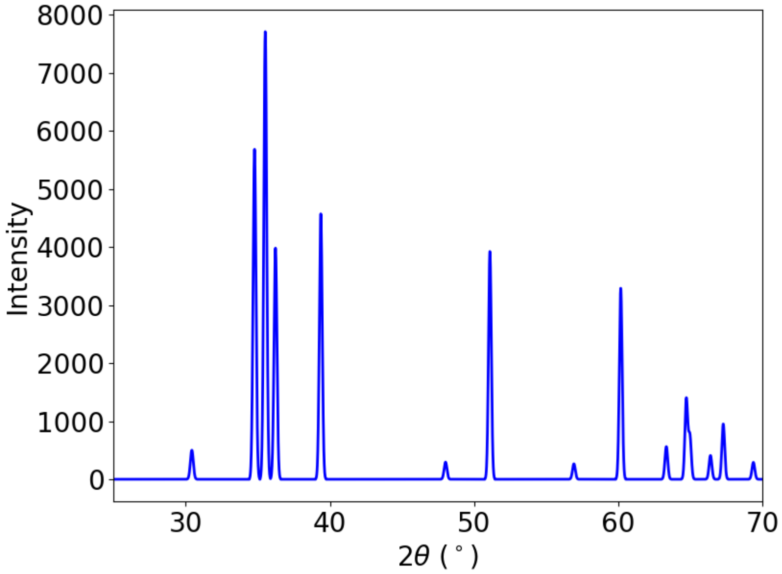

Figure 3.15: Bragg peaks from powder diffraction of α-U, measured at room temperature. The U triplet can be seen around 36° degrees, with the strongest peak being the (021) reflection. Taken from ref. [114].

Incident angle	I_0	x_0	FWHM
0.7	110 ± 3	36.45 ± 0.02	2.09 ± 0.07
1.0	123 ± 3	36.39 ± 0.02	2.03 ± 0.06
10.0	352 ± 8	36.01 ± 0.02	1.57 ± 0.05
HA	246 ± 2	36.16 ± 0.01	1.44 ± 0.02

Table 3.6: Fitted parameters of a single Gaussian fit to U peak for sample SN1219.

thickness of the scattering material, which may suggest that only one peak from the triplet is present. However by fitting a single Gaussian to each sample, it was determined the centre position of the singular peak did not line up with any of the triplet peaks. This suggests that the single peaks observed may be a convolution of the uranium triplet. Peak intensity, positions and full width half maximum (FWHM)- given by $2\sigma\sqrt{2\ln 2}$, where σ is the standard deviation determined from the fit - based on a single peak fit are listed in table.3.6.

In order to determine the composition, the single peak was fitted with three Gaussians. The centre of these three were fixed at 34.8°, 35.5° and 36.3°, i.e. the U (110),(021) and (002) peaks respectively. By keeping these positions fixed, the relative intensities and widths of the three could be determined. Fig.3.16 show the three peak fits and the constituent parts for each scan. For this constrained fit, the background is given by a second order polynomial. At all incident

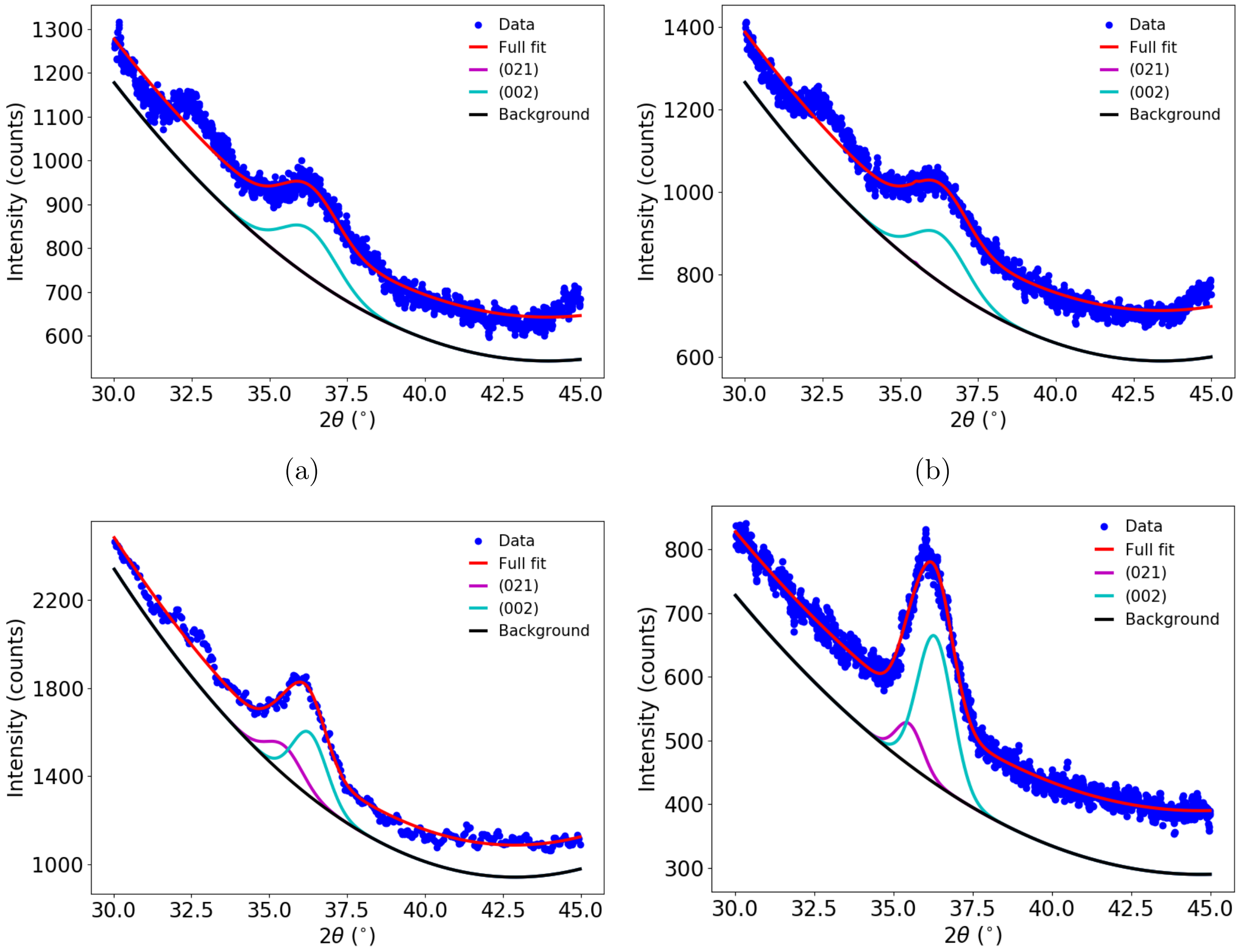

(a)

(b)

(c)

(d)

Figure 3.16: Grazing incidence and θ–2θ scans with a combined fit (red) to the peak corresponding to the uranium triplet positions. The fit is comprised of a polynomial background (black), peak centred at (021) position (magenta) and peak centered at (002) position (cyan). The (110) peak is not included as it cannot be observed over the background on any scan. a) $\omega = 0.7°$ b) $\omega = 1.0°$ c) $\omega = 10.0°$ d) θ–2θ scan. Components of fit offset vertically for clarity.

angles, there is a clear contribution from the (002) peak. At $\omega = 10°$ and in the high angle scan, there is also a smaller contribution from the (021) peak. This disappears at low angles, which is likely due to the reduction in total intensity. It should be noted there is a small peak at ∼32.7° which is not included in the fit. It was determined that this would serve to only shift the fit more towards a contribution from the (002) reflection and would therefore not change the overall conclusions from this analysis. The peak intensity and FWHM for each of the three reflections can be found in table.3.7. From this data, it appears that the iron samples series has a uranium layer preferentially oriented in the [001] direction, with some orientation in the [011] direction. This is unexpected as previous XRD studied on U/Fe multilayers observed purely polycrstalline behaviour [115]. However, these multilayer samples were not capped and ended with an iron layer. Other studies where samples were capped and buffered with Nb, U diffraction peaks could not be observed over satellite peaks from the Nb buffer, [116].

In fig.3.14b, there is a peak at 32.7° which was identified as UO_2. This is not unexpected given the degradation of the sample at the time of measurement. Visually, it appeared that around a third of the film had peeled off, allowing oxygen to permeate into the sample. However, the presence of UO_2 is unlikely to have any effect on the orientation of the remaining U. We can also be confident that there was little to no trace of UO_2 when magnetic characterisation and transport measurements were taken.

Angle	(110)		(021)		(002)	
(°)	I_0	FWHM	I_0	FWHM	I_0	FWHM
0.7	-[2]	-	-	-	115±4	2.02±0.07
1.0	-	-	-	-	125±2	1.97±0.06
10.0	-	-	1302±10	1.35±0.13	290±10	1.31 ± 0.06
HA	-	-	64±3	0.94±0.05	230±2	1.29±0.02

Table 3.7: Fitted values of the peak intensity and FWHM for the (110),(021) and (002) peaks in SN1219 using a three Gaussian fit.

3.2.2.4 Ni-based Layers

Looking at the high angle data for the nickel-based samples, fig.3.17a, there is a sharp peak at 38.205 ± 0.001° which comes from the niobium cap, with a shoulder at 36.5 ± 0.02°. There are five peaks on and around the shoulder. These peaks are due to interference of x-rays within the Nb capping layer and cover the underlying uranium peak, similar to those observed in ref. [116]. As in the iron case, grazing incidence scans provide more information about the structure of the film, as peaks from the uranium, niobium and nickel can all be observed, fig.3.17b. There appears to be no presence of UO_2 in this sample.

From the single peak fits, listed in table 3.8, it appears that the uranium peak is centred past the triplet positions. This is likely due to convolution with the nearby niobium peak. As with the previous sample set, the total fit consists of a polynomial background and Gaussians

---

[2] A blank entry corresponds to an unsuccessful fit of the given peak.

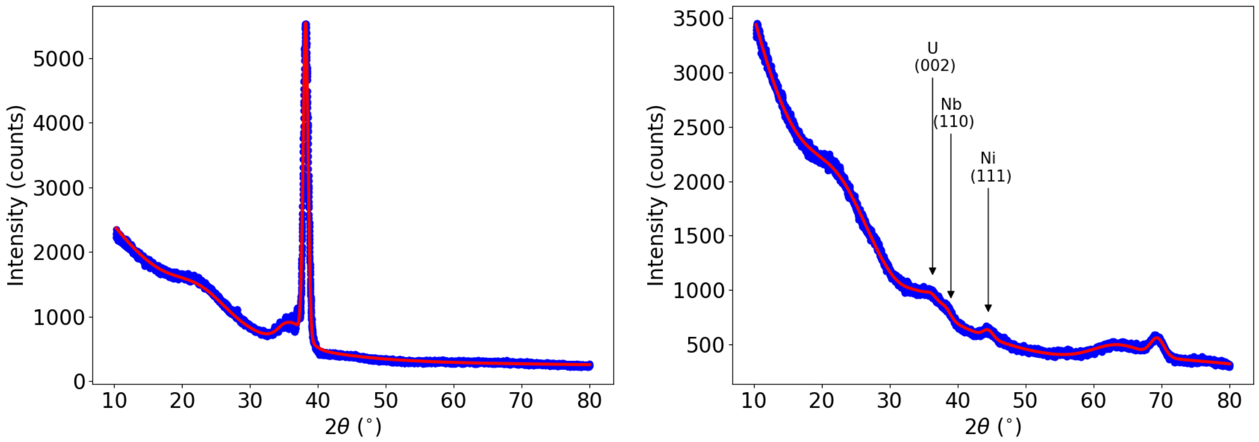

(a) (b)

Figure 3.17: XRD data on sample SN1329, $d_U = 6.9\,\text{nm}$. a) $\theta - 2\theta$ data (blue) fitted with two Gaussians (red) on top of a polynomial background. b) Grazing incidence XRD at $\omega = 1.0°$.

centred at 34.8°, 35.5° and 36.3°. Each fit also required an extra peak to account for the contribution from the Nb cap.

Incident angle	I_0	x_0	FWHM
0.5	162 ± 6	36.40 ± 0.03	2.57 ± 0.07
0.7	263 ± 6	36.45 ± 0.02	2.57 ± 0.04
1.0	242 ± 6	36.25 ± 0.02	2.57 ± 0.05
1.2	242 ± 6	36.37 ± 0.02	2.52 ± 0.04
HA	444 ± 6	36.49 ± 0.02	2.12 ± 0.03

Table 3.8: Results from single Gaussian fit on XRD and GIXRD data for nickel samples SN1329.

When fitting with three peaks, fig.3.18, there appears to only be a contribution to the uranium peak from the (002) peak at all angles[3]. Neither the U (110) nor U (021) peaks can be observed above the background. It may be the case that the convolution with Nb peak is masking contributions from these peaks, but even in that case, they would most likely be significantly weaker than the (002) peak. This implies that the U layer in the Ni samples series is oriented in the [001] direction. However, it cannot be said with complete certainty that there is no contribution from any other direction.

---

[3] Intermediate angle scan (10°) is not used here. This is due to an offset in peak position due to a misalignment of the manual sample stage.

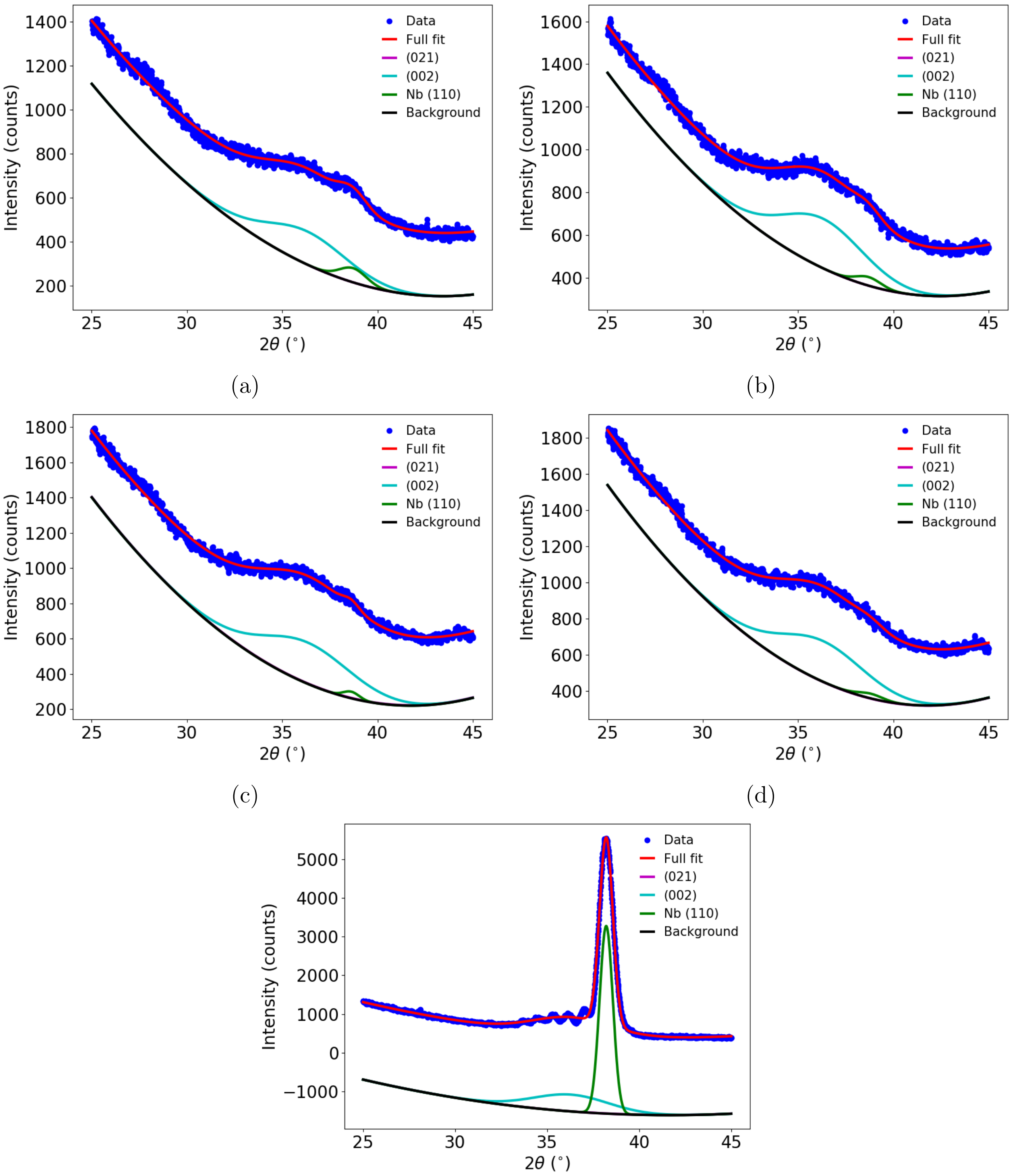

(a) (b) (c) (d) (e)

Figure 3.18: Grazing incidence and θ–2θ scans with a combined fit (red) to the peak corresponding to the uranium triplet positions. Components of the fit are polynomial background (black), peak centred at (021) position (magenta), peak centered at (002) position (cyan) and Nb (110) (green). The (110) peak is not included as it cannot be observed over the background on any scan. a) $\omega = 0.5°$ b) $\omega = 0.7°$ c) $\omega = 1.0°$ d) $\omega = 10.0°$ e) θ–2θ scan. Components of fit offset vertically for clarity.

Angle	(110)		(021)		(002)	
(°)	I_0	FWHM	I_0	FWHM	I_0	FWHM
0.5	-	-	-	-	149±17	5.8±0.3
0.7	-	-	-	-	244±6	5.95±0.10
1.0	-	-	-	-	265±7	6.43±0.12
1.2	-	-	-	-	237±7	5.91 ± 0.11
HA	-	-	-	-	405±10	4.69±0.11

Table 3.9: Fit parameters for three U peak fit to Ni XRD and GIXRD measurements.

3.3 Conclusion

Fe/U and Ni/U bilayer systems, as well as Cu-U and Ni-U alloys, were easily fabricated using a DC magnetron sputtering system. These samples were readily characterised through the use of x-rays. XRR provided information on the thickness of layers and the interfacial roughness for every bilayer sample grown. For both the iron and nickel samples sets $\Delta d_{\mathrm{U}} \approx 0.5\,\mathrm{nm}$ between consecutive samples, as designed. The thickness of the ferromagnetic layer was determined to remain roughly constant over each sample series, as does the FM/U interfacial roughness.

From the XRD and GIXRD data it appears that uranium grown on top of iron exhibits a mixture of [011] and [001] orientation. For nickel based samples, the system is preferentially orientated in the [001] direction. However, due to the small volume of material, and resulting low intensity, there is a possibility that other orientations are present. The importance of these results will be addressed in the following chapters.

Chapter 4

Vibrating Sample Magnetometry

4.1 Theory

The vibrating sample magnetometer (VSM) is a technique which allows the magnetic properties of a sample to be investigated. The magnetisation of the sample is measured by driving a sample in a uniform applied magnetic field at a constant frequency [117,118]. The sample is suspended between the poles of an electromagnet. The sinusoidal motion of the magnetisation induces an AC voltage in pick-up coils situated around the sample, which is based on Faraday's law,

$$V = -\frac{\mathrm{d}\Phi_B}{\mathrm{d}t}, \tag{4.1}$$

where V is the induced voltage and Φ_B is the magnetic flux. The Biot-Savart law

$$\mathbf{B} \cdot \mathbf{m} = I\Phi_B, \tag{4.2}$$

states that the flux generated in the pick-up coil due to a magnetic moment $\mathbf{m}$ as the external magnetic field $\mathbf{B}$ is applied can be related to the current I in the pick-up coil. Combining eqns.4.1 & 4.2 produces

$$V(t) = mG(\mathbf{r})v(t), \tag{4.3}$$

where $G(\mathbf{r}) = (d/dz)(B_m(\mathbf{r})/I)$ and is related to the effect of the sample position on the output signal [119]. The velocity of the sample around an equilibrium position is given by

$$v(t) = A\omega\cos(\omega t). \tag{4.4}$$

The detected voltage then becomes

$$V = mG(\mathbf{r})A\omega\cos(\omega t). \tag{4.5}$$

This signal is measured using lock-in detection.

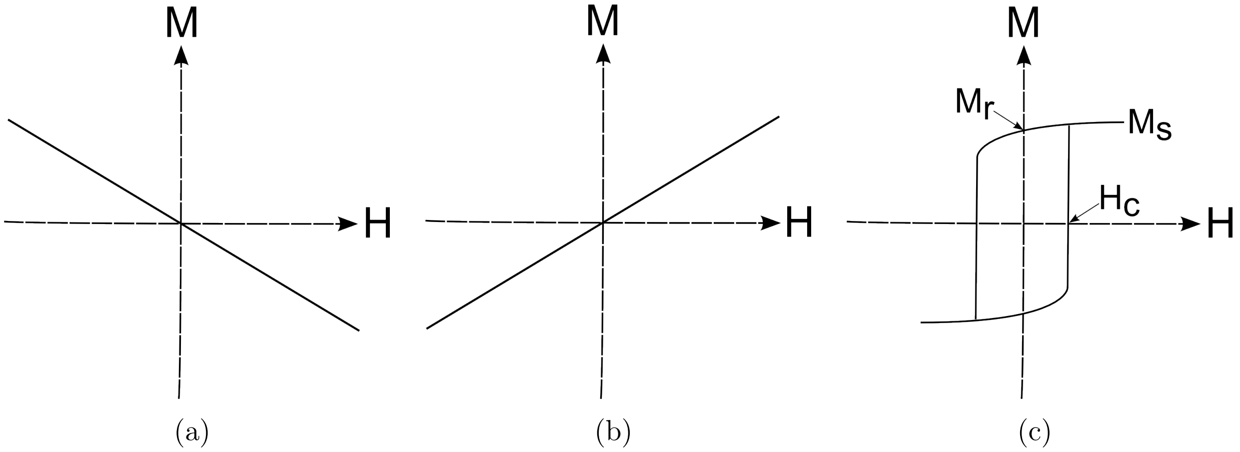

Figure 4.1: Typical M(H) loops for different types of samples (a) Diamagnetic M(H) loop (b) Paramagnetic loop in low field limit (c) Ferromagnetic hysteresis loop where M_s is saturation magnetisation, M_r is the remanent magnetisation and H_c is the coercive field.

The VSM produces an $M(H)$ curve, the form of which is different for diagmagnetic, paramagnetic and ferromagnetic materials, as illustrated in fig.4.1. Ferromagnetic materials display a distinctive M(H) loop, fig.4.1c. At high fields, the magnetic moments are aligned with the field direction. This referred to as the saturation magnetisation M_s. As the field is reduced to zero, there is some proportion of the moments are aligned within the sample. This is known as the remanent magnetisation. If the field is aligned along the easy axis of magnetisation, M_r will be large, resulting a 'more square' loop. In the case of hard axis alignment, the M(H) loop will more tilted, with a smaller M_r value. The difference between these two cases will be discussed in greater detail in section 4.3. The point at which the magnetisation crosses the x-axis is known as the coercive field H_c. Beyond the coercive field, the magnetisation is flipped 180° to align with the direction of the applied magnetic field.

4.2 Set-up

In this work, a commercial Lakeshore 7307 system was used to investigate the anisotropy of each bilayer sample. The configuration of this particular system is shown by Fig.4.2. The Lakeshore

7307 uses 7-inch electromagnets which can reach a maximum field of 1 T. The system uses 730ESC pick-coils which can detect a magnetic moment in the range of 5×10^{-9} – 1 Am^2. The applied magnetic field is measured using a Hall probe attached to a Lakeshore Model 450 Guassmeter.

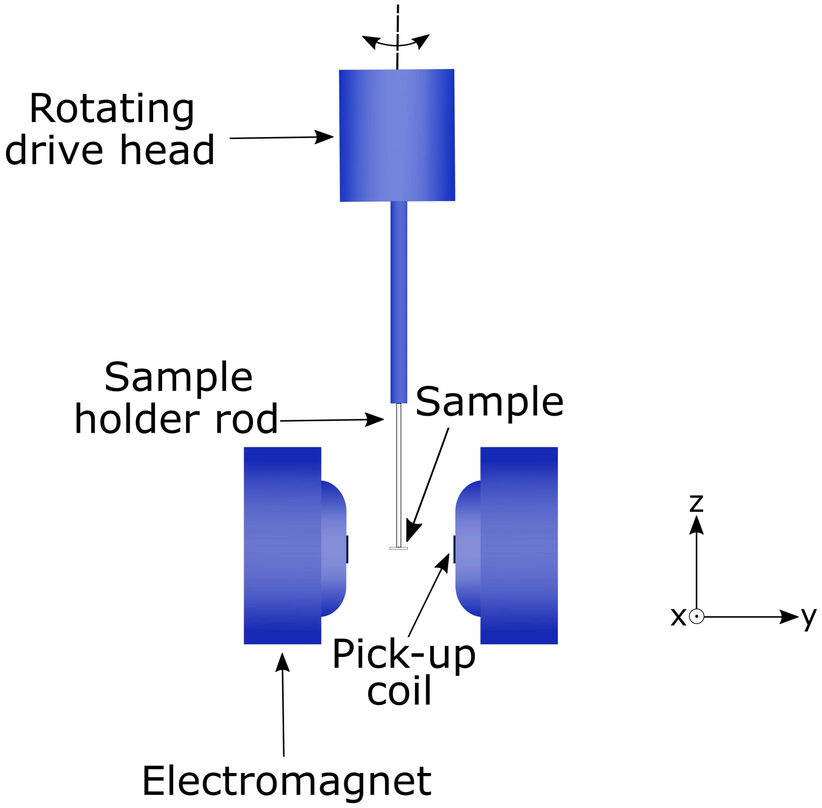

Figure 4.2: Schematic illustrating the sample set up for the Lakeshort 7307 system. Sample is suspended from the rotating drive head between the poles of an electromagnet.

The sample is positioned so that the moment measured in the z and y directions is maximised and is minimised in x. This allows the measurement to be insensitive to small perturbations in the sample position [117]. Two sample rods were specially designed using suprasil quartz to reduce background noise, one for in-plane measurements and the other for out-of-plane, as in fig.4.3. A small amount of Dow Corning vacuum grease was used to attach the sample to the suprasil sample rod as this has a low background compared to the sample and sample holder.

In the in-plane configuration, the drive head was rotated in 10±1 ° steps from -10 ° – 190 °, to allow the sample anisotropy to be probed. The sample was held with the plane of the film perpendicular to the magnetic field for the out-of-plane configuration. All measurements were conducted at room temperature.

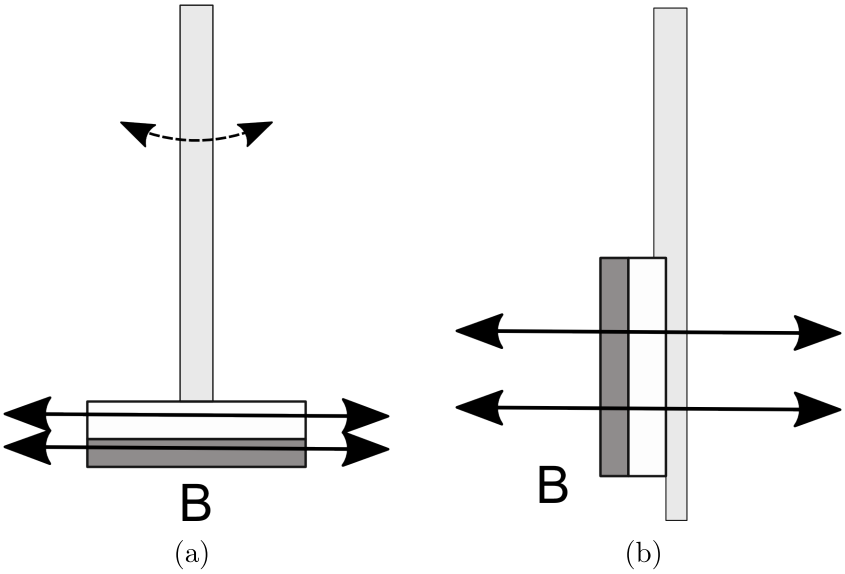

(a) (b)

Figure 4.3: Sample orientations used for magnetometry measurements(a) In-plane (b)Out-of-plane.

For all measurements in the in-plane configuration, the field was swept ±200 mT. For iron/uranium samples $\leq$ 3.8 nm, the field was stepped in ~2 mT increments at all points. Measurements on nickel-based samples and iron samples with $d_{\mathrm{U}} > 3.8$ nm swept the field from 200 - 50 mT in 5 mT steps, then ±50 mT in 1 mT steps. This sweeps allowed the region of magnetic switching to be probed more clearly. This was only carried out on the thicker iron samples due to a 'custom loop' feature in an updated software version.

In addition to these in-plane measurements, all samples were studied in the out-of-plane geometry, with the field swept to ±500 mT in equal steps.

4.3 Results

4.3.1 Iron Bilayers

Iron-based bilayers were the first to be studied. Some examples of hysteresis loops for $d_{\mathrm{U}} =$ 0 nm, 1.7 nm, 3.8 nm and 6.5 nm at various angles can be seen in fig.4.4. Figs.4.4b & 4.4c present the data taken using the equal step loops, where as fig.4.4a & 4.4d both utilised the custom loop. It is clear that the data taken using the custom loop feature is cleaner around the remanent magnetisation.

In all data presented in fig.4.4 there are obvious changes in the shape of the hysteresis loops

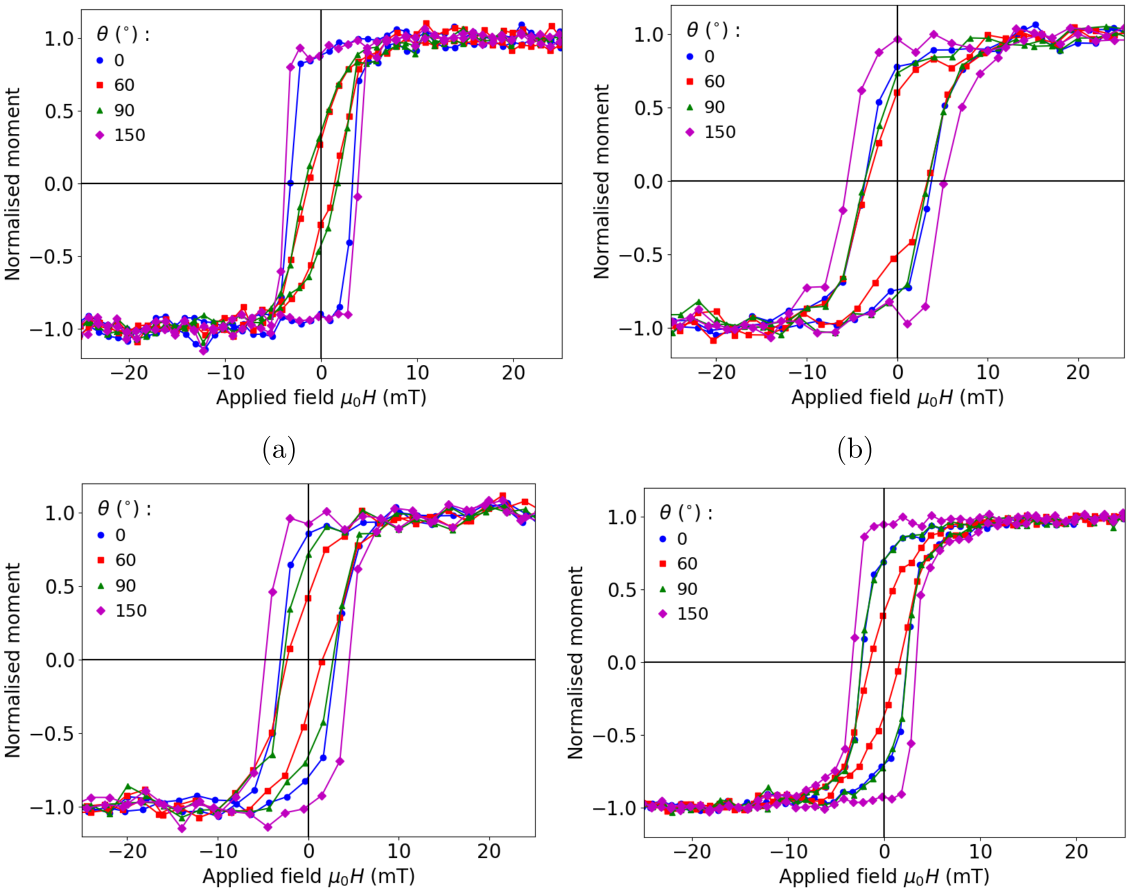

(a)

(b)

(c)

(d)

Figure 4.4: Normalised hysteresis loops for varying uranium thicknesses a) Iron only, b) $d_{\mathrm{U}} = 1.7\,\mathrm{nm}$, c) $d_{\mathrm{U}} = 3.8\,\mathrm{nm}$ and d) $d_{\mathrm{U}} = 6.5\,\mathrm{nm}$. Data constrained to $\pm 25\,\mathrm{mT}$ to clearly illustrate the change in behaviour with angle.

with angle. The loop at 150° exhibits easy axis behaviour as it is has the largest coercive fields and remanent magnetisation. This is characterised by the loop appearing more square than the others. The thin, curved loops at 60° suggest that this is the magnetic hard axis. Here, the coercive fields and remanent magnetisation are lowest.

Before each sample was studied, a scan of the background moment from the sample rod was taken. The background was seen to be diamagnetic and isotropic. These background scans were then subtracted from each data file. To remove any further diamagnetic background attributed to the substrate, a linear fit was applied to the saturated region and then subtracted. Once flattened, another linear fit was taken on the positive and negative saturation regions to

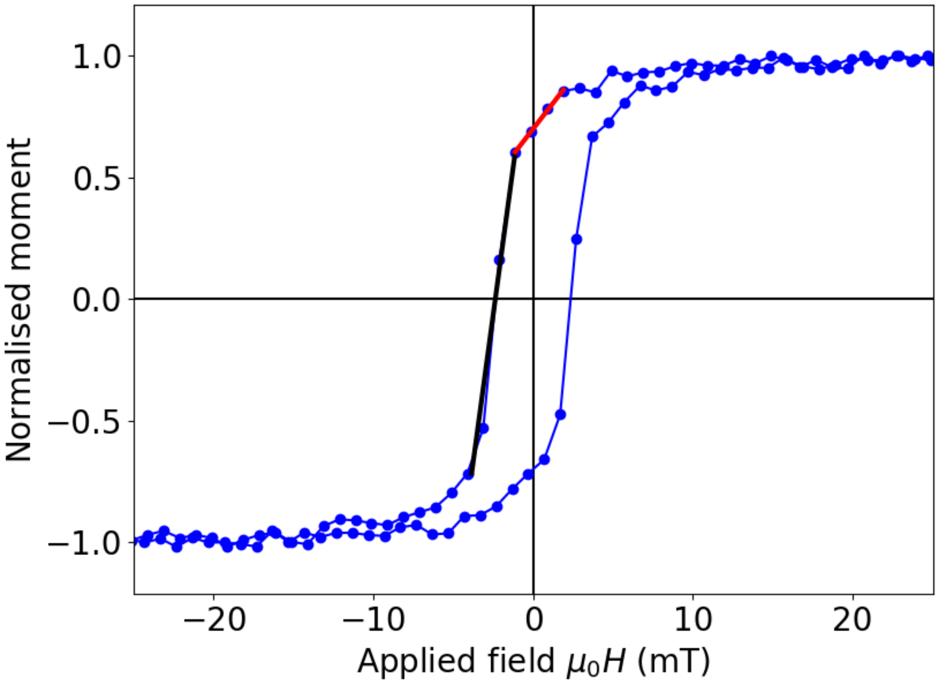

Figure 4.5: Hysteresis loop for $d_U = 6.5\,\text{nm}$ at 0°. The fit crossing the y-axis (red) gives a value for M_r^*. The fit through the x-axis (black) is used to determine $\mu_0 H_c$.

determine the saturation magnetisation M_s. M_s^{Pos} and M_s^{Neg} were averaged to give M_s. The data were then normalised by M_s. To determine the normalised remanent magnetisation M_r^* and the coercive field $\mu_0 H_c$ straight lines were fitted to the appropriate regions for each case, shown as the red and black fits in fig.4.5 respectively. The y- and x-axis intercepts gave M_r^* and $\mu_0 H_c$. For each quantity, the positive and negative values were averaged.

$\mu_0 H_c$ and M_r^* were determined for every angle. Both quantities exhibit uniaxial behaviour and are minimised for the hard axis and maximised at the easy axis. The evolution of both as function of angle for four thickness of uranium can be seen in fig.4.6. Each sample exhibits clear uniaxial anisotropy, with the easy axis between 140 ° and 160 ° and hard axis behaviour around 40 ° – 70 °. As the iron layer is expected to be completely polycrystalline based on the low intensity of the (110) peak seen by XRD and GIXRD in chapter 3, this anisotropy is most likely due to the oblique angle of incidence of the sputtered atoms [28–32]. There is also a peak around 60 °, which has been attributed to stray magnetic fields in the sputtering chamber during growth. The anisotropy of each sample was quantified in terms of the range of $\mu_0 H_c$ and M_r^* as well as their averages. The range was taken as the easy axis $\mu_0 H_c$ or M_r^* minus the corresponding hard axis value. The change in these quantities with increasing d_U can be seen in fig.4.7.

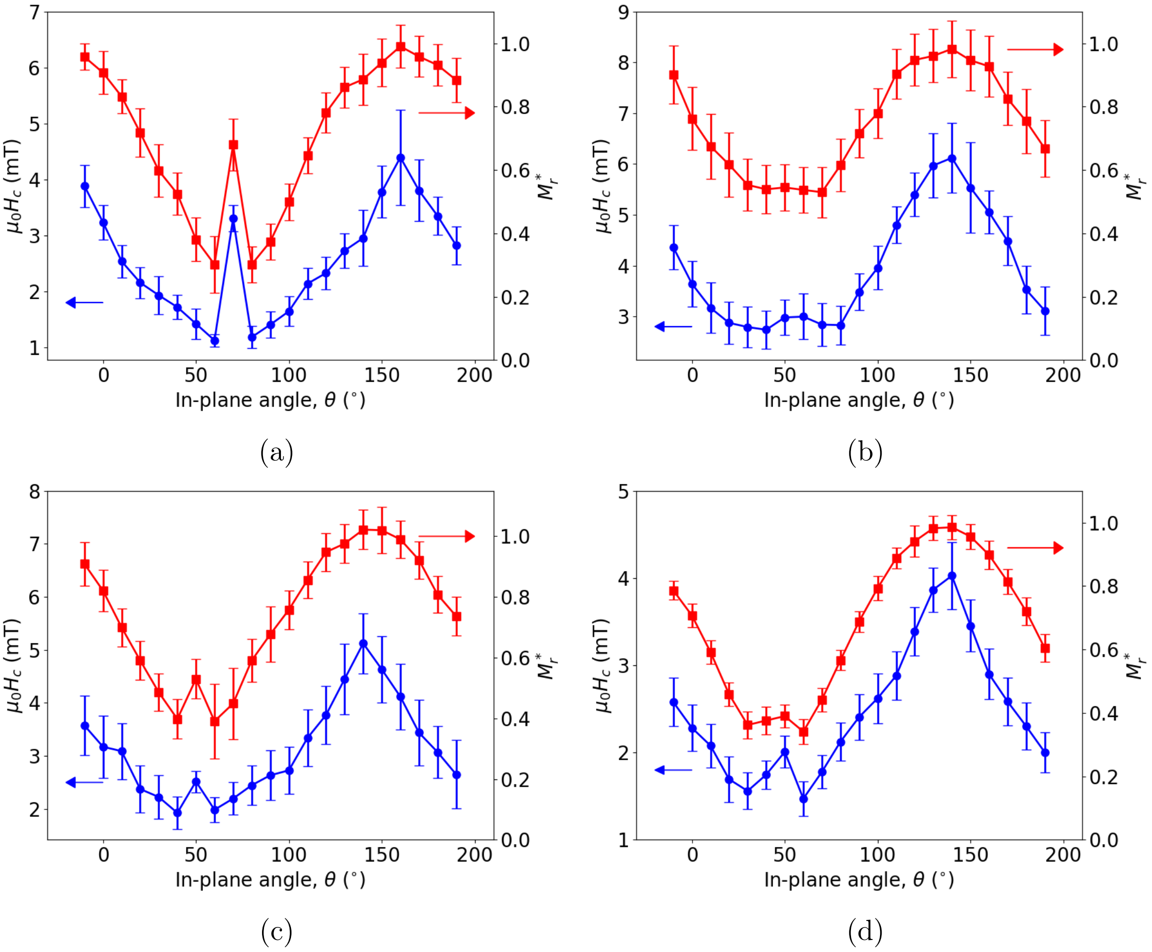

(a) (b)

(c) (d)

Figure 4.6: Evolution of both $\mu_0 H_c$ (blue circle) and M_r^* (red square) with in-plane angle. All samples exhibit easy and hard axis begaviour around 150° and 50° respectively. Each graph repsents a different uranium thickness a) d_{U} $=0\,nm$, b) d_{U} $=1.7$ nm, c) d_{U} $=3.8$ nm and d) d_{U} $=6.5$ nm.

For $\mu_0 H_c$, seen in fig.4.7a, the range (blue) and average (red) both appear to oscillate with increasing d_U. This oscillation can also be seen in the range of remanent magnetisation, shown in blue in fig.4.7b. However, while the average remanent magnetisation (fig.4.7b red squares) appears to oscillate it does not have the same periodicity as the other quantities. It is not clear what may cause this faster oscillation. However, even through it appears that M_r^* oscillates, given the large errors, the change across the series may result from natural variation due to noise.

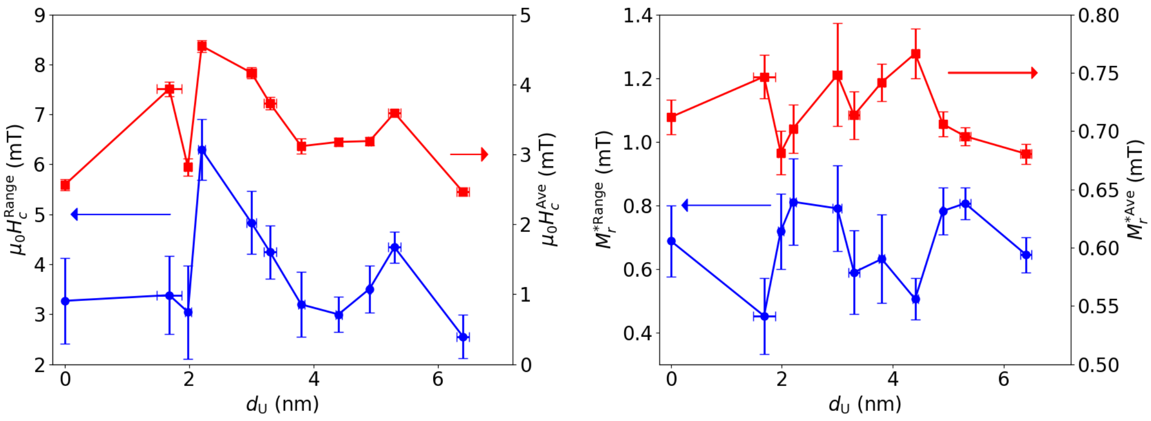

(a) (b)

Figure 4.7: Qualitative measure of the magnetic anisotropy of iron/uranium bilayers as a function of uranium thickness, a) The range (blue circles) and average (red squares) of the coercive field. The forms of the two quantities mirror each other closely with a period of ~3 nm. b) Range and average of the remanent magnetisation. The range appears to oscillate with a period similar to the coercive field but the average portrays a shorter periodicity, with a slightly different form.

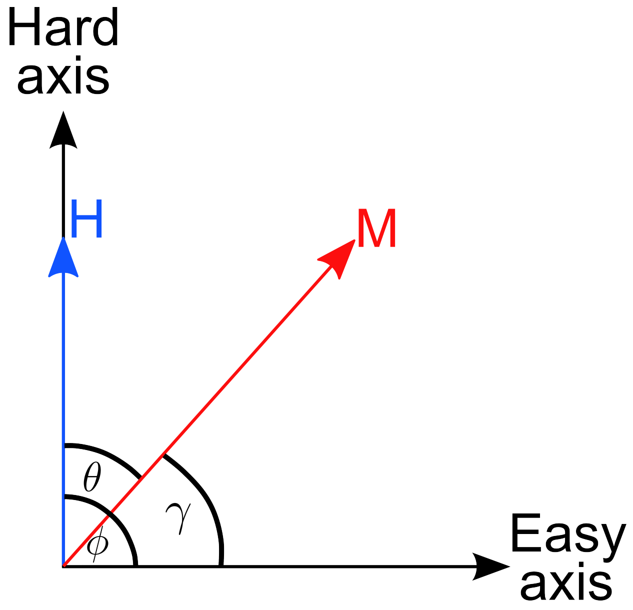

Figure 4.8: Geometric representation of a thin film system with uniaxial anisotropy and the magnetisation lying in the plane of the sample.

In addition to these qualitative measures of the anisotropy in Fe/U bilayers, the effective anisotropy constant K_{eff} can be determined from the hysteresis loops. The effective in-plane anisotropy constant determined here followed the analysis set out in refs. [19] & [94]. In this work, K_{eff} is defined such that it encompasses all components of the anisotropy that may be present in the system, such as the uniaxial anisotropy due to oblique incidence deposition. For a thin film, the magnetisation can be described by the configuration shown in fig.4.8, the total energy density is given as

$$\varepsilon = -\mu_0 \vec{H} \cdot \vec{M} + K_{\text{eff}} \sin^2 \gamma, \tag{4.6}$$

where $\gamma = \phi - \theta$. In this equation, the first term is the Zeeman energy and the second is a uniaxial anisotropy term. As the magnetic field was applied purely in-plane, the magnetisation is assumed to also lie solely in the plane of the film. The demagnetisation energy, as given by eqn.2.12, will go to zero when M lies in the plane of the film, and is therefore not required. Eqn.4.6 can then be expanded to

$$\varepsilon = -\mu_0 H M_s (\cos\phi \cos\gamma + \sin\phi \sin\gamma) + \frac{K_{\text{eff}}}{2}(1 - \cos 2\gamma), \tag{4.7}$$

Minimising eqn.4.7 with respect to γ gives

$$\mu_0 H M_s \sin(\phi - \gamma) = K_{\text{eff}} \sin 2\gamma, \tag{4.8}$$

$$H = \frac{K_{\text{eff}}}{\mu_0 M_s} \frac{\sin 2(\phi - \theta)}{\sin\theta}. \tag{4.9}$$

If H is applied along the hard axis, which is assumed to be perpendicular to the easy axis[1] i.e. $\phi = 90°$, then it can be assumed that θ is small, giving:

$$H_s = \frac{2K_{\text{eff}}}{\mu_0 M_s}, \tag{4.10}$$

where H_s is the field at which the magnetisation saturates. As the output from the VSM returns the magnetic moment, m (Am^2), to determine the anisotropy constant we must convert to magnetisation, M (Am^{-1}). For the iron samples, this has been split into two cases, 'd_{Fe} only' which assumes that only the iron layer is important to the magnetisation, and '$d_{\text{Fe+U}}$' in which the volume of both U and Fe layers are included in the conversion to M, due to the expected presence of induced magnetism in the U over layer. It is not clear how far through the U layer

---

[1] In actuality, this is not always the case in data collected in this work. However, as the angle between the hard and easy axis varies by no more than ±10 ° between samples, which is not enough to cause a significant change, we can keep this assumption.

the magnetisation may be expected to persist so the total U volume has been taken for this case. However, the magnitude of the moment induced in the U layer is significantly smaller than that of iron (at most $0.135\,\mu_B$ compared to $2.2\,\mu_B$ [13, 15]) . This would suggest that only the iron layer needs to be considered. However, both cases are still include for a thorough comparison, illustrated in fig.4.9. For both 'd_{Fe} only' and '$d_{\mathrm{Fe+U}}$' the oscillations are still clear.

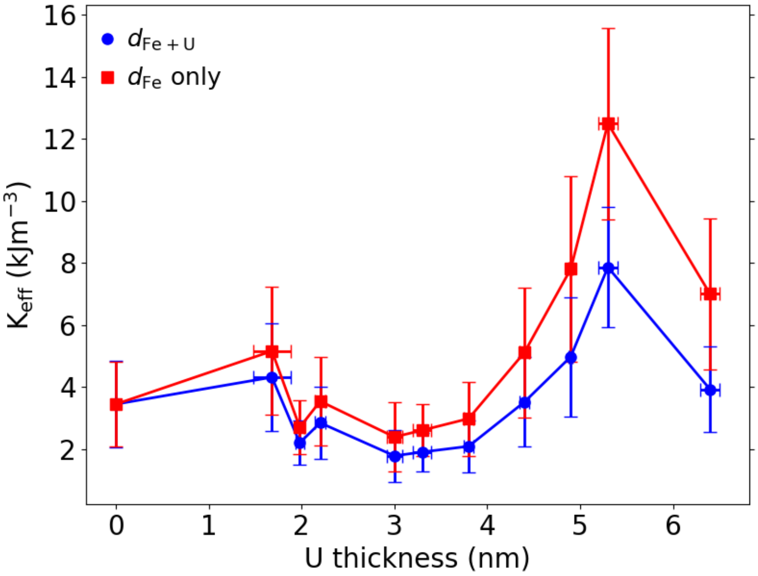

Figure 4.9: Effective anisotropy constant for the case where only the iron layer is considered (red square) and where both the iron and uranium layers contribute due to induced magnetic moments (blue circle). Lines are guide for the eye.

When comparing with fig.4.7a, similar features can be observed with a minimum at d_{U}=2.0 nm and a peak at d_{U}=5.3 nm. This suggests that the average and range of coercive field is a good metric for determining the changes in anisotropy within the series. Unexpectedly, the peak at d_{U}=2.2 nm is not as pronounced as in the coercive field.

The large errors are a consequence of judging the saturation field by eye. When the determination of the saturation field was automated, the value of H$_s$ was often over estimated in some samples, so the 'by eye' method was determined to be more consistent. However, in some cases it appeared that the magnetisation was saturated, only for the two halves of the sweep to separate, possibly due to noise, resulting in larger errors to compensate a possibly underestimation of the saturation field.

Typically, it would be expected that the cubic anisotropy constant K_{c1} for iron would be around $4.8 \times 10^5\,\mathrm{Jm^{-3}}$ [15]. Here, the anisotropy ranges from a factor of 3 to a factor of 20 smaller. The reduction in anisotropy coefficient can be attributed to the origin of the anisotropy.

In this case, the anisotropy will likely originate predominately from induced anisotropy during growth, rather than a strong magnetocrystalline contribution. Additionally, this is a bulk value and even for an single crystal thin film there will be variations in K_{c1}

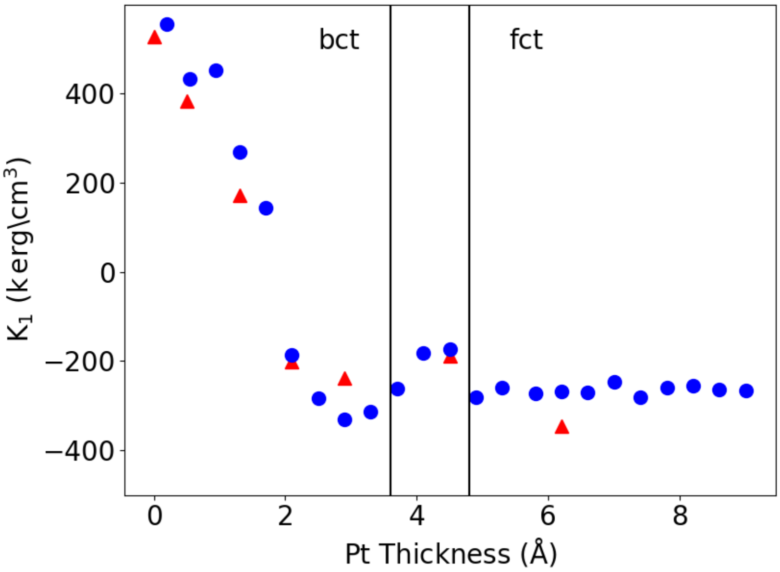

Figure 4.10: Calculated K_{c1} for Fe/Pt hetrostructures, which exhibit an induced magnetic moment in the Pt layer. Data represented by blue circles follows analysis laid out in this thesis. Red triangles represent a second method in which the angle θ was known. The two were found to be in good agreement, giving merit to the method utilised here. Adapted from ref. [94].

The analysis for determining K_{eff} was based on that by the work of Antel *et al.*, which looks as the proximity induced moment in Pt grown on Fe. Comparing $K_{\text{eff}}(d_{\text{U}})$ to the work of Antel *et al.* in ref. [94], replotted in fig.4.10, the anisotropy constant in this work is much lower. This likely due to the samples of Antel *et al.* being (001) oriented and therefore having a cubic anisotropy coefficient which is expected to be largers than the effective coefficient due to induced anisotropy present in samples used in this work. However, it is still interesting to look at the functional form K_{c1} as a function of Pt thickness as a comparison with U. As a function of platinum thickness, the anisotropy constant appears to be non-monotonic, with a small peak around 4 Å which was attributed to a change in crystal structure, from a body-centred tetragonal structure to face-centred tetragonal. Past this transition, K_1 appears to be monotonic, decreasing slowly as Pt thickness increases. A structural transition is unlikely to be case in this work, as the U layer should always be in the orthorhombic α phase at the thickness grown here. However, ideally, to truly rule this out both grazing incidence and high angle XRD would be performed on all samples.

To understand the origins of these oscillations, it is important to first look at variations in the structure of the Fe/U bilayers. It would be expected that an increase in d_{Fe} would result in a larger coercive field[2]. Fig.3.10b in chapter 3 presents the thicknesses determined by GenX fitting of iron against uranium. While there are some variations, the samples with the largest thickness do not correspond to those with the greatest $\mu_0 H_c^{\mathrm{Range}}$ and $\mu_0 H_c^{\mathrm{Ave}}$. In fact, the thickest sample actually exhibits one of the lowest values for both these quantities. Another factor which may be expected to affect the coercive field is roughness at the Fe/U interface. It is assumed that all domains within each sample are of the same type – separated by either Néel or Bloch walls – and therefore the relation of roughness to coercive field should be monotonic [120]. Fig.3.10a illustrates the rms roughness at the Fe/U interface, which appears to be roughly monotonic. Comparisons of the form of roughness as a function of uranium thickness with that of the coercive field shows no similar features, ruling out interfacial roughness as a cause of this oscillatory anisotropy. It may also be possible that there is some formation of the magnetic compound $\mathrm{UFe_2}$ in varying quantities at the interface. However, the Curie temperature of $\mathrm{UFe_2}$ is 160K [13], so there would be no contribution to the anisotropy at room temperature. These preceding arguments suggest that the origin of the oscillation is not related to the material physics of the samples.

The period of the observed oscillation is $\sim$3 nm. This is on a similar length scale to the oscillations seen by Wilhelm *et al.* in ref. [13]. While the oscillations in induced moment in ref. [13] are for multilayers systems, it is not unreasonable to assume that a bilayer system would exhibit a damped oscillation of a similar period suggesting a potential connection between the induced magnetic moment and these anisotropy oscillations. Assuming that the induced magnetisation in uranium is locked to the magnetisation of the iron, i.e. always aligned parallel or anti-parallel to one another, the oscillatory behaviour of the induced magnetisation may explain the oscillations in anisotropy.

As mentioned in section 2.1.4.1, there are systems which exhibit oscillatory behaviour when increasing the thickness of the non-magnetic layer. These are FM/NM multilayers which exhibit the oscillatory exchange coupling [3–5]. It was seen that many of the transition metals displayed this coupling with varying periodicity. When grown on Co, Cr had the longest period of 1.8 nm [5]. Heavy metals such as Pt, Pd and Au do not show any in-plane coupling, but do exhibit similar coupling in out-of-plane measurement. It is clear that in the Fe/U systems the oscillations cannot come from oscillatory exchange coupling as there is no secondary ferro-

---

[2] While this is generally true, it should be noted that the often the dependence of H_c on the thickness is non-monotonic, though not oscillatory. Often there is an initial increase at low film thickness, followed by the coercivity plateauing at higher thickness [120].

magnetic layer for the iron to couple to. However, the quantum well states which govern these oscillations may be responsible. As there is thought to be strong hybridisation between the Fe $3d$ and U $5f$ states [14], it is not unexpected that QWSs in U may result in oscillations of the magnetic anisotropy. The increased periodicity of these oscillations compared to those in lighter metals will come from the difference in the Fermi and Brillouin zone boundary wavevectors of uranium. As the orientation along the z-direction was found to be a mixture of [011] and [001], the period of a quantum well state oscillation in this systems may be calculated from eqn.2.25. However, preliminary calculations for different orientations of single crystal α-U suggest a much shorter period than the one measured here, ranging from $0.1 - 1\,\text{nm}$ [121]. The observation of this longer period may be due to aliasing cause by the large step size of d_{U} between consecutive samples. However, further theoretical work is required to calculate the period of the textured polycrystalline α-U.

If the magnetic anisotropy oscillations originate from quantum well states, it seems likely that there is a link between the induced magnetic moment and these QWSs as they have a similar periodicity, though it is not clear at this stage. To determine whether these oscillations are a result of the induced moment or QWSs, measurements of Ni/U layers were carried out. As Ni/U does not exhibit an induced moment, the presence or absence of oscillations will support one of these cases. The results of these studies can be found in section 4.3.2, following a discussion on the out-of-plane behaviour of the Fe/U series.

Out-of-plane measurements

In the out-of-plane configuration, it was expected that only hard axis behaviour would be observed as typically the thickness of a ferromagnetic layer required to exhibit perpendicular magnetic anisotropy is $<3\,\text{nm}$ [20, 24, 122]. However, for iron/uranium samples this was not the case. In general, the series behaved as expected, with the exception of three samples $d_{\text{U}} = 1.7\,\text{nm}, 4.4\,\text{nm}, 5.0\,\text{nm}$. A comparison of the hysterisis loops from $d_{\text{U}} = 1.7\,\text{nm}$ and $2.2\,\text{nm}$ can be seen in fig.4.11a. The sample where $d_{\text{U}} = 2.2\,\text{nm}$ displays the expected hard axis behaviour, whereas $d_{\text{U}} = 1.7\,\text{nm}$ produces a relatively square hysteresis loop, suggesting an out-of-plane easy axis.

When comparing fig.4.9 with reference to fig.4.11, it might be expected that there is some evidence of this perpendicular magnetic anisotropy. However, there is no clear signature of the out-of-plane anisotropy in the effective anisotropy coefficient, which is to be expected as the method used to determine K_{eff} restricts the magnetisation to lie in the plane of the sample, i.e looking at only the in-plane magnetisation cannot provide an accurate picture of all aspects of

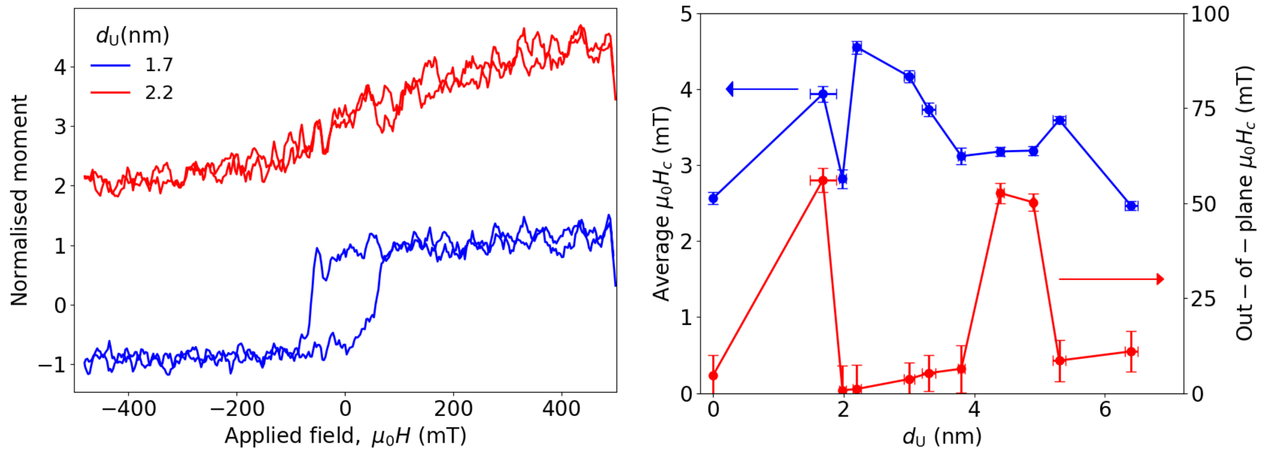

(a)

(b)

Figure 4.11: (a) Out-of-plane hysteresis loops for two samples d_U at 1.7 nm (lower blue loop) and 2.2 nm (upper red loop). Curves are offset for clarity. (b) Comparison of the in-plane H_c^{Ave} (blue) and the out-of-plane coercive field for each sample (red). Lines are guide for the eye.

the sample magnetisation.

The presence of this PMA may be related to the some surface anisotropy at the Fe/U interface. Systems which exhibit PMA can also experience modulations of anisotropy through quantum well states [74]. However, while these states are expected to be present in Fe/U bilayers, the absence and sudden appearance of PMA across the sample series can not be easily explained. It is possible that QWSs at very specific thickness could alter the anisotropy in such a way that the system becomes less anisotropic. When comparing the out-of-plane samples with their corresponding in-plane average coercive field as seen in fig.4.11b, it does appear that samples with a low average also show out-of-plane magnetisation. However, given the small sample set this cannot be said with certainty.

It is possible that the PMA is a result of something other than interfacial anisotropy. As these samples are anti-symmetric ferromagnet/heavy metal systems it would not be unexpected to find chiral spin textures due to the interfacial Dzyaloshinskii-Moriya interaction. It is possible that an IDMI term could cause canting of spins within the system, pulling them out of plane. In the work of Ryu *et al.* in ref. [123], they suggest that in order for IDMI to be exhibited, there must be some proximity induced magnetisation. They also propose that the DMI is proportional to the induced magnetisation. In this picture, we would expect that the uranium thicknesses which exhibit the largest magnetic moments would display DMI, which may be why out-of-plane magnetisation is only found in a subset of the samples. In contrast with this interpretation, theoretical calculations by Yang *et al.*, found in ref. [124], depicted an inverse relationship between the strength of the DMI with the size of the proximity induced magnetisation. However, the strength of the DMI is reduced but only around a third when the moment was increased to $0.4\,\mu_B$, which is significantly larger than expected for uranium. Based on the measurements of Wilhelm *et al.*, it is assumed that the induced moment within any given value of d_{U} should be less than $0.135\,\mu_B$ and therefore would not be large enough to kill any DMI present, thus not explaining the appearance of out-of-plane magnetisation for only three samples. This means PMA should be observed in all samples if it was a consequence of DMI. Work by Rowan-Robinson *et al.* proposes yet another interpretation. In ref. [125], it was observed in Pt(5.4 nm)/Co/Pt(2.6 nm) trilayers that the upper and lower Pt layers exhibited induced magnetic moments of different magnitudes. However, the DMI at the each interface was said to be equal and opposite. This implies that there is not a direct link between the strength of the DMI and the PIM. In the study by Rowan-Robinson *et al.*, a spacer layer of varying thickness was introduced between the Co and upper Pt layers. This saw an increase of the DMI and a reduction of the PIM in the upper Co layer. However, this increase in DMI can be attributed to the increased asymmetry of the system rather than the reduction of the PIM.

As there are no clear conclusion about the role of PIM in the interfacial DM interaction, the involvement of quantum well states is the next consideration. There appears to be no research into the effect, if any, that QWSs may have on interfacial DMI. However, theoretical calculations from Belabbes *et al.* suggest that the strength and chirality of the DMI are dependent on hybridisation of orbitals and the resultant position and filling of the spin-split bands at the Fermi energy [126]. It is known that the presence of QWSs alters the density of states at the Fermi level and are spin dependent. Therefore, systems which exhibit QWS behaviours may produce a DMI which varies in strength. The presence of a DMI which varies in strength would result in a change in the competition with other energy contributions, and may explain why some samples exhibit a preference for PMA.

Unfortunately, based purely on the existence of PMA in a subsection of these sample, there is not enough evidence to draw clear conclusions about the presence of DMI in these systems and would require more investigation.

4.3.2 Nickel Bilayers

To fully understand the role of the induced magnetic moment in the oscillations of anisotropy seen in the iron-based systems, fig.4.9, we look to nickel-based systems, as these are expected to have zero proximity induced magnetisation in the uranium layers.

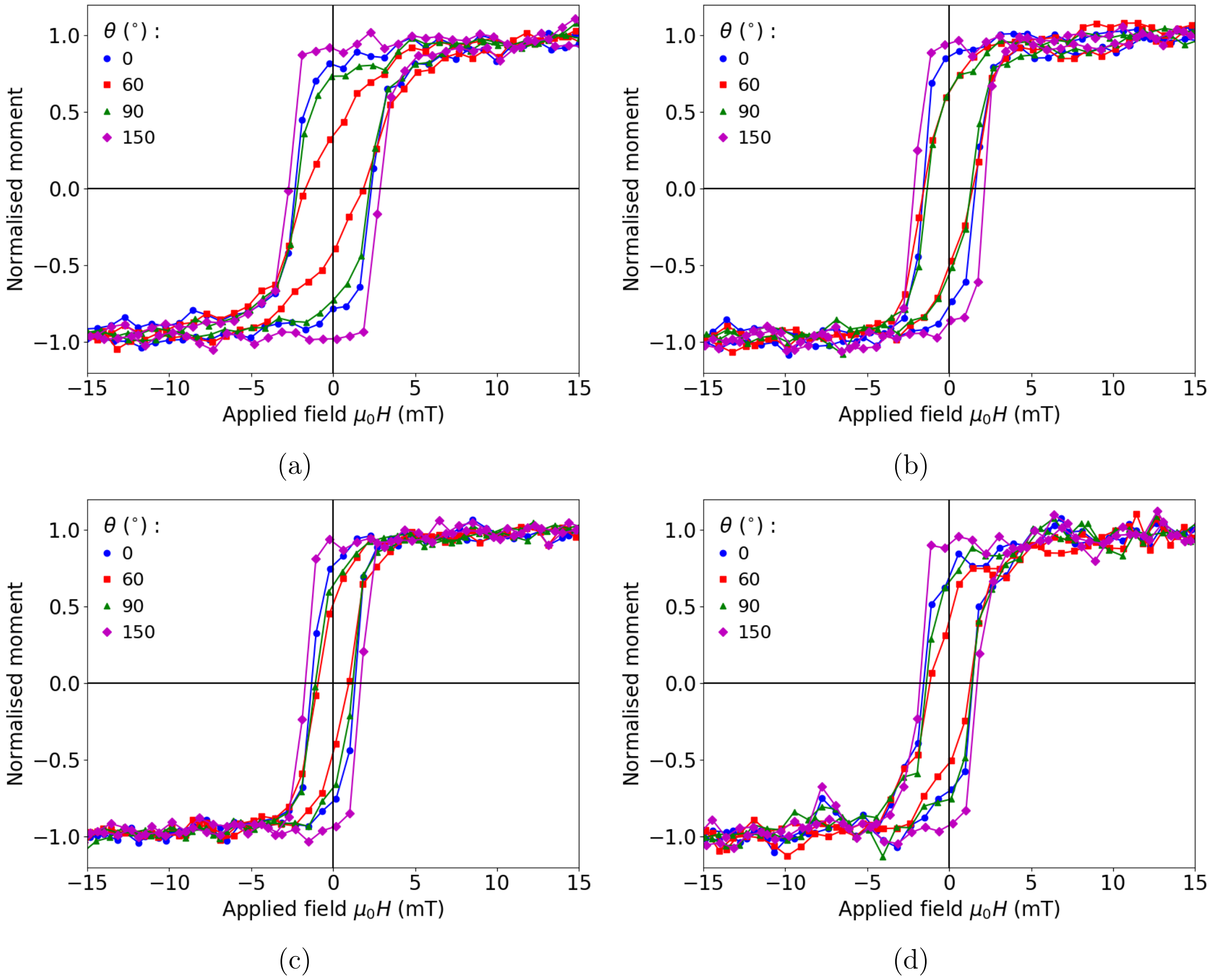

(a)

(b)

(c)

(d)

Figure 4.12: Hysteresis loops for nickel based samples for a selection of in-plane angles. a) Nickel only. b) $d_{\mathrm{U}} = 0.6\,\mathrm{nm}$ c) $d_{\mathrm{U}} = 4.6\,\mathrm{nm}$ and d) $d_{\mathrm{U}} = 7.5\,\mathrm{nm}$.

All samples were analysed using the same method as those in section 4.3.1. For all samples, the VSM ‘custom loop’ feature was used. Fig.4.12 shows hysteresis loops at multiple angles for $d_{\mathrm{U}} = 0$, 0.6, 4.6 and 7.5 nm. When comparing M(H) loops for $d_{\mathrm{U}} = 0\,\mathrm{nm}$, there is obvious switching from hard (∼60°) to easy axis (∼150°). When looking at figs.4.12b, 4.12c & 4.12d, it is clear that the addition of any amount of uranium has a distinct effect. For $d_\mathrm{U} = 0.6$,4.6 and 6.9 nm, the easy and hard axis behaviour become difficult to differentiate.

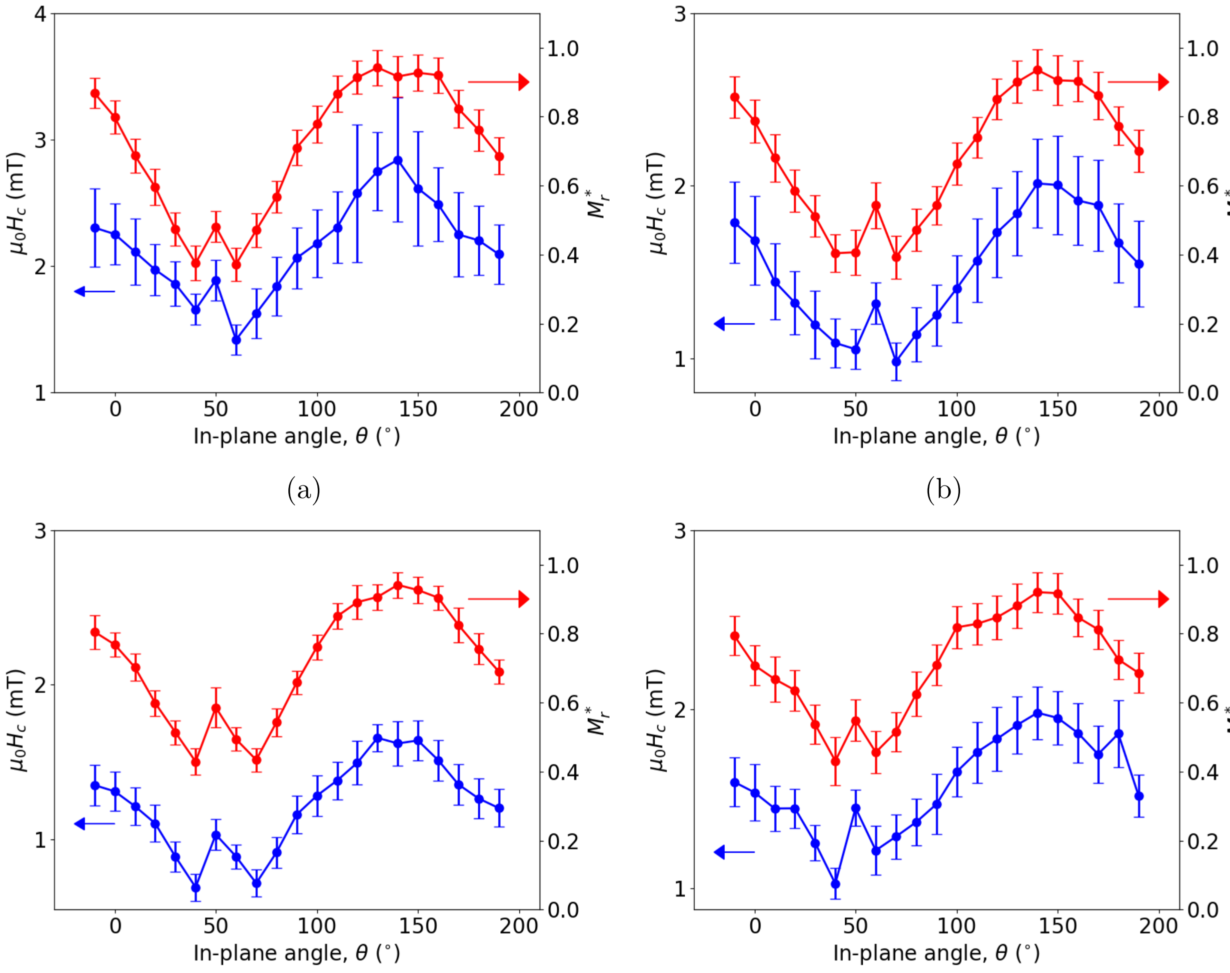

(a)

(b)

(c)

(d)

Figure 4.13: Uniaxial anisotropy of Ni/U thin films observed in both the coercive field and remanent magnetisation with in-plane angle. Easy and hard axis behaviour becomes harder to differentiate with the addition of uranium a) Nickel only. b) d_U = 0.6 nm c) d_U =4.6 nm and d) d_U =7.5 nm.

The coercive field and normalised remanent magnetisation as a function of angle can be found in fig.4.13. The form of both are very similar to those seen in fig.4.6. For both nickel and iron, the easy and hard axes are around 150° and 70° respectively, with an additional peak at 60°. It is clear that the origin of anisotropy in both cases must related be the growth conditions. If these samples were exhibiting anisotropy predominately due to texture, it would be expected that the position of these axes would be different for iron and nickel, as the easy axis would be along a different crystallographic axis for the two metals. However, when looking at the values for both $\mu_0 H_c^{\mathrm{Ave}}$ and $\mu_0 H_c^{\mathrm{Range}}$, for the nickel-based samples they are about half that of the iron-based layers. This is due to the fact that nickel is magnetically softer than iron and therefore easier to switch.

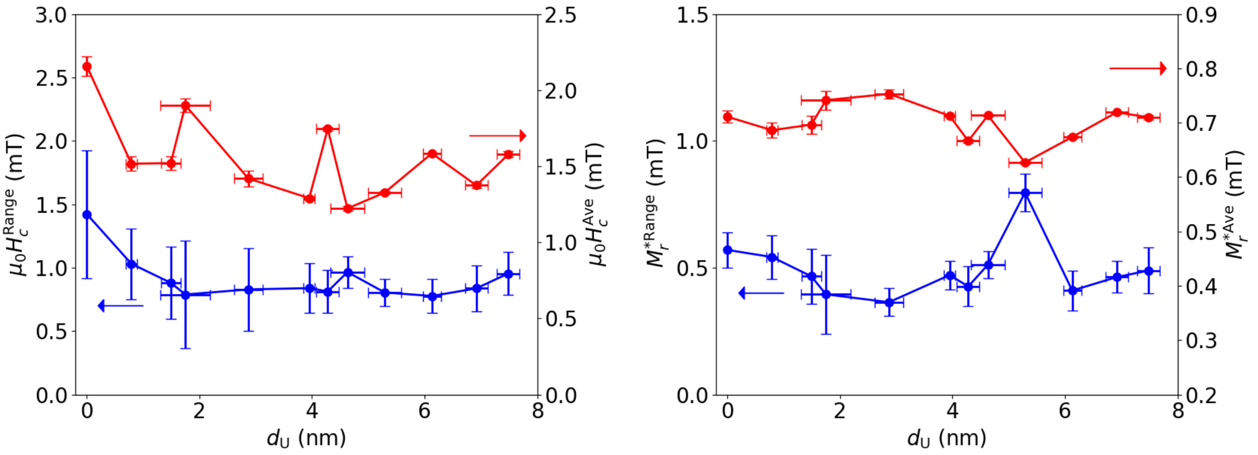

(a)

(b)

Figure 4.14: Range and average of a) coercive field b) normalised remanent magnetisation. In both cases, the average more clearly illustrates oscillations of anisotropy.

As with the iron, the range and average coercive field and remanent magnetisation were taken as a preliminary measure of the anisotropy. These can be found in fig.4.14a. When looking at the coercive field as a function of uranium thickness, it is appears that there is little variation in the range. On the other hand, there is a clear oscillation in the average coercive field. Similarly, for the remanent magnetisation, it is difficult to establish the presence of oscillations. It is therefore important to look at K_{eff} for the nickel series. The effective anisotropy constant for Ni-based layers is shown in fig.4.15. In this case, only the volume of nickel is considered when converting from magnetic moment to magnetisation as there should be no induced moment present in the system. K_{eff} has pronounced oscillations as a function of uranium thickness, though does not line up exactly with those observed in the average coercive field and remanent magnetisation. This is likely due to the small changes in both with uranium thickness, therefore masking the form present in $K_{\mathrm{eff}}(d_{\mathrm{U}}\ )$. Returning again to the material physics, these oscillation do not appear to line up with variation in rms interfacial roughness, fig.3.12a , or nickel thickness, fig.3.12b. As with Fe, Ni may also form a magnetic compound with uranium, in this case UNi_2. However, again this has a Curie well below room temperature (∼21 K), so will play no role in these magnetometry studies. This would suggest that quantum well states play a role in the nickel series, though this may seem counter-intuitive. As no induced moment is expected in a Ni/U bilayers [14], it would follow that this is due to a lack of hybridisation of Ni and U orbitals. However, for anisotropy modulation to be possible though QWSs in the non-magnetic overlayer, there must be some level of hybridisation. This hybridisation would likely be very weak in comparison to the iron, which may go some way to explaining the reduction in amplitude of the oscillations across the two samples sets. It has been previously suggested that the mixing of Fe $3d$ and U $5f$ states is much larger than that of the Ni $3d$ – U $5f$ [106][3], as thought to be the case here.

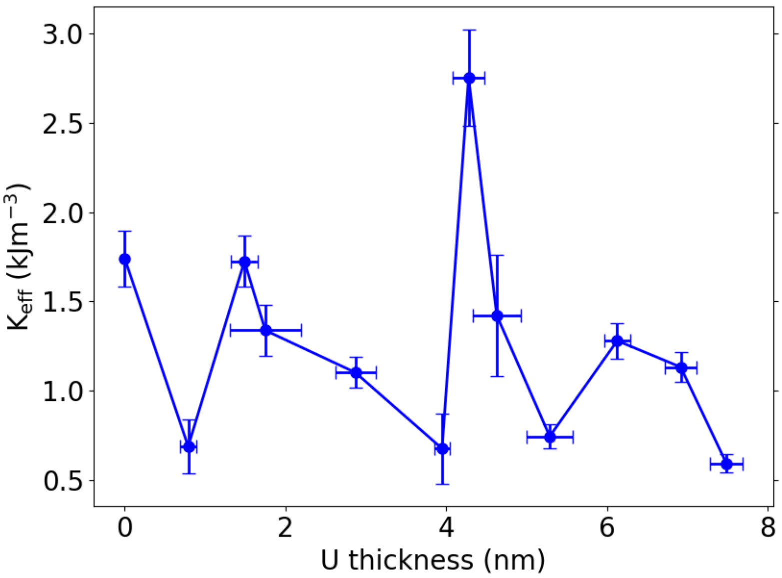

Figure 4.15: Effective anisotropy constant of nickel/uranium thin films, as a function of uranium thickness. Clear oscillations in the anisotropy can be seen.

For quantum well states, the period is determined by the band structure of the layer which changes with thickness [66]. As the layer which changes in this work is always the uranium, it would be expected that the period in both cases would be equal. In this nickel-based films, the oscillation period is around 2 nm, which is slightly shorter than that observed in the iron series. It is possible that the strong hybridisation of orbital which results in the induced moment in the iron system alters the U band structure, resulting in a different periodicity for systems with and without induced magnetic moment.

---

[3] These statements about hybridisation were made in relation to UFe_2 and UNi_2, but are expected to hold in the case of layered thin films [14].

Additionally, the presence of QWS induced oscillation in nickel, contributes to the understanding of the oscillatory induced moment observed in iron. As the nickel exhibits no PIM, it is not a prerequisite for QWSs. Therefore the oscillation of the induced moment is a consequence of QWSs, as opposed to the driving force behind them.

No perpendicular magnetic anisotropy was exhibited by the nickel-based heterostructures. The thickness of the nickel layers is greater than the iron thickness. This may indicate that while the iron is demonstrates PMA at thickness greater than normal, there could be an upper limit which the nickel exceeds. Unfortunately, this could only be tested by growing a thinner nickel series.

4.4 Conclusion

The anisotropy of Fe/U and Ni/U bilayers was studied extensively using vibrating sample magnetometry. For both samples sets it there is a clear uniaxial anisotropy which originates from the oblique angle of incidence during sputtering. This anisotropy was expressed both qualitatively - range and average coercive field and remanent magnetisation - and quantitatively as an effective anisotropy constant. With increasing uranium thickness K_{eff} was found to oscillate in both the iron and nickel sample series. These oscillations were ascribed to quantum well states forming in the uranium layer. Oscillations in the Fe series are stronger than its Ni counterpart due to stronger hybridisation of the Fe $3d$ and U $5f$ states. Furthermore, it is probable that these QWSs drive the oscillation of the proximity induced moment studied in ref [13]. There is also a slight variation in the period of the the oscillations between Fe/U and Ni/U samples. This is again most likely caused by the stronger hybridisation of iron and uranium altering the band structure.

Hopefully, through theoretical calculations the presence of quantum well states can be corroborated. The x-ray diffraction studies in chapter 3 showed that iron/uranium bilayers tend be formed of a mixture of the [011] and [001] directions, with the [001] orientation being preferred, while uranium grown on nickel is predominantly [001] oriented. This data may allow calculations to provide an accurate estimation of the expected periods. However, preliminary calculations based on possible single crystal orientations point to aliasing due to the large step size in uranium thickness between successive samples. It may be possible to create a finer series of films by reducing the power at which the uranium was sputtered. This would afford control over the film growth, allowing access to sub-angstrom deposition rates for uranium.

In addition to the in-plane studies, magnetisation was studied with the applied field at 90°

to the film surface. While only hard axis behaviour was observed for nickel, iron exhibited unexpected behaviour as a small subset of samples exhibit perpendicular magnetic anisotropy. This is particularly unexpected due to the relatively thick iron layers grown for this work. From these studies, the origin of this PMA is not apparent, though it may be due to a surface anisotropy or the interfacial Dzyaloshinskii-Moriya interaction. In order to understand the underlying physics behind the spontaneous perpendicular magnetisation in iron-based samples, a second series of iron samples should be fabricated. These samples could then be investigated using Brillouin light scattering, a technique used to determine the strength of the Dzyaloshinskii-Moriya interaction. This would confirm the existence of chiral spin textures due to interfacial DMI within the system. If no DMI was observed, this would signify the presence of a surface anisotropy contribution which is U thickness dependent.

Chapter 5

Anisotropic Magnetoresistance

5.1 Theory

Anisotropic magnetoresistance (AMR) is a magneto-transport technique in which the measured change in resistance as a function of externally applied field is dependent on the orientation of the sample magnetisation with respect to the direction of the current through the sample [127]. AMR is related to the spin-orbit coupling of a material, as this promotes mixing between spin-up and spin-down states in the d band of a ferromagnet. This mixing alters with direction of the magnetisation, and therefore altering the occupation of the d bands. This results in anisotropic scattering of the s electrons into the d band [128–130] and is often quantified as the change in resistivity between the applied field parallel to current $\rho_{\|}$ and perpendicular to current $\rho_{\perp}$,

$$\Delta\rho = \rho_{\|} - \rho_{\perp}. \tag{5.1}$$

The change in resistivity at any given angle θ between the magnetisation and the direction of current can be determined from

$$\rho(\theta) = \rho_{\perp} + \Delta\rho\cos^2(\theta). \tag{5.2}$$

It is common to discuss materials in terms of their anisotropic magnetoresistivity ratio, originally as a metric of suitability for storage applications [127], which is given as

$$\frac{\Delta\rho}{\rho_{\mathrm{av}}} = \frac{\rho_{\|} - \rho_{\perp}}{\frac{1}{3}\rho_{\|} + \frac{2}{3}\rho_{\perp}}. \tag{5.3}$$

This equation is primarily for bulk samples as ρ_{av} is composed of two directions perpendicular to the current path and only one parallel.

In this work as the resistivity ratio is referred to as the normalised change in peak resistivity between the parallel and perpendicular directions, and is denoted $\Delta R/R_{\text{range}}$ [1].

The resistivity of uranium, iron, nickel and niobium are $\sim$0.27 $\mu\Omega$m [131], 0.10 $\mu\Omega$m, 0.07 $\mu\Omega$m, and 0.14 $\mu\Omega$m respectively. It is expected that the current will preferentially try to flow through the layer with the lowest resistivity.

Zhang *et al.* suggest that in when there is additional spin-orbit interactions at a ferromagnet/non-magnetic interface, the measured AMR will exhibit an unconventional angular response [132], given by

$$\rho(d) = \rho_0 + m_x^2 \Delta\rho - m_y^2 \Delta\rho, \tag{5.4}$$

where d is the distance from the interface, and m_x and m_y are the x and y components of the magnetisation respectively. Here the first two terms of the right hand side are equivalent to eqn.5.2. The third term is related purely to spin-orbit scattering and does not have the same angular dependence as the previous term. This term becomes most apparent when the magnetisation is orthogonal to both the electric field and the effective spin orbit field, i.e. out-of-plane. As this work focuses on the in-plane configuration it may be that no pure spin-orbit contribution will be seen. Zhang *et al.* also state that the second term, while traditionally related only to the bulk AMR may also be dependent on the spin-orbit coupling of the heavy metal layer. While it is unlikely that there will be any additional contribution from the third term in this work it should be noted that this theory does not account for reflections of electrons at the interface, and therefore ignores quantum well states. As these QWSs are expected based on the work in chapter 6.13, it may be that this theory would not be viable for this system in any case. However, this does not suggest that there is no additional contribution from the large SOC, rather that is unclear as to how this effect may be quantified, particularly in the presence of QWSs.

Within the literature, there is little work on the effect of other types scattering in comparison to the traditional $s-d$ scattering within a ferromagnet expected for AMR. Therefore it is unclear what effect the f electrons of uranium may have on the anisotropic magnetoresistance measurements.

When field is swept in both directions, the AMR signal is observed as a butterfly hysteresis

---

[1] In the literature, this is commonly referred to purely as $\Delta R/R$. However, in this work is has been chose as $\Delta R/R_{\text{range}}$ to maintain consistency with the VSM analysis. Here $\Delta R/R$ refers to the normalised change in resistance of the samples at any given angle.

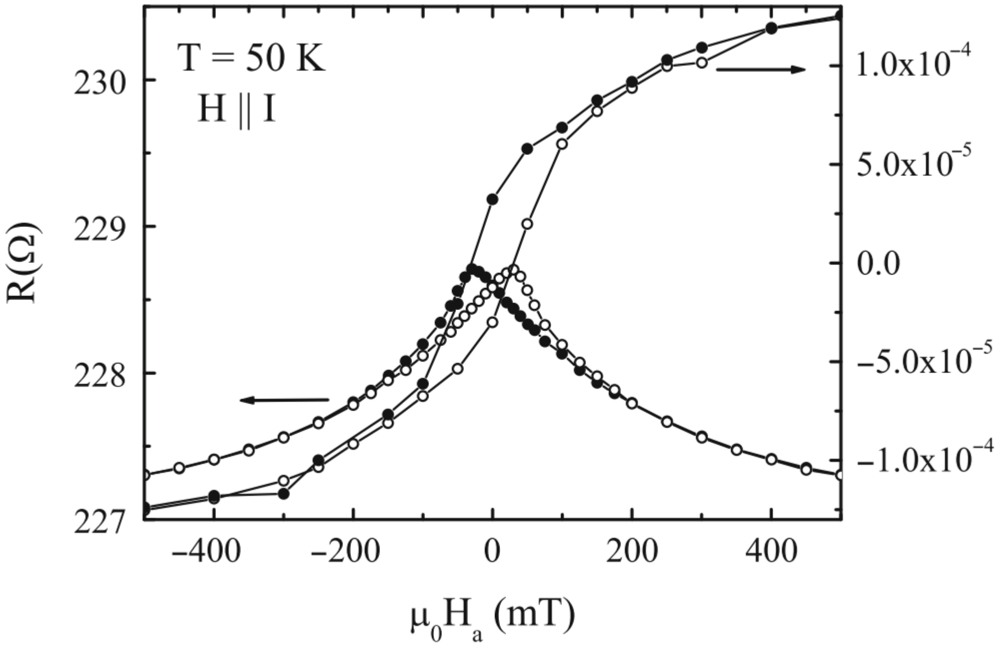

Figure 5.1: Example of AMR peak position in comparison to the coercive field measured using vibrating sample magnetometry for a $Pd_{0.81}Ni_{0.19}$ thin film. Taken from ref. [133]

loop with two peaks in resistance. It is expected that the positions of these two AMR peaks correspond to the coercive fields determined from the VSM in chapter 6.13. [133]. This can be seen in fig.5.1 for a $Pd_{0.81}Ni_{0.19}$ thin film. In both field directions the VSM data clearly aligns with the peaks observed from AMR measurements.

5.2 Device Fabrication

For magnetoresistance measurements, samples were patterned to provide a defined current path. In this case, a Hall bar configuration, with two current contacts and six voltage taps, was used. Processing of the samples was carried out in the cleanroom at the University of Bristol.

Samples were cleaned using acetone and isopropyl alcohol. Samples were then placed in a spin coater and were spun initially with a Microposit primer in order to help the resist adhere to the sample surface. For the iron-based samples, where the niobium cap was <10 nm, Microposit S1805 resist was used. To coat the samples, a drop of resist was placed on the surface of the sample which would then be spun for 45 s at 4000 rpm, with an acceleration of 2000 rpm s^{-1}. The samples were baked on a hot plate at 115° for 1 minute to solidify the resist layer.

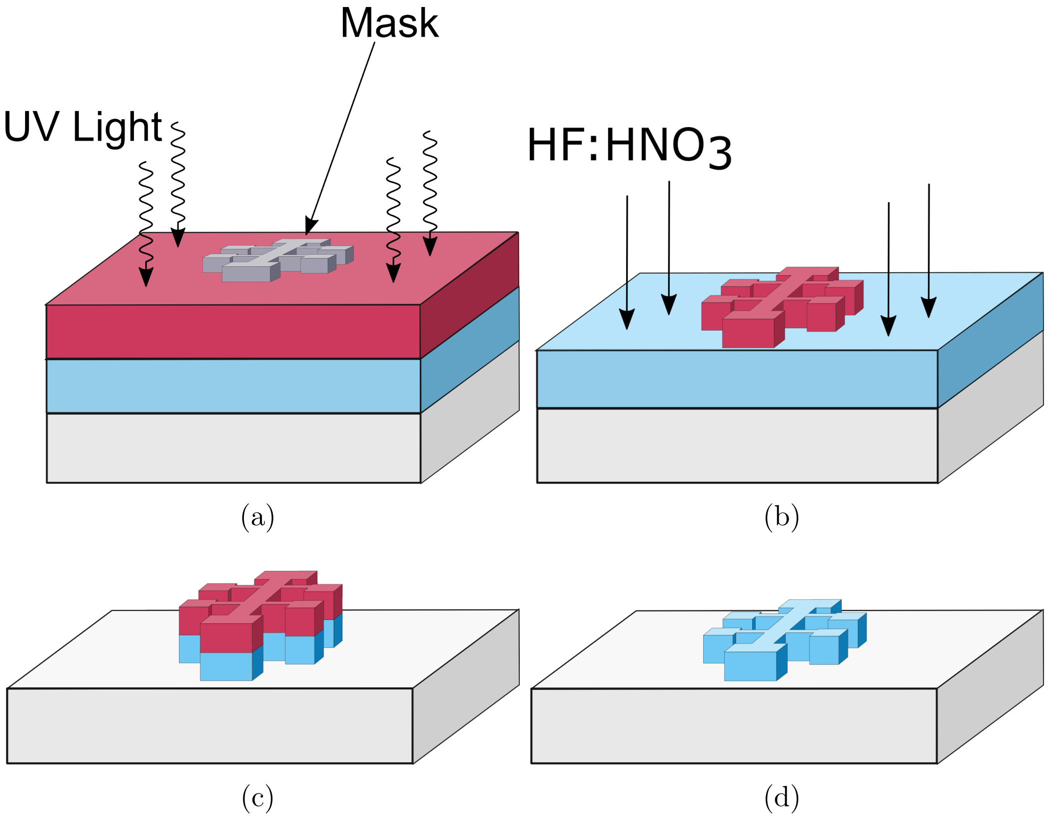

Figure 5.2: Process of wet etching bilayer samples. (a) Chrome mask is placed on top of resist (red layer) coated samples. Resist is then exposed with UV light. (b) After exposure, sample is developed, leaving only resist in the desired pattern. The sample is then dipped in acid to etch. (c) After the acid etching, only the resist covered material remains in tact. (d) Resist is removed, leaving the final patterned sample.

The resist was then shaped into the desired device pattern using optical lithography and a chrome on glass mask. The lithography was carried out in two steps: removal of the thick edge bead, and patterning of the Hall bar. When using the S1805 resist optical lithography was done using a Karl Suss MJB3 mask aligner. A square mask was used to remove the resist edge bead. The edge bead was exposed for 180 s and developed in Microposit MF319 developer for 60 s. Removal of this edge bead created a flat surface on which the device mask could sit flush on. This stops the accidental exposure of sections of the Hall bar. With the edge bead removed, the film was positioned under a Hall bar mask and exposed for 120 s. The resist was again developed for 60 s. The mask used had a device size of 3 mm × 2 mm with the central wire being 100 μm wide, the contact pads 400 μm^2, and voltage taps 40 μm wide. The multilayers were etched in a 1:1 HNO_3/HF solution, with 2 ml of acid diluted in 98 ml of water. Depending

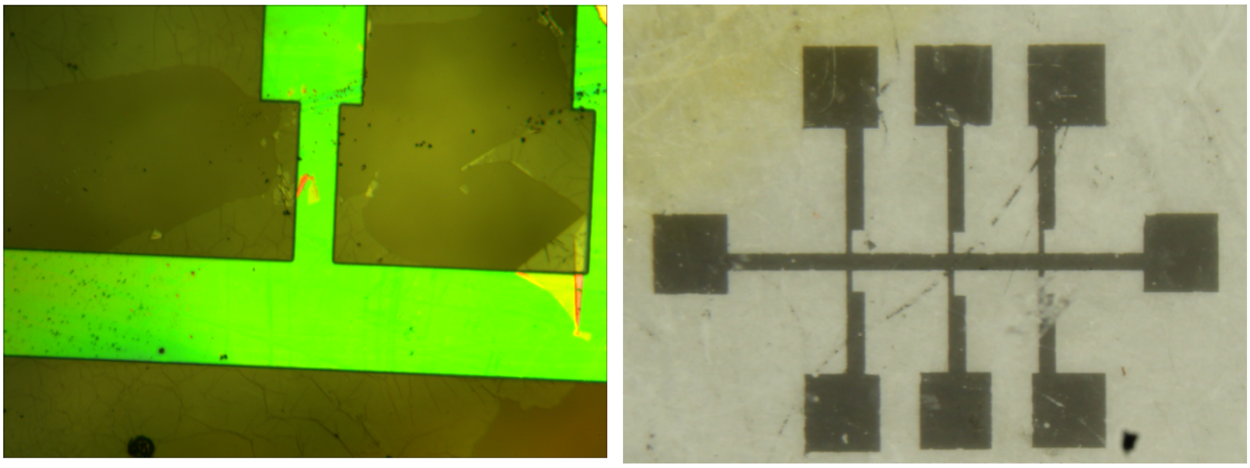

(a) (b)

Figure 5.3: Iron/uranium samples etched into a Hall bar configuration. a) samples post etch with resist covering bar. The dark edges around the device are due to an undercut which occurred during the acid etching. b) Final etched Hall bar.

on the number of samples previously etched in the solution, the etching time varied from 10 s – 90 s.

For Ni based structures, the Nb cap was significantly thicker (>10 nm). For these thicker films, the S1805 resist would not fully adhere to the Nb film and was replaced with the thicker S1813 resist. Samples were spun at 3000 rpm for 45 s, with an acceleration of 150 rpm s^{-1}. The slower speed and acceleration were chosen to avoid spinning the resist off the surface of the film. The lack of adhesion of the S1805 to the thicker Nb was attributed to the surface roughness. The lithography with thicker resist was carried out on a MIDAS MDA-400M-6 mask aligner. Edge beads were exposed for 25 s and developed for 60 s, and Hall bars were exposed for 5 s and developed for 45 s. Due to the thicker Nb layer, a stronger concentration of acid was required. In this case, 10 ml of acid in 50 ml of water was used. Samples were immersed in the solution for 30 s.

This process produced samples with only very small undercuts, on the order of $\approx 2\,\mu$m, for both types of samples. These can be seen in fig.5.3a as the dark edge around the device. An example of the final device can be seen in fig.5.3b.

5.3 Set-up

Patterned samples were secured on to an 8-pin DIP socket adapter chip using GE varnish. The samples contacts were then bonded to the chip contacts by either aluminium or gold wires. Iron based samples were contacted using 33 μm Al wire by wedge bonding on a TPT HB16 wire bonder. An example of this can be found in fig.5.4a. For the nickel samples, it was found that the Al wire would not bond well and that the wedge bonding process would remove small sections of the film. To over come this, Ni samples were hand bonded using an indium stamping method to secure 25 μm gold wires.

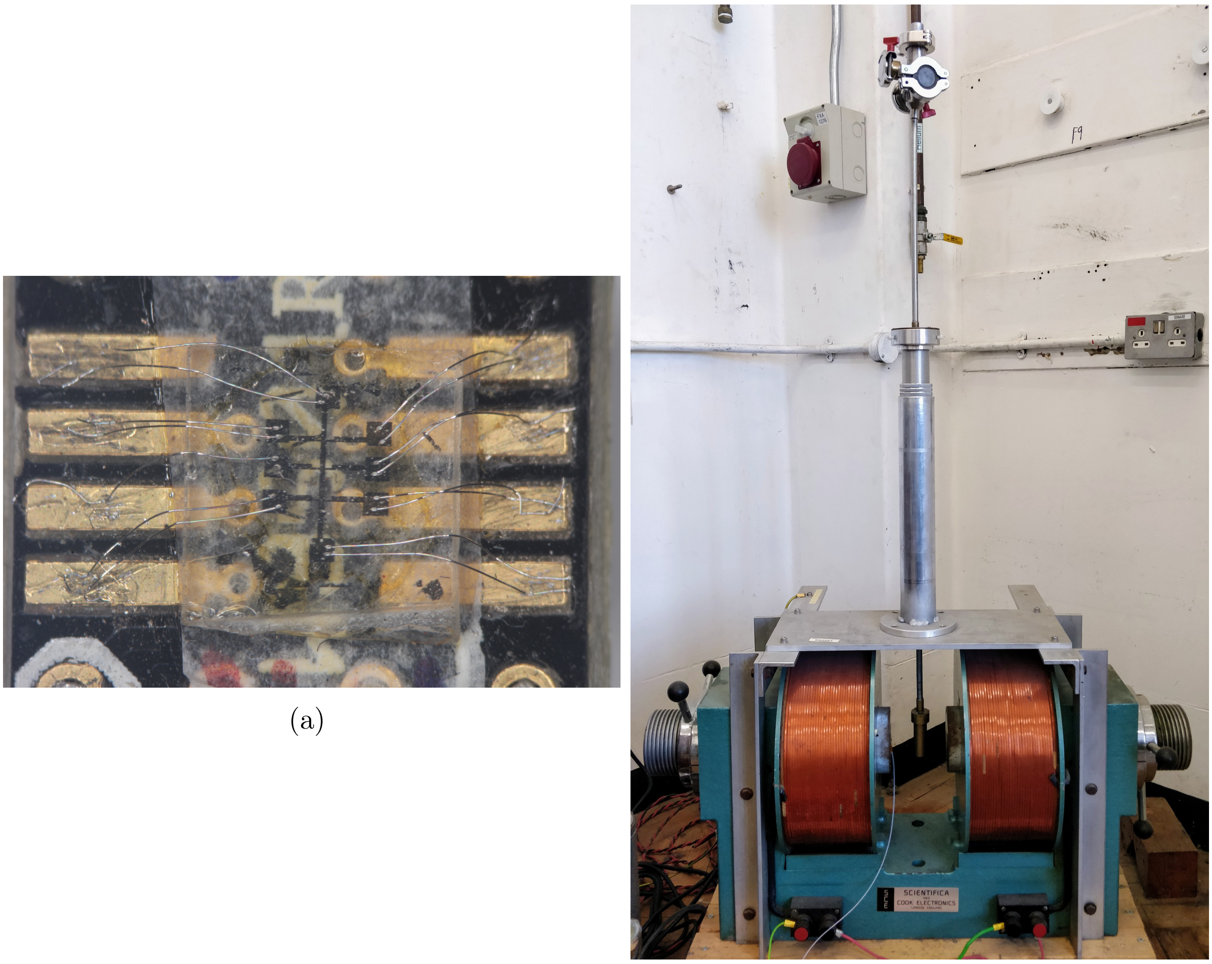

(a)

(b)

Figure 5.4: a) Sample bonded to 8-pin DIP chip by Al wedge bonding. Given the precision of the wire bonder each contact can be bonded at least twice. This creates redundancy and allows for breakage. b) AMR measurement set-up. Samples is covered by brass cap to reduce noise. Probe can be freely rotated between the poles of the magnet.

Bonded samples were attached to DIP socket on the AMR probe and placed between the poles of an electromagnet, as shown in fig.5.4b. The current to the coil was controlled by a Kepco bipolar operational power supply, which operates to a maximum of $\pm 6\,\mathrm{A}$ corresponding to an $\sim \pm 200\,\mathrm{mT}$ field. A bipolar current of $100\,\mu\mathrm{A}$ was produced by a Keithley 6221 current source and was passed along the main current wire, with voltage measured longitudinally using either a Keithley 2182A nanovolmeter or an Agilent 34420A nanovoltmeter. As with the VSM, samples were rotated in-plane from -10° – 190° in 10° ± 1° increments.

5.4 Results

5.4.1 Fe-Based

A standard AMR measurement where current is parallel or perpendicular to the magnetisation results in a basic butterfly hysteresis loop, as illustrated in fig.5.5a. The important features of these loops are the peak positions $\mu_0 H_c$ and the change in resistance ΔR. ΔR was always taken as the distance between the peak and the saturation value. However, when the external field is applied around 45° to the current, the hysteresis loop becomes more complex, as exhibited in fig.5.5b. This unusual loop shape occurs at the intermediate stages between positive ΔR to negative ΔR and vice vera, and appears to be a superposition of both behaviours. In these cases, there is an increase (decrease) in resistance followed by a decrease (increase) to what is considered the "main peak". This results in the appearance of extra peaks surrounding the main peak. For analysis in this work, where these complex loops occur ΔR does not take into account changes in resistance in the opposite direction from the main peak, but only from the saturation baseline to the peak. This is illustrated in fig.5.5b. These extra peaks also tend to occur at higher fields than the main peaks. These additional peaks are present in all samples, including $d_{\mathrm{U}} = 0\,\mathrm{nm}$. They can also be seen in ref. [133], suggesting that they are typical of AMR and are not related to the properties of the uranium over-layer.

During field sweeps, there can be heating within the sample. This heating is linear in time and leads to a linear offset between the up and down field sweeps, as illustrated in fig.5.6a. This offset was removed by fitting the saturation resistance with a straight line and subtracting the gradient, resulting in loops similar to the one shown in fig.5.6b.

Based on ref. [133], the AMR loops were compared to their corresponding VSM hysteresis loops. This is illustrated for the iron only sample at a variety of angles in fig.5.7. From these data overlays, it seems that the relationship between peak position and coercive field is more

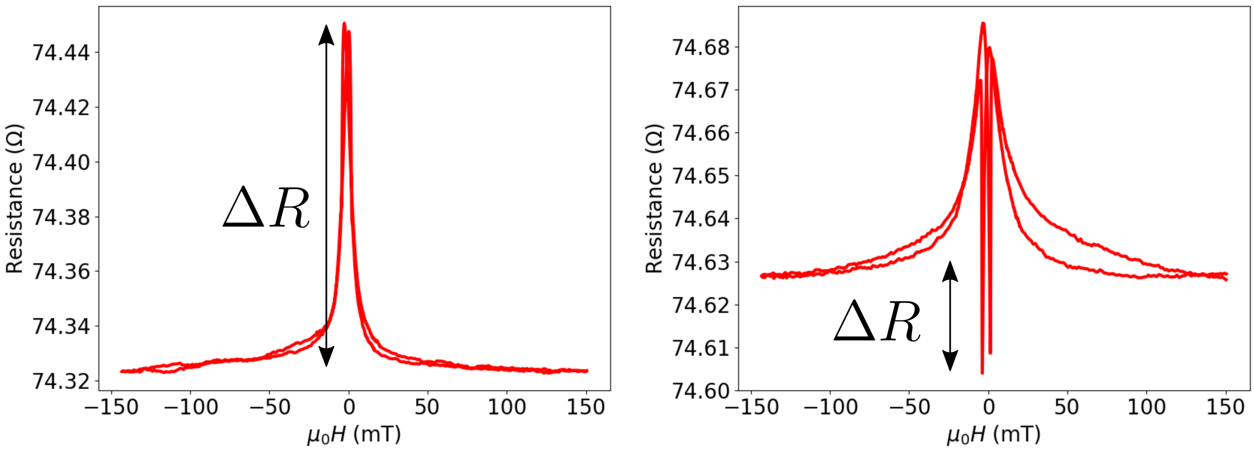

(a) (b)

Figure 5.5: Anisotropic mangetoresistance curves at different angles between current direction and the applied field. ΔR is defined as the distance between the saturation and peak resistances. a) Typical butterfly hysteresis loop when field is applied at 10° to the current direction. b) AMR curve at 140° between applied field and current direction. Here the curve is at a midpoint between a positive and negative change in magnetoresistance.

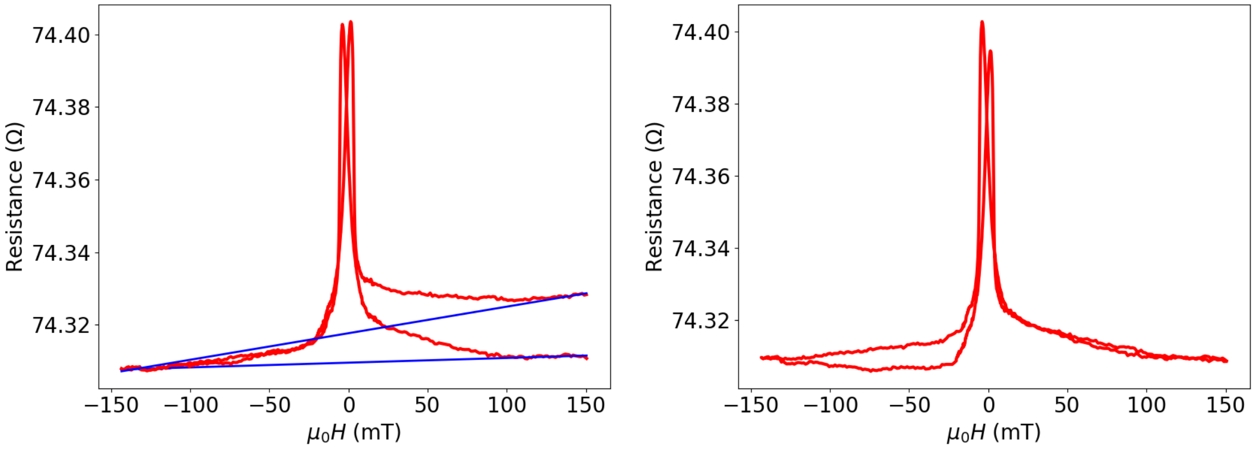

(a) (b)

Figure 5.6: Examples of heating within the samples causing an offset in the resistance. a) Hysteresis loop with linear fit (blue) to the saturation resistance. This gradient can be subtracted to remove effects of heating. b) The hysteresis loop after a linear offset has been removed.

complex than expected. At each angle, one peak is displaced in field compared with its VSM counterpart. This shift is smallest when the magnetisation lies along the easy axis, illustrated in fig.5.7d. This may result from an additional shape anisotropy term due to the patterning

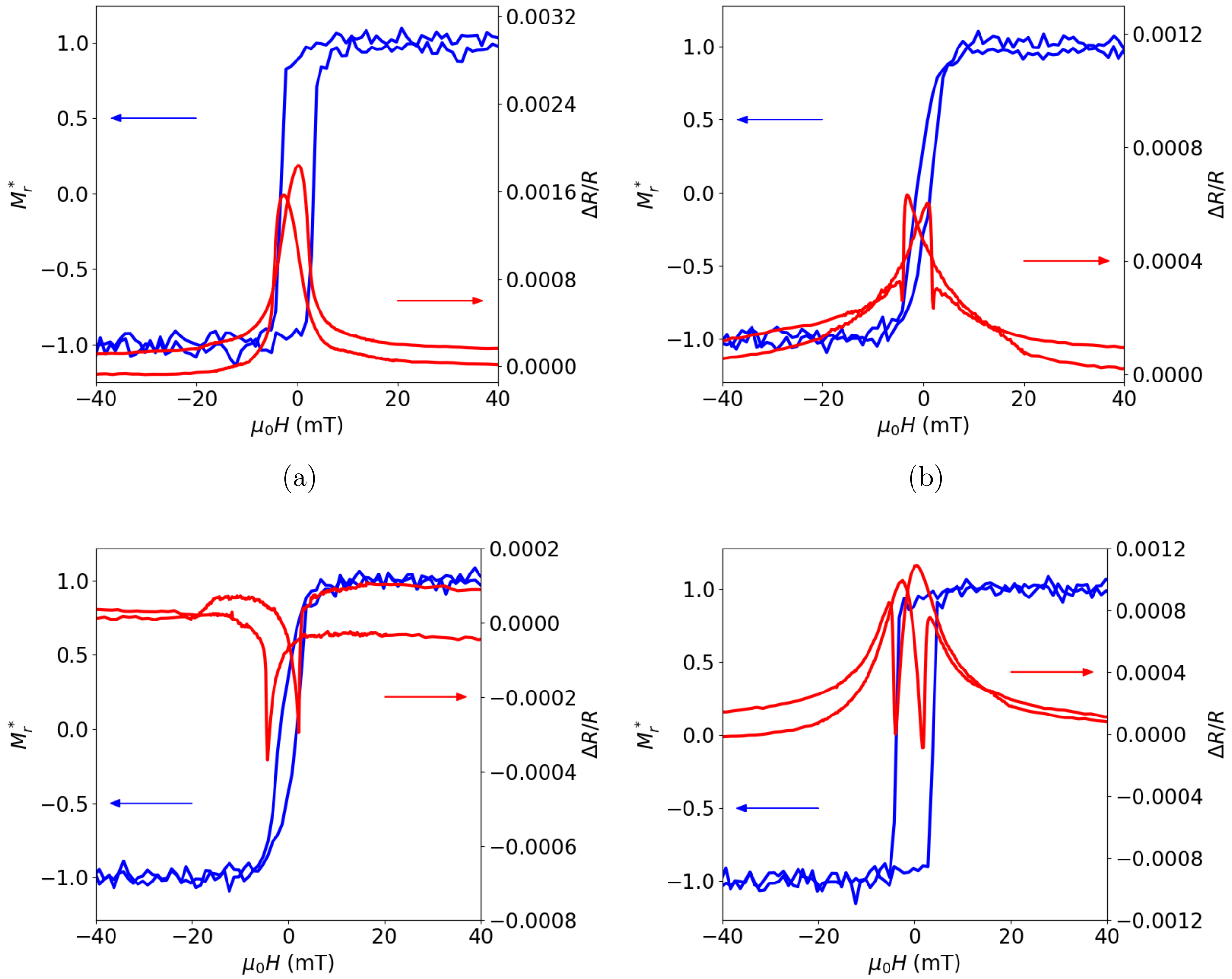

(a)

(b)

(c)

(d)

Figure 5.7: AMR data (red) overlaid on VSM hysteresis loops (blue) at multiple angles. In each case only one peak from the AMR butterfly loop matches the VSM coercive field. a) 0° b) 60° c) 90° d) 150°

of the films. It is also interesting to note that the easy axis observed in the VSM data does not correspond with simple AMR behaviour. Both the magnetic easy and hard axes lie along the positive-negative magnetoresistance switching angles. This is likely just an unfortunate consequence of the design and patterning of the device in an effort to keep measurements consistent. There is no evidence that it has any effect on the anisotropic magnetoresistance, though in future it may be interesting to create a device in which the current direction would be parallel to the magnetic easy axis for comparison. Ideally the saturation resistance could be plotted at each angle and fitted with eqn.5.2 to account for this. From the data taken in this work, it appears that the saturation resistance does not follow eqn.5.2 due to heating the sample and possible other contributions, such as the planar Hall effect, resulting in a much more complex functional form. Throughout the rest of the chapter, the focus is placed on the change in the normalised change in resistance of the peaks, as this removes these additional effects which disrupt R_{sat}.

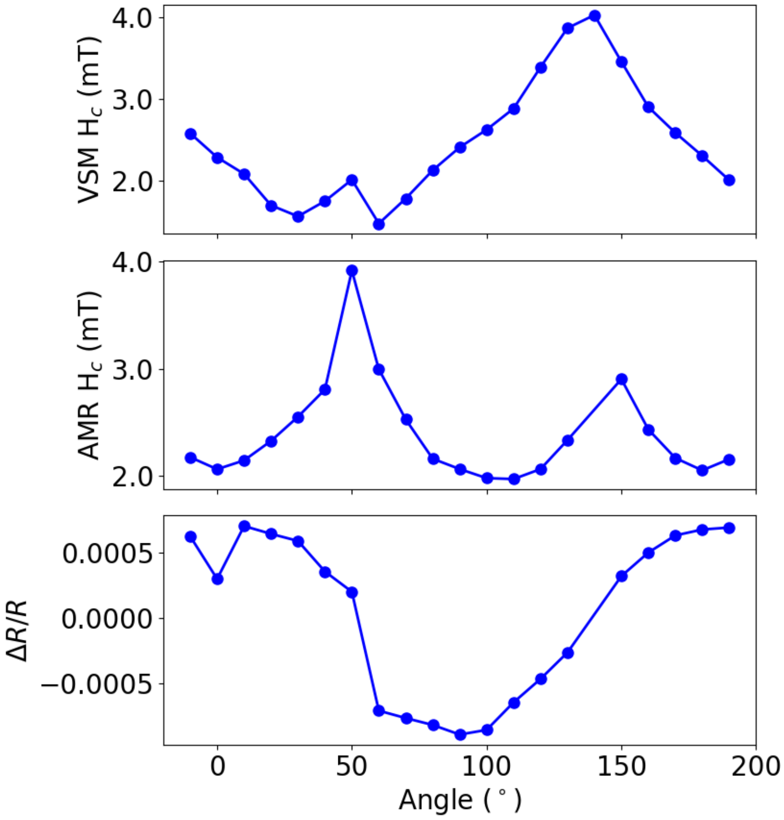

Figure 5.8: Comparison of VSM and AMR angular data for d_{U} =6.5 nm. The top and middle panels represent the coercive fields from vibrating sample mangnetomomety and anisotropic magnetoresistance respectively. The bottom panel shows $\Delta R/R$ from the AMR measurements.

It is useful to compare $\mu_0 H_c$ from both the VSM and AMR measurements as well as the normalised change in resistance $\Delta R/R$ as a function of angle. Fig.5.8 illustrates this for sample 1223 ($d_{\mathrm{U}} = 6.5\,\mathrm{nm}$). The coercive field comparisons indicate similarities in both the form and peak positions. However, the peak at 50° is markedly increased in comparison to its VSM counterpart. In the AMR data, $\mathrm{H}_c^{\mathrm{AMR}}$ increases much more suddenly around a peak, where as $\mathrm{H}_c^{\mathrm{VSM}}$ increases steadily across the whole angular range.

When comparing the peak position with $\Delta R/R$ in fig.5.8, it appears that the peaks shift to higher fields as $\Delta R/R$ switches from positive to negative. As stated earlier this appears to be dependent on the design of the device as the easy and hard axis align with the field at angles where the current and magnetisation are not orthogonal with one another.

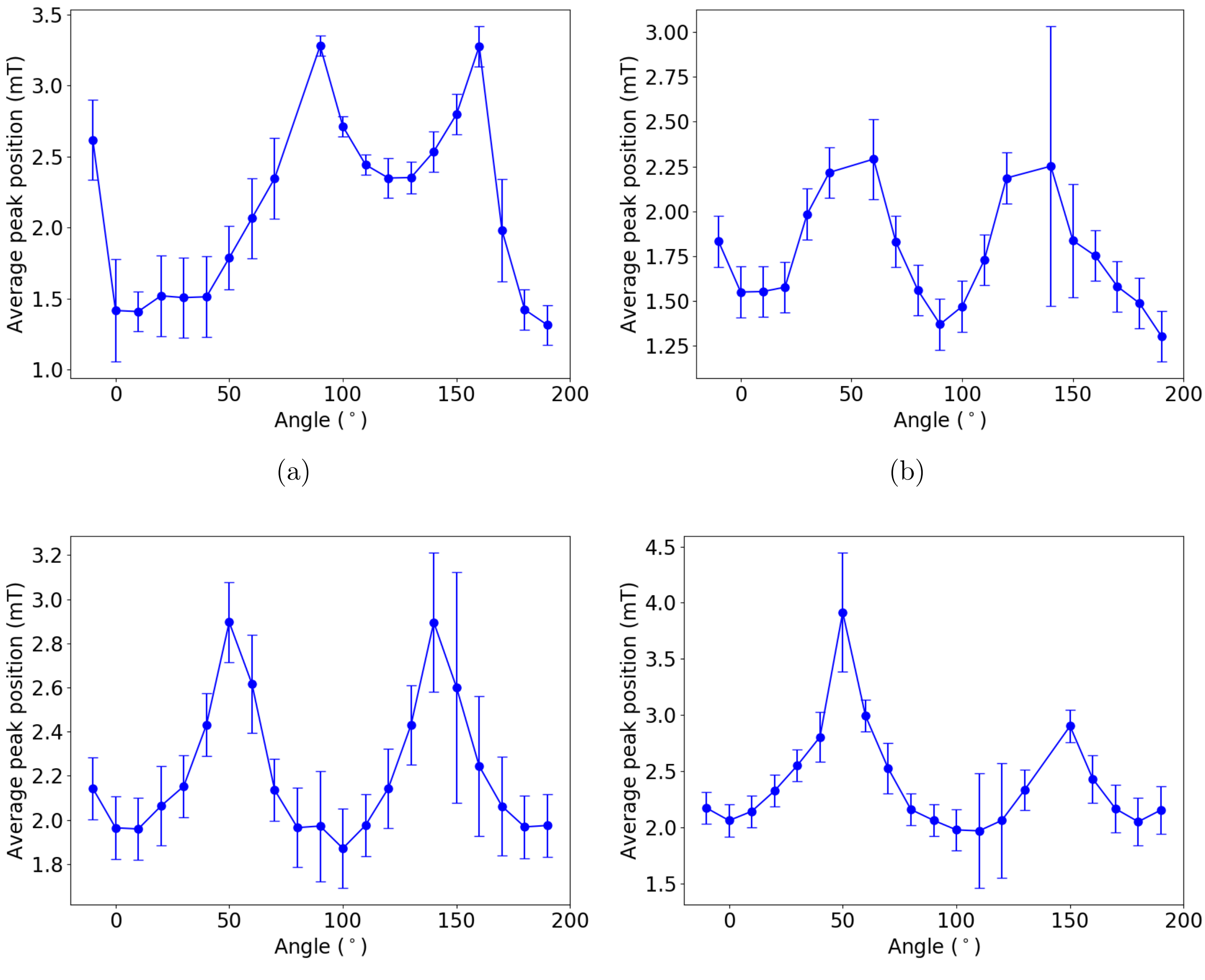

(a) (b)

(c) (d)

Figure 5.9: Average position of the hysteresis loop peaks at varying uranium thicknesses. In each case there are two clear peaks that are positioned at ∼ 50° and 150°. a) d_{U} = 0 nm b) d_{U} = 1.7 nm c) d_{U} = 3.2 nm d) d_{U} = 6.5 nm.

Focusing on peak position as a function of angle, the functional form when compared to the corresponding coercive field data from the VSM is very similar. In both cases there are two clear peaks which tend to be centred around 50° and 150° for all samples in the iron/uranium series. However, the presence of a second peak around 50° is much more pronounced in AMR data. In all AMR data, the average $\mu_0 H_c$ is lower than the coercive field determined by the

VSM. This is to be expected as it is clear from fig.5.7 that the peaks do not line up exactly with the coercive field. For the iron only sample in fig.5.9a, the first peak is shifted to higher angles, ∼ 90°. It is not obvious why this may have occurred as the corresponding VSM data shows a large second peak around 60°.

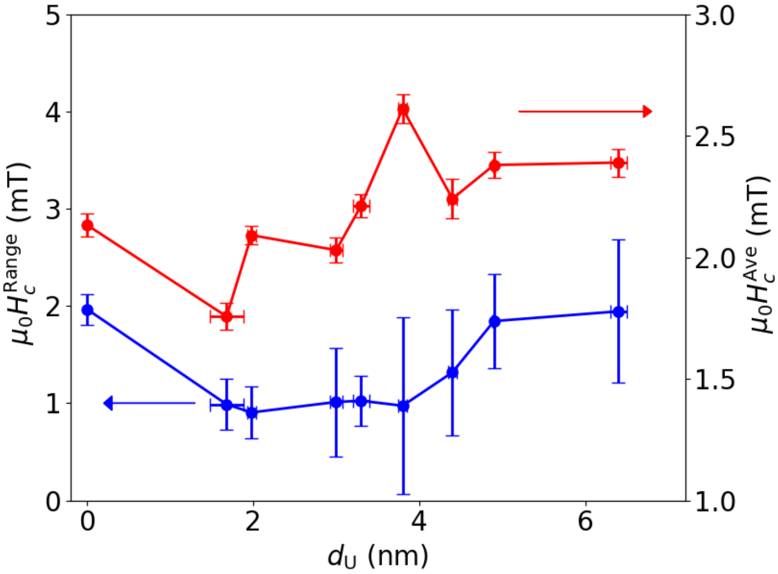

Figure 5.10: Range (blue circles) and average (red squares) of peak positions across the Fe bilayer series. The range does not exhibit much change with d_{U} but the average suggests oscillations of the anisotropy.

As the with VSM data, the range and average of $\mu_0 H_c$ for each samples was used to quantify the anisotropy of the system, shown in fig.5.10, based on the assumption that the peak position corresponds to the coercive field. It seems like the range is consistent across d_{U} , though this may be due to the resolution of the measurement. As a result of the low resolution and large errors, there are no clear conclusions that can be drawn from the range. Conversely, the average appears to oscillate with uranium thickness. It appears that the period of this oscillation is shorter than measured through magnetometry, ∼ 2 nm compared to ∼ 3 nm, but is likely within error due to the relatively coarse step size in d_{U} . However, it should also be pointed out that in this series, samples 1216 $d_{\mathrm{U}} = 2.2$ nm and 1222 $d_{\mathrm{U}} = 5.3$ nm have been omitted due to issues with patterning or lack thereof for sample 1222. For sample 1216, when the switch from positive to negative $\Delta R/R$ occurred, there was a shift in the peak position from ∼ 2 mT to ∼ 7 mT. It is possible that this is the result of some pinning due to defects in the wire. It was determined that the first current contact was not well connected to the Hall bar and therefore the current was routed along a voltage contact. This may have introduced additional complications in to the current path, resulting the the unusual behaviour. The presence of these anomalous systems may have resulted in some aliasing and were omitted to avoid this issue, which may result in under sampling Despite the lack of a completed series, the appearance of anisotropy oscillations in $\mu_0 H_c^{\mathrm{ave}}$ corroborates the idea of quantum well states playing an important role in this system.

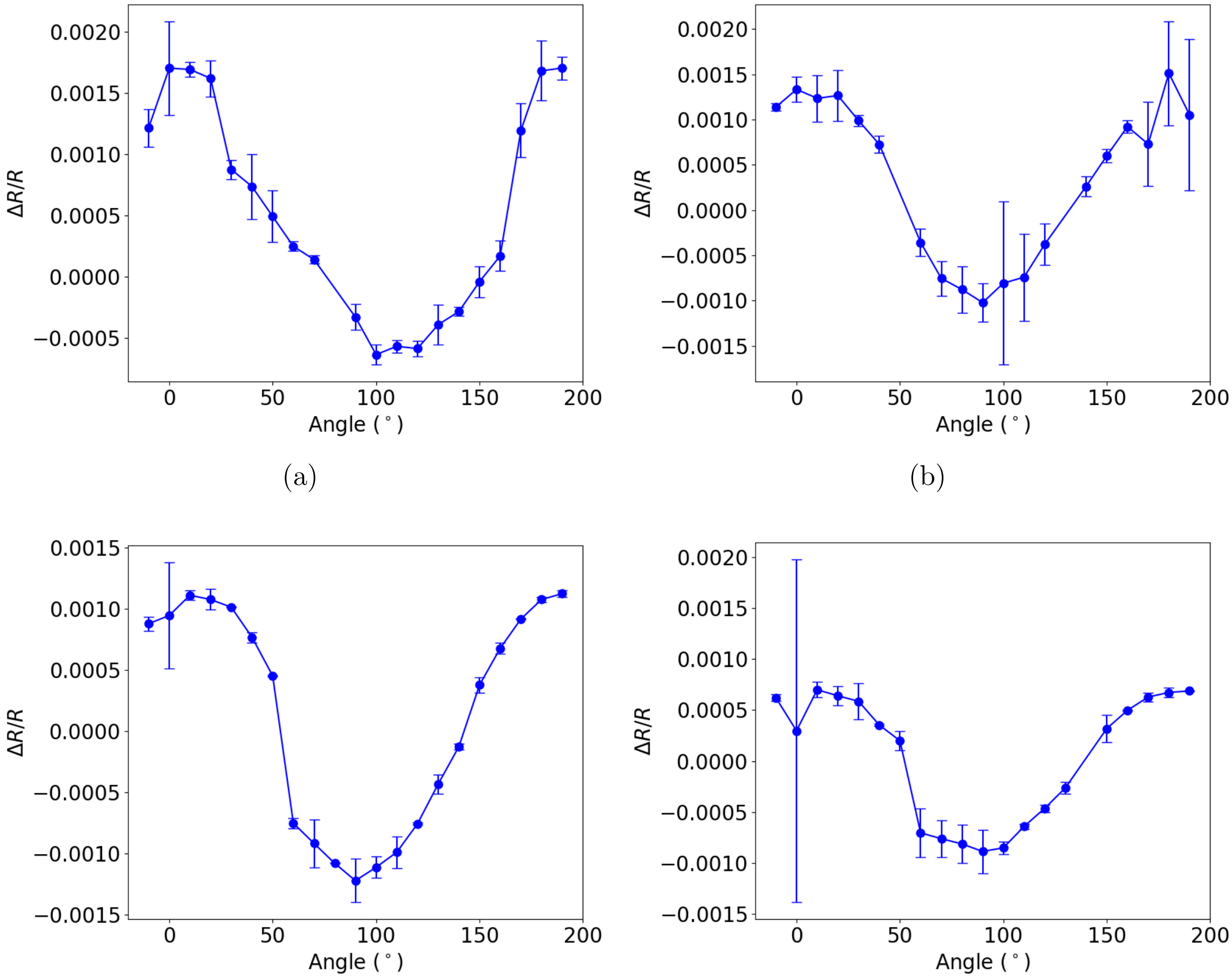

(a) (b)

(c) (d)

Figure 5.11: Average $\Delta R/R$ of the two peaks for various uranium thicknesses. All of these curves follow the expected $\cos^2$ dependence. a) $d_{\mathrm{U}} = 0\,\mathrm{nm}$ b) $d_{\mathrm{U}} = 1.7\,\mathrm{nm}$ c) $d_{\mathrm{U}} = 3.2\,\mathrm{nm}$ d) $d_{\mathrm{U}} = 6.5\,\mathrm{nm}$

Fig.5.11 illustrates the changing magnetoresistance for a subsection of the iron based samples. These appear to follow the $\cos^2\theta$ dependence as expected from eqn.5.2, though there is some offset, resulting in a slight asymmetry around $\Delta R/R = 0$. In some cases, such as fig.5.11d at 0°, the heating in the samples was not continuously linear. When a linear background was removed, an offset in the peak position was introduced. It is expected that ΔR should be approximately the same for both peaks in the field sweep as the loops should be symmetrical in field. To account for this, the error in $\Delta R/R$ for each peak is taken as the different between that peak and its counterpart.

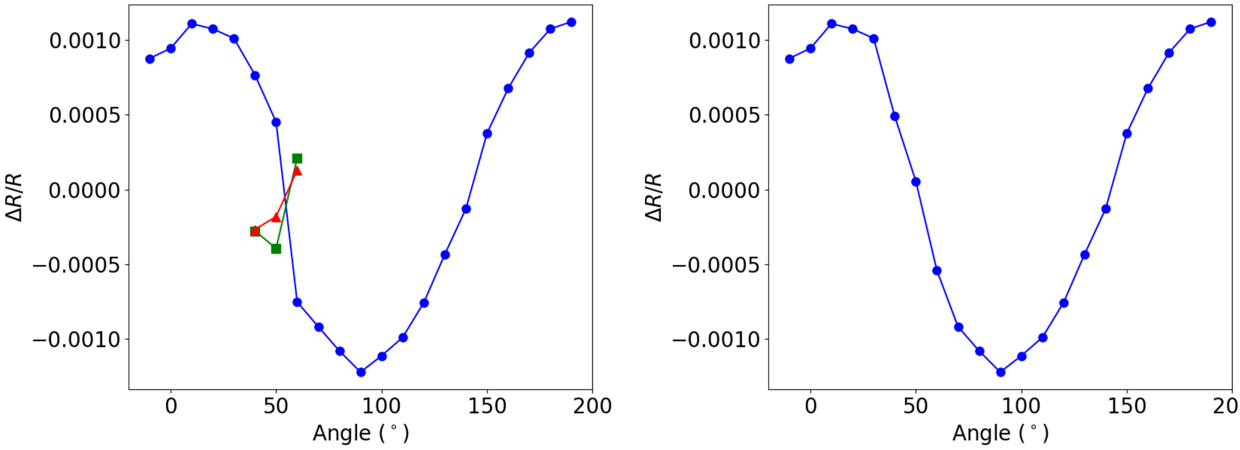

(a) (b)

Figure 5.12: Change in resistance with the inclusion of extra peaks a) Extra peaks can be observed at 40°–60°. Green squares and red triangles illustrate the change in magnetoresistance from the saturation value to the extra peak. Green squares represent the first peak encountered during the field sweep and the red triangles represent the final peak observed. b) $\Delta R/R$ of extra peaks subtracted from $\Delta R/R$ $_{\text{main}}$ to give the total $\Delta R/R$ at that angle. This appears to enhance the $\cos^2\theta$ form of $\Delta R/R$.

While the data presented in fig5.11 follow the expected $\cos^2\theta$ dependence, for some angles within these data sets, the full change in resistance in not truly taken into account. As stated previously, the change in resistance is only taken from the saturation value to the "main peak". However, it may be the case that the presence of extra peaks, such as those seen in fig.5.5b may alter the angular dependence. Fig.5.12 illustrates the effect of these extra peaks on the normalised magnetoresistance for the samples with $d_{\text{U}} = 3.2\,\text{nm}$. In fig.5.12a, the first peak encountered and the peak occurring after the main peak are represented by the green squares and red triangles respectively. As there is a switch from positive to negative magnetoresistance, these peaks are found to always oppose the main peak direction. When these extra peaks are taken into consideration for the total resistivity, $\Delta R/R$ is shifted towards zero and maintains its $\cos^2\theta$ form. It does not appear that there is any unexpected changes to the angular dependence as a result of these extra peaks.

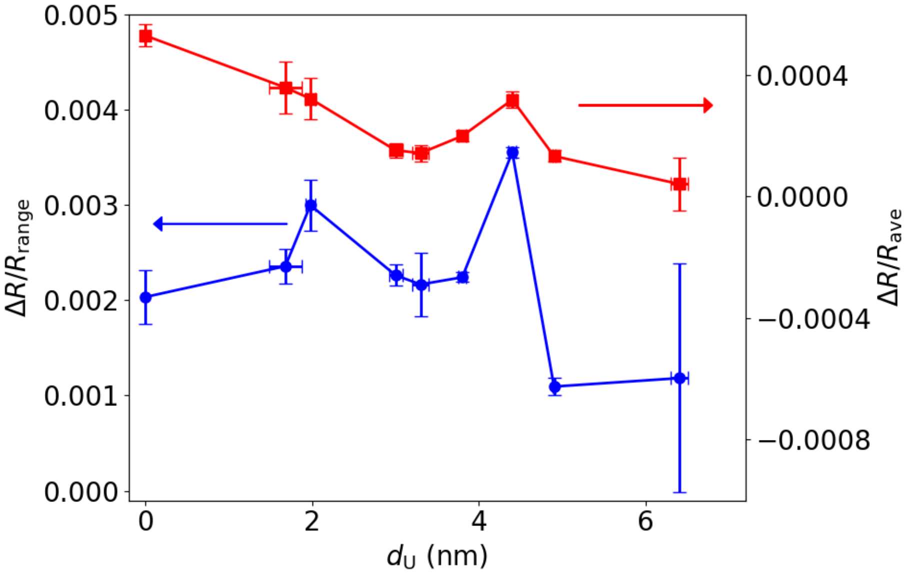

Figure 5.13: The range (blue circles) and average (red squares) of the anisotropic magnetoresistance across the iron/uranium bilayer series. The range shows clear monotonic behaviour while the average appears to follow are more linear trend.

To understand how this magnetoresistance is altered as a function of uranium thickness, it was quantified by the average and range of $\Delta R/R$, as was done with the peak positions, which can be found in fig.5.13. The range of the anisotropic magnetoresistance quantifies the change is resistance between the parallel and perpendicular orientations. It is equivalent to eqn.5.3 and can also be referred to as the anisotropic magnetoresistance ratio. The values of $\Delta R/R_{\mathrm{range}}$ across the series are comparable to literature values for other magnetic materials, e.g. $\Delta R/R_{\mathrm{range}} = 0.0019$ for Py [134]. Looking at the range as a function of uranium thickness, it is clearly non-monotonic. In the iron/uranium systems, there is expected to be an oscillatory induced magnetic moment in the uranium as a result of strong hybridisation of the d and f orbitals [13], which may help to explain this phenomenon. Work by Li. *et al.* [135] observed an initial increase in the anisotropic magnetoresistance ratio of an Fe/Pt system with increasing Pt thickness. This then dropped off past a critical thickness, $\sim 2\,\mathrm{nm}$. The enhancement in AMR is most clear at 10 K, but is still visible at room temperature. The increase was attributed to spin polarisation in the Pt conduction band resulting from the induced magnetic moment. As the induced moment in the Fe/U systems is expected to oscillate, it is plausible that the AMR ratio would oscillate concomitantly, and is a results of $d-f$ scattering. Further work by Li *et al.* into Fe/Au systems [136] reported low temperature oscillations in the AMR as a result of quantum well states. As it is expected that it is the QWSs which drive the proximity induced magnetisation, the oscillations here are more likely a consequence of the QWSs. The visibility of these oscillations at room temperature is presumably due to the strong hybridisation but may be enhanced by PIM in the uranium layer. The decrease of $\Delta R/R_{\text{range}}$ to values below that of the ferromagnetic layer only is often attributed to a shunt resistance, and is likely what has happened at $d_{\text{U}} > 5\,\text{nm}$.

The average $\Delta R/R$ represents the symmetry of the curve, and is a measure of the offset of $\Delta R/R$ around zero. In fig.5.13, the average decreases with d_{U} , with the exception of a small peak at 4.4 nm.

5.4.2 Ni-Based

Analysis for the nickel/uranium samples was carried out in the same manner as for iron/uranium, with a linear background due to heating being subtracted where appropriate. As with the iron series, there were some samples which could not be successfully patterned and etched. In this section, samples 1321 ($d_{\text{U}} = 1.5\,\text{nm}$), 1329 ($d_{\text{U}} = 6.9\,\text{nm}$), and 1330 ($d_{\text{U}} = 7.5\,\text{nm}$) have been omitted for this reason.

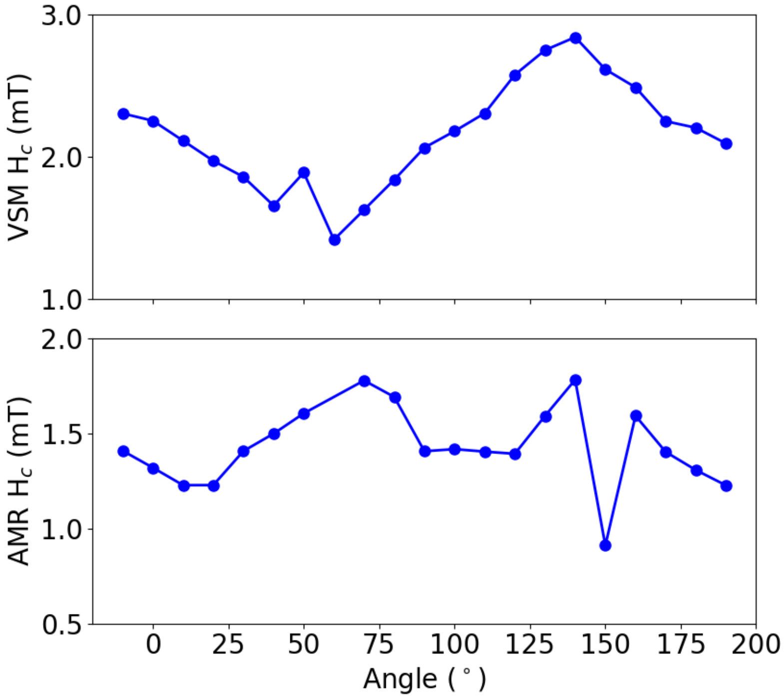

Figure 5.14: Comparison of the coercive field of a nickel thin film as a function of angle from vibrating sample magnetometry (top panel) and anisotropic magnetoresistance (bottom panel). Error bars not drawn here to preserve clarity.

Comparing again the VSM and AMR coercive fields, fig.5.14, it appears that the AMR peak positions follow a similar form to their VSM counterparts, with two peaks around 90° apart. The dip at 150° is likely due to ambiguity in the peak position as a result of noise and has a correspondingly large error not illustrated here to maintain clarity. However, for the nickel series $\mu_0 H_c^{\mathrm{AMR}}$ was found to be around half of $\mu_0 H_c^{\mathrm{VSM}}$, similar to observations of $\mu_0 H_c^{\mathrm{AMR}}$ and $\mu_0 H_c^{\mathrm{VSM}}$ in iron. In comparison with iron, $\mu_0 H_c^{\mathrm{AMR}}$ of Ni is significantly lower, as expected based on the VSM data. Unfortunately, due to the small change in field between angles, it was not possible to extract H_c for the complete nickel series, so this section will focus only on $\Delta R/R$.

The form of $\Delta R/R$ with angle for the nickel-based samples also appears to follow the $\cos^2\theta$ dependence, with maxima usually found at 0° and 180°. When compared to iron, the asymmetry around $\Delta R/R$ =0 is more pronounced. While in the positive magnetoresistance configuration, i.e. 0° & 180°, $\Delta R/R$ is ~0.002, whereas the negative configuration $\Delta R/R \sim$ -0.001.

Fig.5.16 depicts the evolution of $\Delta R/R_{\mathrm{range}}$ and $\Delta R/R_{\mathrm{ave}}$ with d_{U} . With the exception of d_{U} = 2.9 nm, $\Delta R/R_{\mathrm{range}}$ appears to be roughly linear. As there is no induced moment, an enhancement of the anisotropic magnetoresistance ratio should not be present. However, oscillations may still be expected due to the presumed presence of quantum well states. As the hybridisation is likely weak in the Ni/U systems [106], it may be the case that the QWSs do not contribute to AMR at room temperature [136]. It is unclear why the the point at $d_{\mathrm{U}} = 2.9$ lies much higher in both $\Delta R/R_{\mathrm{range}}$ and $\Delta R/R_{\mathrm{ave}}$. It is possible that it may result from a poor quality device, but it is unclear why this would cause such an increase.

The average appears to be non-monotonic, as it initially decreases then increases at higher d_{U} . This clearly illustrates the asymmetry of the magnetoresistance as a function of angle. It also appears that $\Delta R/R_{\mathrm{ave}}$ tends to be greater for nickel-based thin films than for iron. It is not clear what could introduce this asymmetry in the systems.

5.5 Conclusion

Samples were patterned into Hall bars through a process of optical lithography and wet etching to provide a defined current path for transport measurements. Angular anisotropic magnetoresistance measurements allowed for comparison of coercive fields and anisotropy with data procured by vibrating samples magnetometry through analysis of peak positions. Additionally, the anisotropic magnetoresistance ratio was hoped to reveal information of the electronic nature

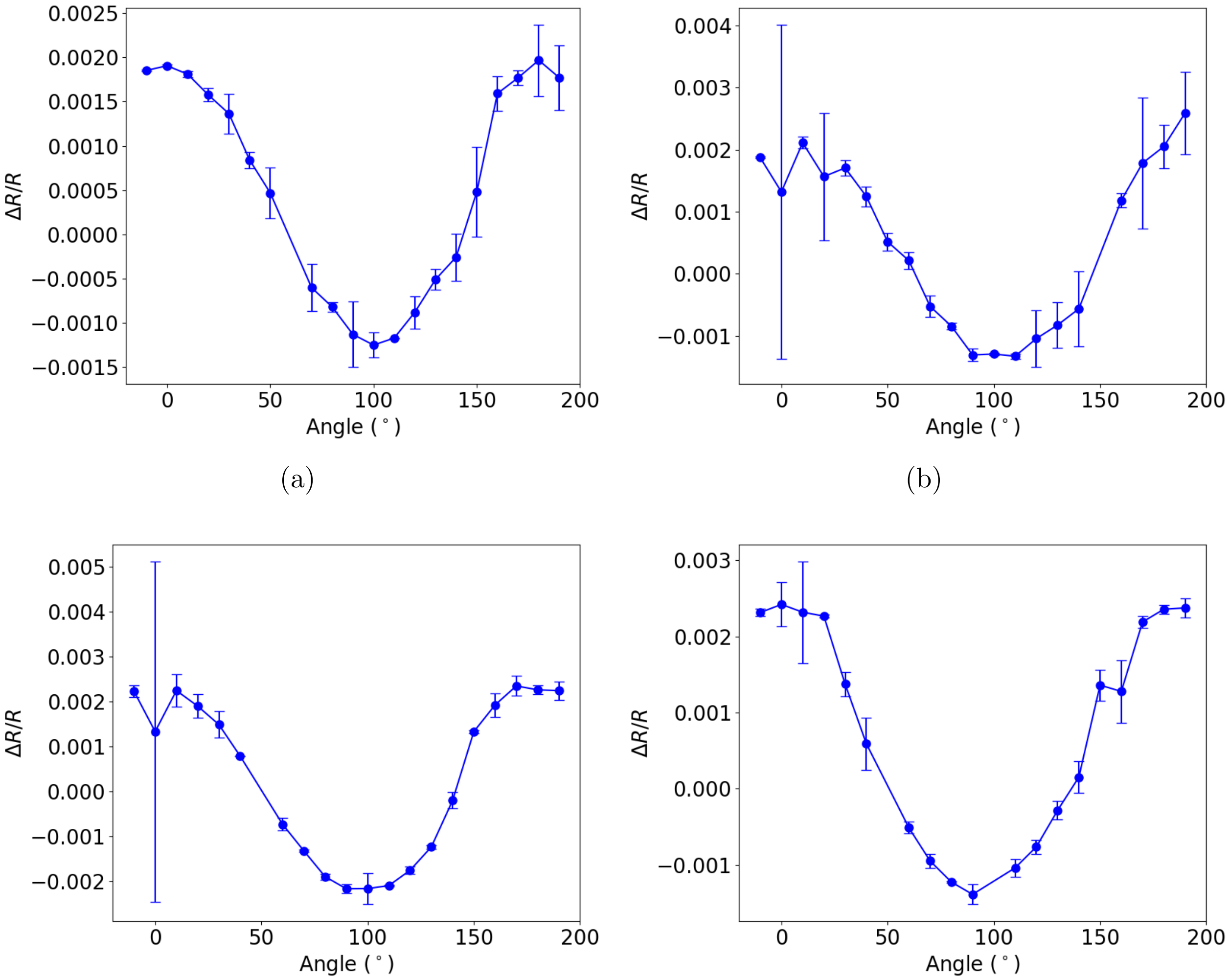

(a) (b)

(c) (d)

Figure 5.15: Normalised change in resistance as a function of angle for a selection of samples in the Ni/U series. All samples follow the expected $\cos^2$ form associated with AMR. a) d_{U} =0 nm b) d_{U} =0.6 nm c) d_{U} =4.3 nm d) d_{U} =6.1 nm

of these systems and any consequences of $d-f$ scattering.

Evidence of oscillations were observed for the iron/uranium series in both the average coercive field and in $\Delta R/R_{\mathrm{range}}$. These oscillations are most likely a result of quantum well states pesent within the uranium layer. However, typically these states cannot be observed at room temperature in AMR. The increased visibility of these oscillations may be a result of enhancement due to the presence of the induced moment within the U layer.

In comparison, very little could be discerned from anisiotropic magnetoresistance ratio in Ni/U thin films. Further measurements are required to determine if quantum well states can

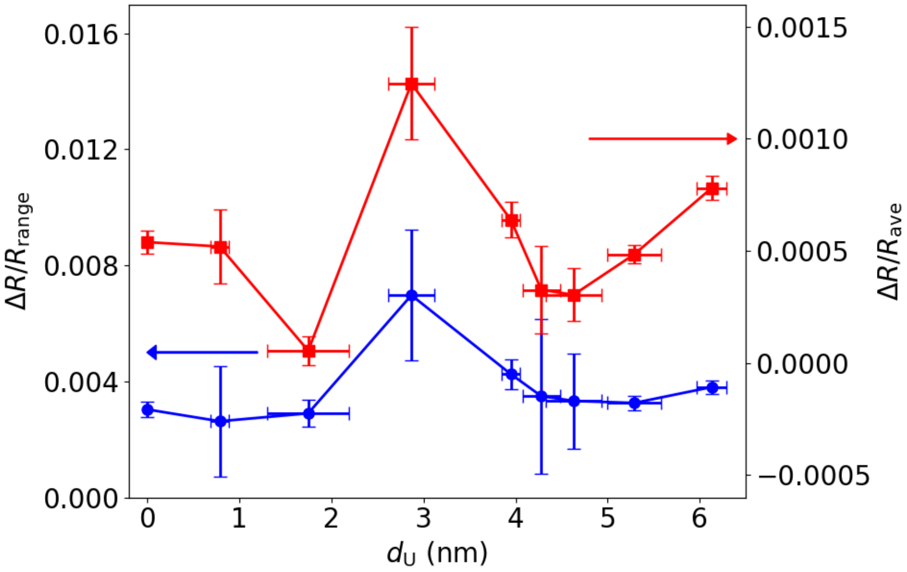

Figure 5.16: $\Delta R/R_{\rm range}$ (blue circles) and $\Delta R/R_{\rm ave}$ (red squres) as a function $d_{\rm U}$. $\Delta R/R_{\rm range}$ is roughly linear with $d_{\rm U}$ whereas $\Delta R/R_{\rm ave}$ changes non-monotonically due to changes in the symmetry of $\Delta R/R$ as a function of angle

be observed in the nickel series, as they may only be observable at low temperatures due to weak hybridisation with the uranium $5f$-orbitals.

Chapter 6

Ferromagnetic Resonance

6.1 Set-up

Ferromagnetic resonance (FMR) measurements of nickel bilayers were carried out using an Active Spectrum MicroESR system. In this system, the microwave field **h** is fixed in frequency. This system uses X-band frequencies (∼9.8 GHz), with the resonator cavity operating in the TE_{102} mode, as illustrated in fig.6.2a. The applied DC magnetic field **H** can be swept from 20.7 – 420.7 mT and **H** is applied perpendicular to **h**. The applied field is modulated with a small AC field, and the power absorption measured through lock-in detection.

Samples were secured to a suprasil rod with a small amount of vacuum grease and placed in a quartz tube. These samples are oriented so they can rotate from in-plane to out-of-plane, as shown in fig.6.1. As with the previous angular measurements, bilayer samples were rotated from -10° – 190° in 10° ± 2° increments. The estimate of the error in angle accounts for a number of factors including the alignment of the goniometer, the alignment of the applied field within the cavity, and rotation of the sample rod within the tube. The samples were suspended inside the resonator cavity and held at a constant height throughout all measurements. At each angle, the field was swept from 50 – 420.7 mT with a step size of 0.017 mT. Each scan ran three times giving the average power absorption. Between each angle, the impedance of the cavity was tuned to account for changes induced by the presence of the sample. The system provides a measure of the differential power absorption with applied DC field, seen in fig.6.2b.

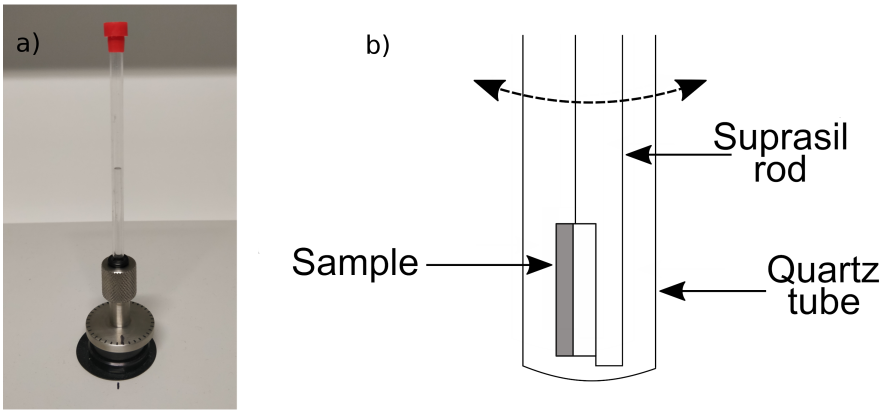

Figure 6.1: a) Custom goniometer to facilitate angular measurements using MicroESR system. b) Illustrative representation on sample placement inside the quartz tube. Samples can be rotated from in-plane to out-of-plane.

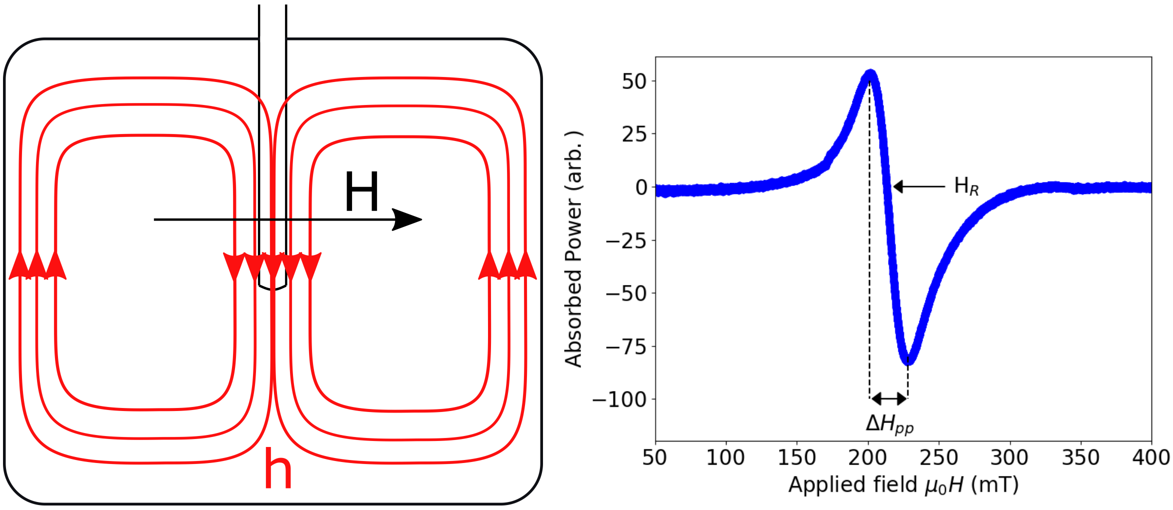

(a)

(b)

Figure 6.2: a) Geometry of fields within the MicroESR system. The red arrows represents the path the microwave magnetic field **h** follows in a TE_{102} cavity. The sample is held at the point where the microwave field is homogeneous. The externally applied magnetic field **H** is represented by the black arrow. b) Typical data set obtained using MicroESR system. H_R and ΔH_{pp} are the resonance field and peak-to-peak width respectively.

6.2 Analysis

The following analysis is set out in CGS units as this is the most common choice in the literature. The data are, however, presented in SI units to maintain consistency with the other results in this thesis.

The analysis of the ferromagnetic resonance data in this chapter follows that of Mizukami *et al.* set out in refs. [137] & [138]. The geometry of the fields and magnetisation with respect to the film is detailed in fig.6.3.

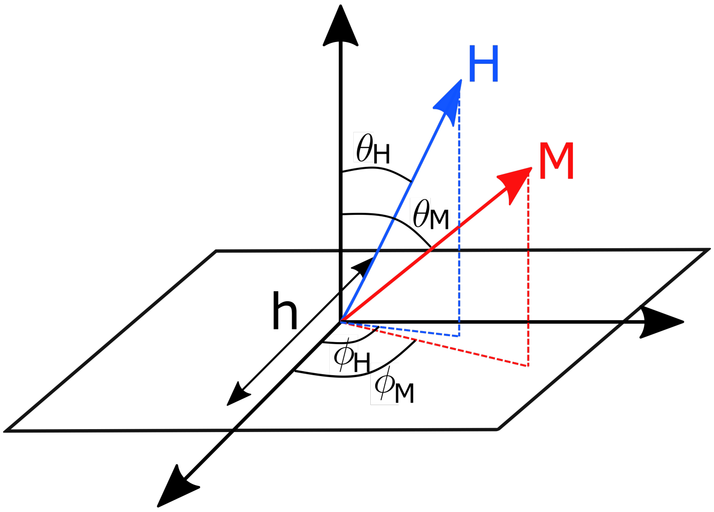

Figure 6.3: Geometry of a sample within the FMR system. The microwave field h is always applied in the plane of the sample, while the samples can be rotated so the applied magnetic field H rotates from in-plane to out-of-plane. The magnetisation of the sample M tracks with the applied field.

The energy density of this thin film system, when looking at rotation from in-plane to out-of-plane is defined as

$$\varepsilon = -\mathbf{M}\cdot\mathbf{H} + 2\pi M_s \cos^2\theta_M - K\cos^2\theta_M. \tag{6.1}$$

In this equation, the first term represents the Zeeman energy, the second is the thin film demagnetisation term, and the final term represents an effective uniaxial anisotropy. When using the coordinate system illustrated in fig.6.3, this expands to

$$\begin{aligned}\varepsilon = -M_s H[\sin\theta_H \sin\theta_M \cos(\phi_H - \phi_M) + \cos(\theta_H - \theta_M) - \sin\theta_H \sin\theta_M] \\ + 2\pi M_s \cos^2\theta_M - K\cos^2\theta_M.\end{aligned} \tag{6.2}$$

On resonance $\partial\varepsilon/\partial\phi_M = 0$ and $\partial\varepsilon/\partial\theta_M = 0$, allowing ϕ_M and θ_M to be determined. From the first condition it can be seen that $\phi_H = \phi_M$. The second condition provides an equation for θ_M

which can be solved numerically,

$$\sin(2\theta_M) = \frac{2H_R}{4\pi M_{\text{eff}}}\sin(\theta_M - \theta_H). \tag{6.3}$$

Here $4\pi M_{\text{eff}} = 4\pi M_s - 2K/M_s$ and is thought of as the effective demagnetisation field and H_R is the resonance field. The resonance field is taken as the point at which the measured power absorption crosses through zero, from positive to negative. When converted to SI units $4\pi M_{\text{eff}}$ is referred to as M_{eff}. Expanding the resonance condition equation determined by Suhl [50],

$$\omega_{res} = \frac{\gamma}{M\sin\theta_M}\left[\frac{\partial^2\varepsilon}{\partial\theta_M^2}\frac{\partial^2\varepsilon}{\partial\phi_M^2} - \left(\frac{\partial^2\varepsilon}{\partial\theta_M\partial\phi_M}\right)^2\right]^{1/2}, \tag{6.4}$$

using eqn.6.2 produces,

$$\left(\frac{\omega_{res}}{\gamma}\right)^2 = \left(H_R\cos(\theta_H - \theta_M) - 4\pi M_{\text{eff}}\cos^2\theta_M\right)\left(H_R\cos(\theta_H - \theta_M) - 4\pi M_{\text{eff}}\cos 2\theta_M\right). \tag{6.5}$$

Taking $4\pi M_{\text{eff}}$ and g as optimisation parameters and solving for H_R, a fit to the angular resonance field data can be found.

After determining suitable values of M_{eff} and g, the peak-to-peak width data can be fitted. The peak-to-peak width is composed of intrinsic and extrinsic contributions. The intrinsic contribution can be quantified by,

$$\Delta H_{pp}^{\text{in}} = \frac{1}{\sqrt{3}}\frac{\alpha}{M}\left|\frac{d(\omega_{res}/\gamma)}{dH}\right|^{-1}\left(\frac{\partial^2\varepsilon}{\partial\theta_M^2} + \frac{1}{\sin^2\theta_M}\frac{\partial^2\varepsilon}{\partial\phi_M^2}\right). \tag{6.6}$$

The factor of $1/\sqrt{3}$ comes from the conversion from FWHM to the peak-to-peak width [138]. If there are inhomogeneities within the film, which result in frequency independent variation of the sample properties there will also be an extrinsic contribution [138, 139], given by

$$\Delta H_{pp}^{\text{ex}} = \frac{1}{\sqrt{3}}\left(\left|\frac{dH_r}{d4\pi M_{\text{eff}}}\right|\Delta 4\pi M_{\text{eff}} + \left|\frac{dH_r}{d\theta_H}\right|\Delta\theta_H\right). \tag{6.7}$$

The total peak-to-peak width due to both intrinsic and extrinsic broadening is given as

$$\Delta H_{pp} = \Delta H_{pp}^{\text{in}} + \Delta H_{pp}^{\text{ex}}. \tag{6.8}$$

Here $\Delta 4\pi M_{\text{eff}}$ and $\Delta\theta_H$ are the dispersion of the magnitude of $4\pi M_{\text{eff}}$ and its direction respectively. In order to determine ΔH_{pp}, the peak-to-peak data is fitted using eqn.6.8, with α, $\Delta 4\pi M_{\text{eff}}$ and $\Delta\theta_H$ as optimisation parameters.

6.3 Results

Standard resonance curves for various thickness of uranium are displayed in fig.6.4. These curves are from measurements in the in-plane geometry and take the form of the first derivative of a Lorentzian. The addition of uranium has a clear effect on both the resonance field – zero power crossing point in fig.6.4a – and the peak-to-peak width of the samples, fig.6.4b. Additionally, it can be seen that in all curves there is an asymmetry of the Lorentzian line shape in the power absorption. This asymmetry most likely arises from exchange effects. These effects can arise from changes in the magnetisation of the ferromagnetic layer caused by inhomogeneities in the film and the skin depth of the ferromagnet [140].

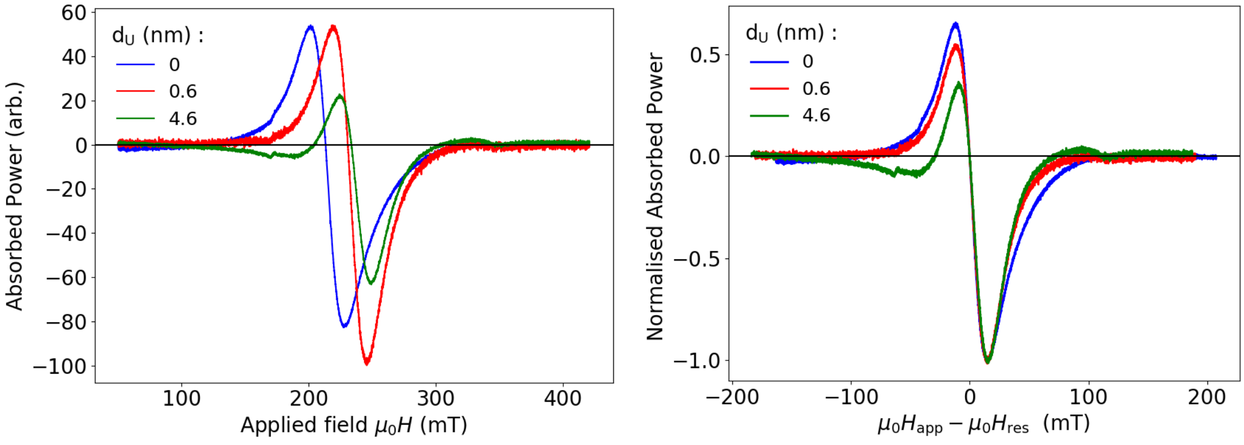

(a) (b)

Figure 6.4: Overlay of in-plane ferromagnetic resonance data for three different thickness of uranium; $d_{\mathrm{U}} = 0\,\mathrm{nm}$ (blue), $d_{\mathrm{U}} = 0.8\,\mathrm{nm}$ (red), and $d_{\mathrm{U}} = 4.6\,\mathrm{nm}$ (green). a) Raw data showing the change in resonance field and power absorption as d_{U} is increased. b) Data normalised to the dip height and shifted by the resonance field. This illustrates the change in peak to peak width with changing d_{U}.

Due to this asymmetry of the curves, a standard Lorentzian derivative was not sufficient to fit to the data. Typically, a skewed Lorentzian is due to some convolution with a Gaussian. Here, the data maintained their Lorentzian line shape and could not be described as a mix of the two. Both cases can be seen in fig.6.5a. It was not clear how accurately describe this asymmetric Lorentzian mathematically. However, the resonance field and peak-to-peak widths were well defined so, in order to move past this asymmetry issue, the resonance field was determined by a linear fit to the section between the positive and negative peaks, and is taken as the point at which the fit crosses the x-axis. The peak-to-peak width was ascertained by fitting each peak as a third order polynomial, illustrated in fig.6.5b.

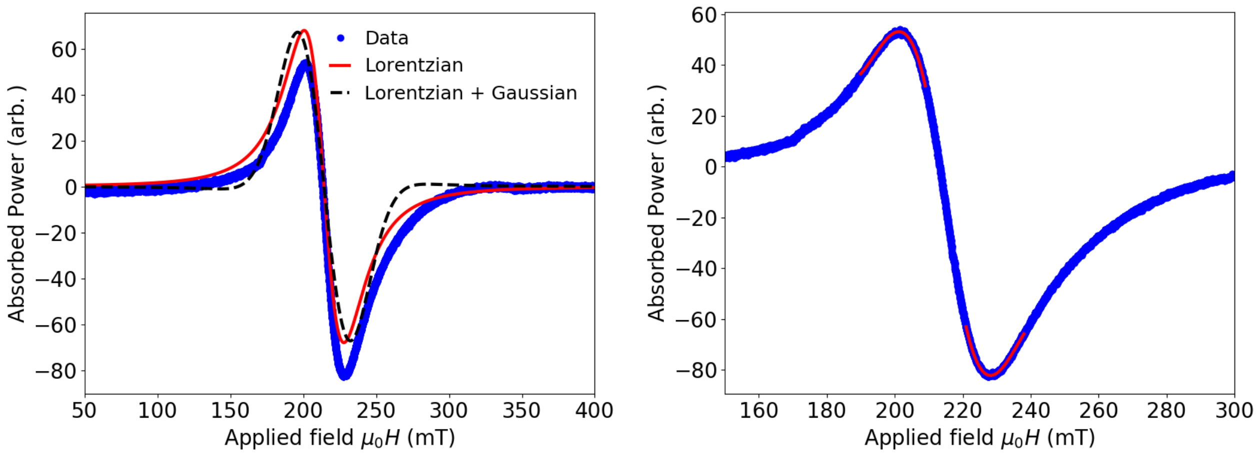

(a)

(b)

Figure 6.5: a) Standard Lorentzian derivative (solid red) and Lorentzian-Gaussian (dashed black) fitted to the FMR curve (blue). b) Third order polynomial fit (red) to determine the peak-to-peak width of the FMR curve.

Examining the resonance field and peak-to-peak widths at $\theta_H = -90^\circ$ provides a preliminary overview of the dynamics of the system. Studying the resonance field provides information about the magnetic anisotropy, as described by eqn.6.3. In chapter 6.13, the magnetic anisotropy was observed to oscillate possibly as a result of quantum well states. It is expected that this behaviour would be mirrored in the resonance data[1], presented in fig.6.6. While it may be possible that oscillations are present, the resolution of the measurement is too low to say this with certainty, though the spread of resonance fields at large d_{U} may be an indication of oscillations of magnetic anisotropy.

From eqn.6.8, it is the peak to peak width which contains information about the damping of the system. Work by Mizukami *et al.* [138] on Py/Pt systems suggest that ΔH_{pp} should become approximately constant at thicknesses greater than 1 nm, as depicted in fig.6.7. This suggests that there is a critical thickness above which there is no added effect to the damping of the system.

---

[1] It is worth mentioning that while we may have oscillation in anisotropy from both VSM and FMR measurements, the functional form of the two cannot be directly compared, as the VSM data looks at rotations in-plane and FMR in-plane to out-of-plane.

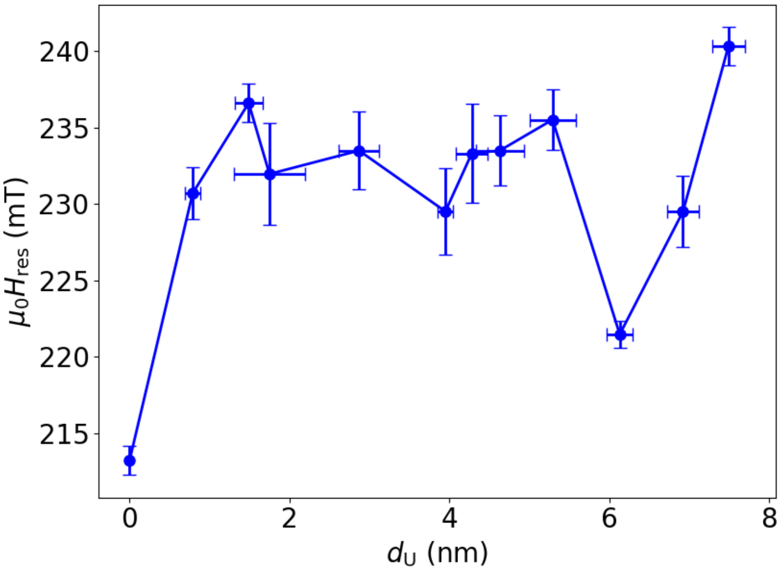

Figure 6.6: Dependence of the resonance field on d_{U}, taken from FMR measurements when the field is oriented in the plane of the film. There is a clear increase in the resonance field with the addition of a uranium layer, suggesting an increase in anisotropy. Given the resolution, it is unclear whether there are oscillations in the field throughout the series.

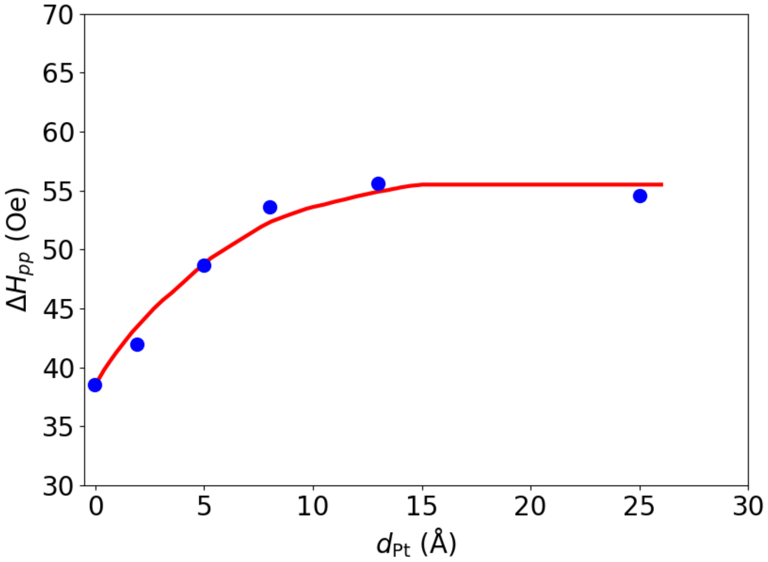

Figure 6.7: ΔH_{pp} as a function of platinum thickness measured with applied field in the plane of the film. This increases until around 1 nm where it then plateaus, suggesting damping saturates at a critical thickness. Adapted from ref. [138]

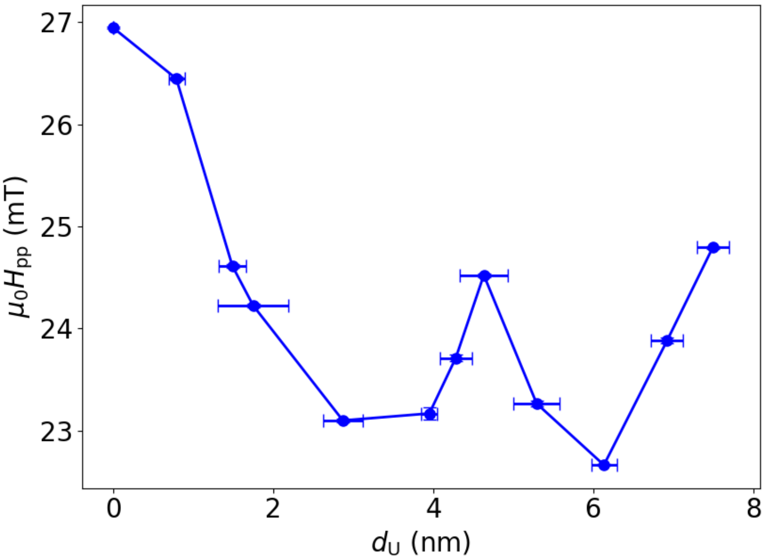

Figure 6.8: Change in peak to peak field as a function of uranium thickness for field in-plane. Unexpectedly, there is an initial decrease in peak to peak field with the addition of uranium. The peak-to-peak field then appears to oscillate. This may suggest some oscillation in the damping of these systems.

This does not appear to be the case for the uranium based system, as presented in fig.6.8. An initial decrease in ΔH_{pp} suggests that the addition of uranium is reducing the damping, acting as a spacer layer between the nickel and the niobium cap. At higher $d_{\rm U}$, the peak-to-peak width begins to oscillate. However, to understand fully the dependence of damping on uranium thickness, we must turn to the angular data.

Fig.6.9 presents a selection of FMR curves for $d_{\rm U} = 0$, 0.6, 4.3 and 7.5 nm. These curves have been normalised to the lower lobe height in absorbed power and shifted around the resonance field. Each plot shows the changing peak-to-peak width with angle. For each sample, the peak to peak width increases as the sample is moved towards the out-of-plane orientation.

In some measurements, a dip is observed before the resonance peak, particularly obvious in fig.6.9c. This feature is from a background signal from the sample holder. It is most apparent in samples where the overall power absorption is low. However, this background does not appear to interfere with the resonance field and peak to peak widths, which all follow the expected trend irrespective of this addition.

To follow the analysis presented in section 6.2, first the resonance field at each angle was determined. A selection of these data for various $d_{\rm U}$ can be seen in fig.6.10. For a majority of the samples, there are no data between 70° & 120°. At these angles, the applied field was

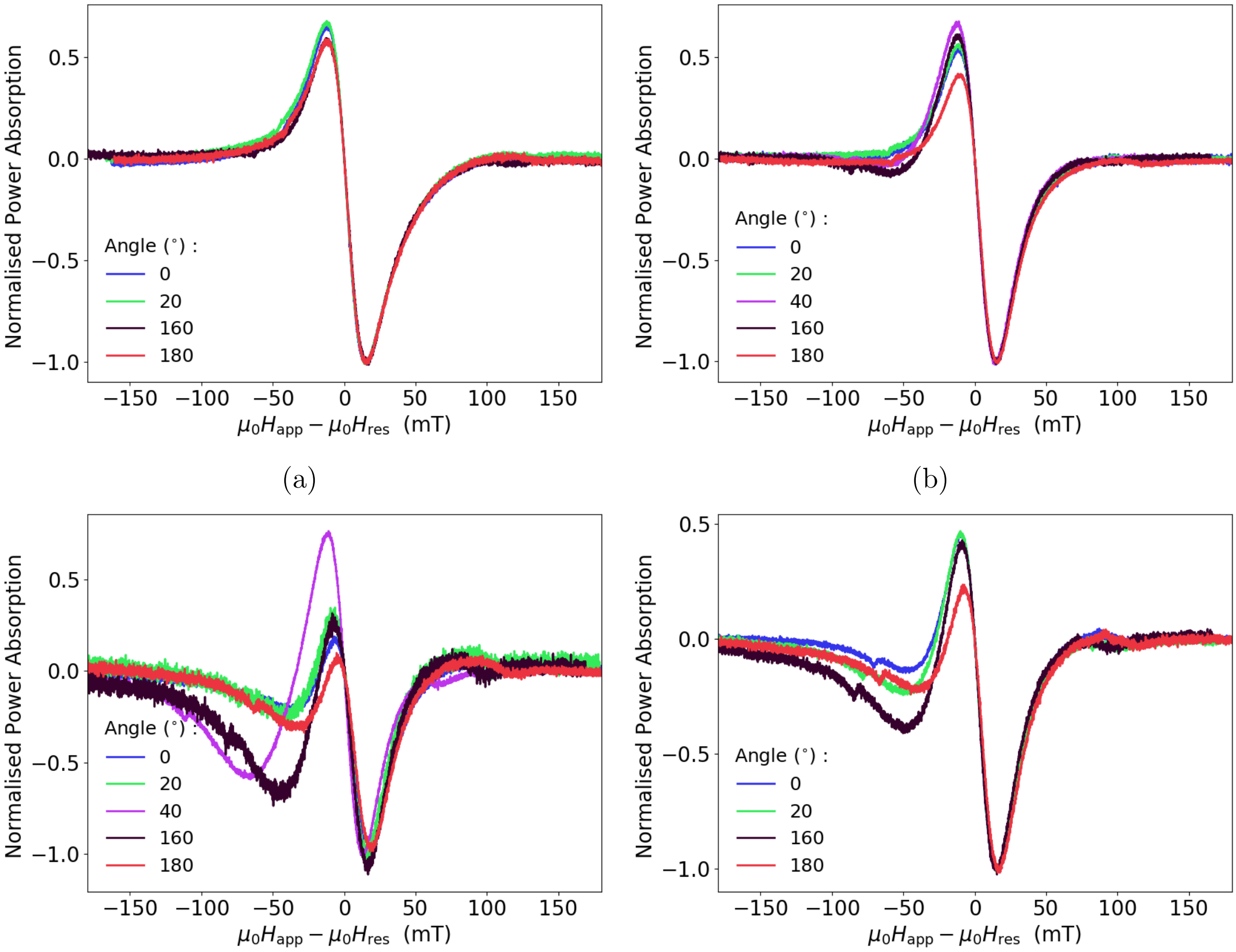

(a) (b)

(c) (d)

Figure 6.9: Ferromagnetic resonance curves normalised to the lower lobe height and shifted around the resonance field positions. Each figure shows the change in power absorption and peak to peak width with angle. In all cases, the peak-to-peak width increases around the out-of-plane orientation. a) $d_{\text{U}} = 0\,\text{nm}$ b) $d_{\text{U}} = 0.6\,\text{nm}$ c) $d_{\text{U}} = 4.3\,\text{nm}$ d) $d_{\text{U}} = 7.5\,\text{nm}$.

insufficient to reach resonance [141]. There are a small number which do exhibit resonance at 70° or 120° but again, nothing can be reached beyond these angles within the accessible field range. However, while this may increase the error associated with the fit, values for M_{eff} and g can still be easily determined. The best fits to these data are given by the solid red lines in fig.6.10.

The best fit to each data set was determined by minimising χ^2. For sample SN1330, the optimisation of M_{eff} and g can be found in fig.6.11. This contour plot demonstrated how χ^2 varies as a function of both quantities. For this sample, the optimisation determined that

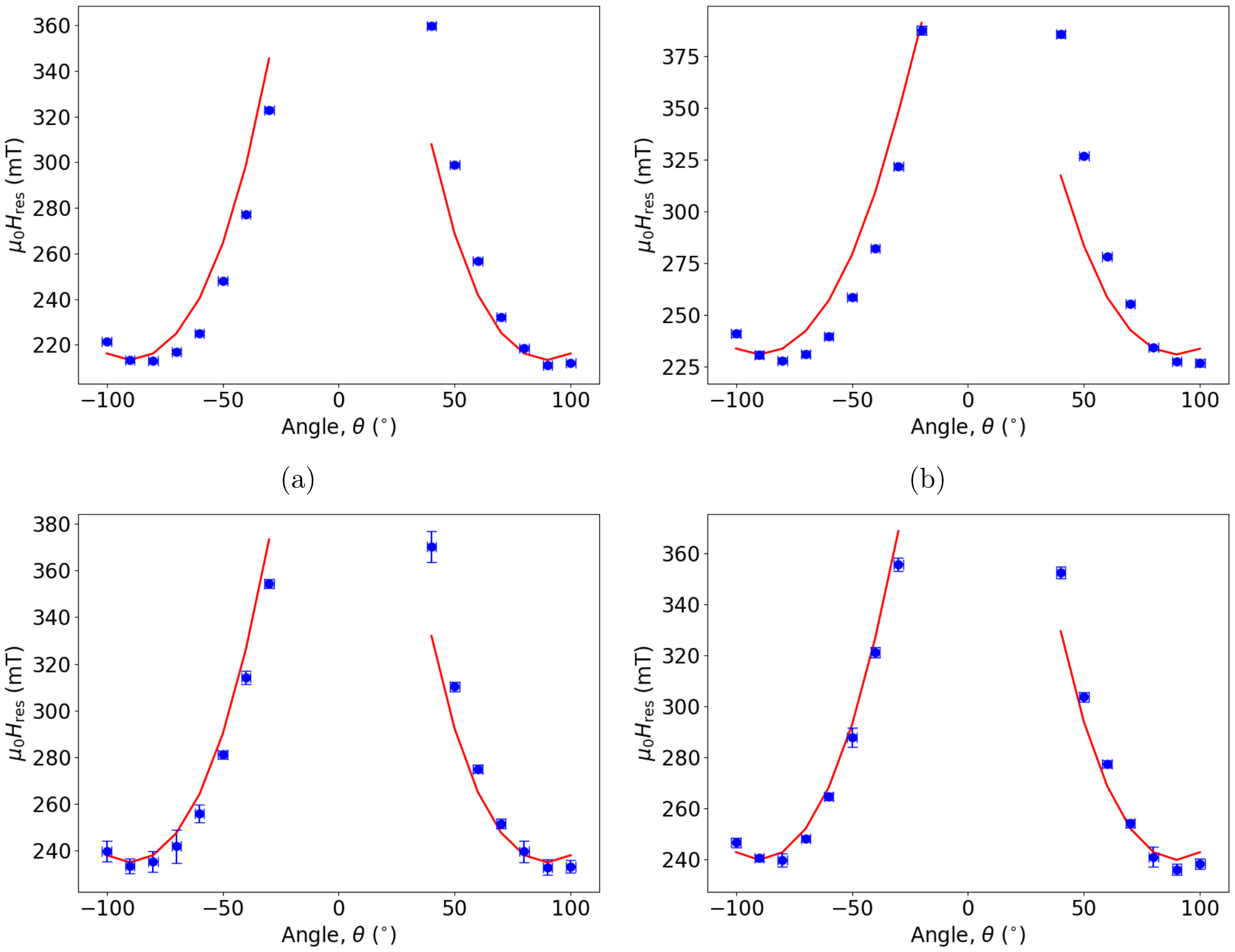

(a) (b)

(c) (d)

Figure 6.10: Resonance field data (blue) as a function of angle. Data fitted by numerically solving eqns.6.3 & 6.5. Fits to data given by red lines. a) $d_U = 0\,\mathrm{nm}$ b) $d_U = 0.6\,\mathrm{nm}$ c) $d_U = 4.3\,\mathrm{nm}$ d) $d_U = 7.5\,\mathrm{nm}$.

$M_{\mathrm{eff}} = (1.3{\pm}0.4) \times 10^5\,\mathrm{Am}^{-1}$ and $g = 2.260 \pm 0.017$. Slices from the contour plot at $M_{\mathrm{eff}} = 1.3{\times}10^5\,\mathrm{Am}^{-1}$ and $g = 2.26$ can be seen in figs.6.12a & 6.12b respectively. From these plots, it can be seen that χ^2 varies more rapidly with changing g than with M_{eff} .

For samples where χ^2 is "small" – $\chi^2 < 100$ – the errors in M_{eff} and g were taken as the change in each required to increase χ^2 by 5%. Where χ^2 is greater than 100, such as fig.6.10a, it appeared that the fits were systematically shifted to the left of the data. In these cases, the data was shifted by the 2° error in angle and refitted. This was found to reduce χ^2 in all cases. From this, the error in M_{eff} and g were taken as the difference between the optimised values of

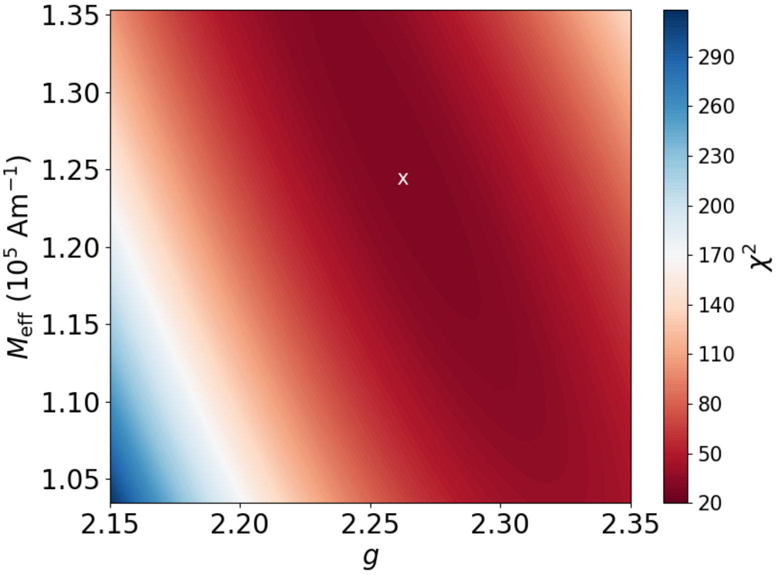

Figure 6.11: Optimisation of χ^2 as both M_{eff} and g vary represented as a contour plot. Low χ^2 corresponds to deep red and for this sample ($d_{\mathrm{U}} = 7.5\,\mathrm{nm}$) the minimum was found to be at $M_{\mathrm{eff}} = 1.24{\times}10^5\,\mathrm{Am}^{-1}$ and $g = 2.26$,given by the white 'X'.

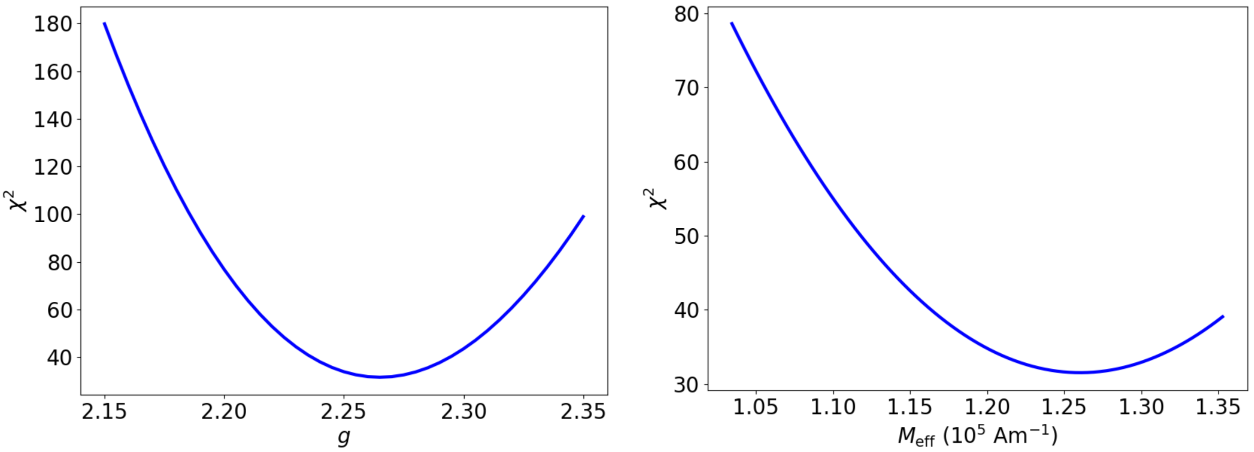

(a)

(b)

Figure 6.12: Slices of the contour plot in fig.6.11 which demonstrate how χ^2 vaires individually with M_{eff} and g. a) Variation of χ^2 with g when M_{eff} is fixed at $1.24{\times}10^5\,\mathrm{Am}^{-1}$. b) χ^2 as a function of M_{eff} with g fixed at 2.26.

the shifted and unshifted cases.

M_{eff} and g as a function of d_{U} can be seen in fig.6.13a. In both cases there seems to be oscillations with increasing d_{U} . When comparing with the in-plane resonance field in fig.6.6,

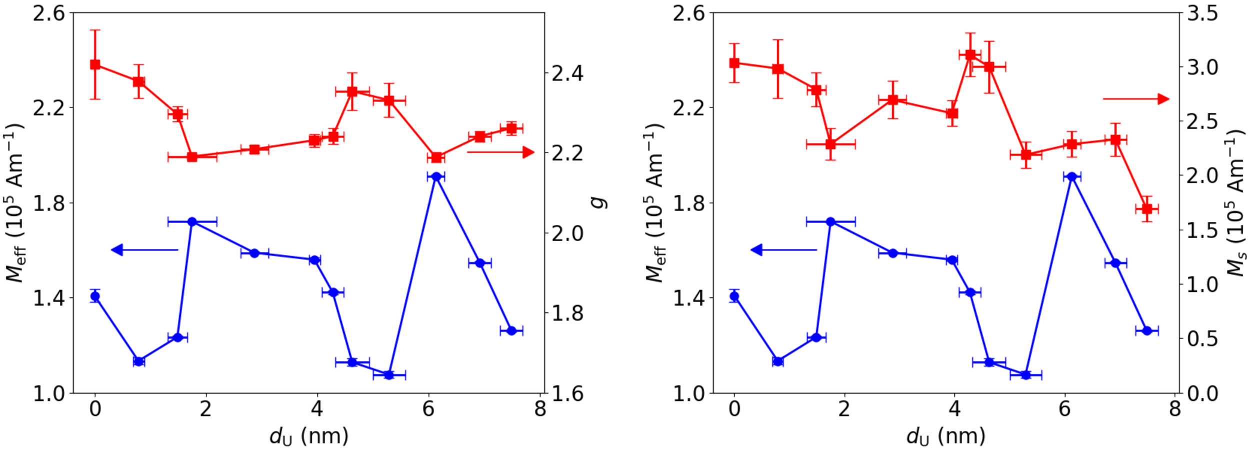

(a)

(b)

Figure 6.13: a) $M_{\rm eff}$ and g calculated from the resonance field fitting as a function of uranium thickness. $M_{\rm eff}$ and g follow an inverse relationship but both appear to oscillate. b) Comparison of $M_{\rm eff}$ with M_s determined from VSM measurements in chapter . While there is variation in M_s, it does not follow the same form as the variation in $M_{\rm eff}$, suggesting changes in the anisotropy are also present.

it appears that the form of $M_{\rm eff}$ is similar but inverted. These clear oscillations in $M_{\rm eff}$ suggest that the anisotropy of the samples as they are rotated from in-plane to out-of-plane is also governed by quantum well states. This is not unexpected as QWSs should affect the anisotropy in all geometries. $M_{\rm eff}$ is found to be smaller than the saturation magnetisation determined by vibrating sample magnetometer measurements in chapter 6.13, found in fig.6.13b, indicating a perpendicular anisotropy field which also oscillates.

The value of g for each samples is greater than that expected for a free electron, ~ 2. This is thought to be related to the spin-orbit coupling of the overlayer in contact with Ni [137]. Interestingly, g is larger for the Ni/Nb interface than for Ni/U.

Taking the fitted value of $M_{\rm eff}$, the peak-to-peak width as a function of angle could be fitted for each samples using eqn.6.8. A selection of these fits can be found in fig.6.14.

In some cases, such as that of fig.6.14d, there appears to be some asymmetry between $\mu_0 \Delta H_{pp}$ at positive and negative angles. It is unclear what causes this reduction in peak-to-peak width as other angular studies on ferromagnetic resonance of thin films appear symmetric round 0° [141]. It may be possible that it is due to precession of the sample within the cavity, resulting the the samples being off-centre during measurements. As a consequence of this asymmetry there will likely be a reduction in the damping parameter α.

Fig.6.15 shows the break down of the fit for $d_{\rm U} = 0.6\,{\rm nm}$ into its three components, $H_{pp}^{\rm in}$

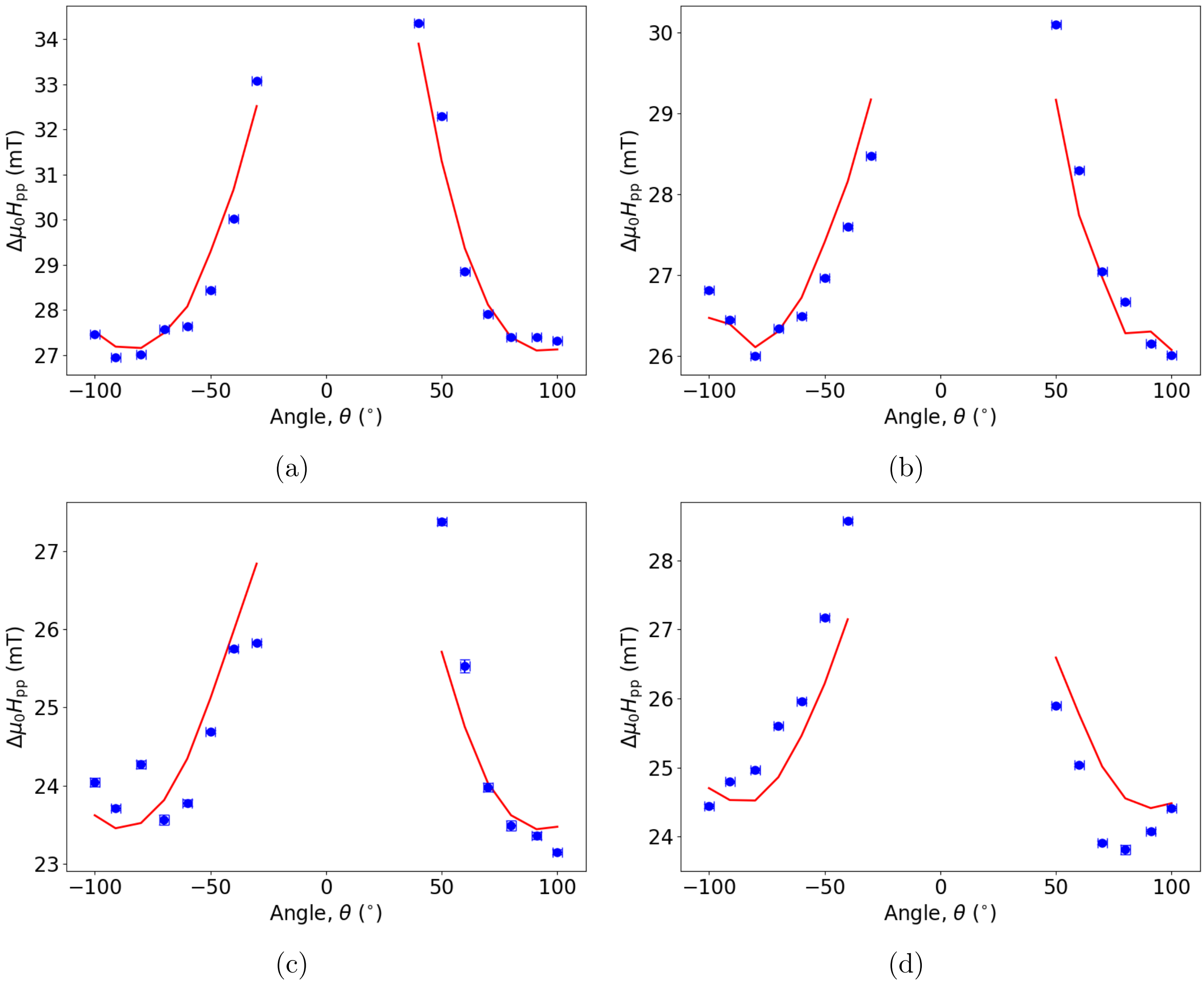

(a)

(b)

(c)

(d)

Figure 6.14: Peak-to-peak data (blue) as a function of angle. Fits to data given by red lines. a) $d_{\mathrm{U}} = 0\,\mathrm{nm}$ b) $d_{\mathrm{U}} = 0.6\,\mathrm{nm}$ c) $d_{\mathrm{U}} = 4.3\,\mathrm{nm}$ d) $d_{\mathrm{U}} = 7.5\,\mathrm{nm}$.

(black dashed) , ΔM_{eff} (green dotted), and $\Delta\theta_H$ (cyan dot-dash). For each sample, the dominant contribution comes from H_{pp}^{in}. This contribution is dependent on the damping of the system, given by eqn.6.6, and has a form quite distinct from the data. There is a similar upturn at high angles but the increase in linewidth in higher angles is much more gradual than the data, followed by an eventual downturn close to zero. The contribution denoted ΔM_{eff}, the first term in eqn.6.7, is related to the distribution of M_{eff} in a sample. This follows the form of the data reasonably but is insufficient to describe the data on its own. The final term of eqn.6.7 is dependent on $\Delta\theta_H$. This term appears to be the smallest contribution to the overall fit. This term is generally quite flat, with peaks around ±90°. This behaviour is slightly unexpected

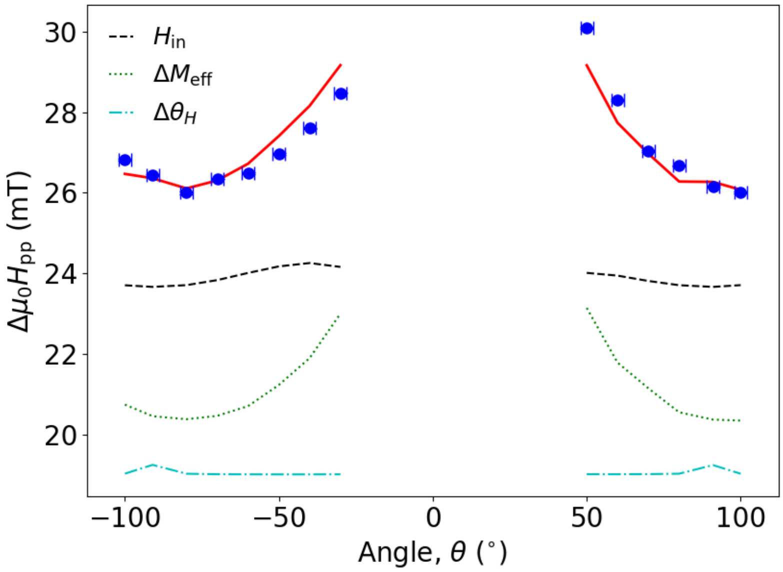

Figure 6.15: Contribution of the three components required to fit the peak-to-peak width; $H_{pp}^{\rm in}$ (black dash) which depends on the damping, and $\Delta M_{\rm eff}$ (green dotted) and $\Delta\theta_H$ (cyan dot-dash) which are both related to the structure of the film. Components shifted vertically upwards for clarity of form.

based on the break down of contributions that can be found in refs [137] & [138]. In these works, the contribution from $\Delta\theta_H$ is relatively flat until around 30° but there are no peaks around 90°. Mathematically, this component is expected to increase around ±90° and it appears that these points have been removed in refs. [137] & [138]. When these peaks are removed from the $\Delta\theta_H$ contribution the fit does not improve and in some cases where there are fluctuations in the data around ± 90°, χ^2 increases. Additionally, without these points, altering α and $\Delta M_{\rm eff}$ serves to only increase χ^2 more, so there is no change to the these parameters when minimising this new fit. It may be that there is little dispersion of θ_H within these samples, so a small or zero contribution may not be unrealistic, though without data around 0°, the full contribution from $\Delta\theta_H$ can only be speculated on.

For all samples, the peak-to-peak width drops at angles closer to zero. This is not unexpected from both the literature [137, 138, 141] and the form of the intrinsic contribution to the line width, give by black dashed line in fig.6.15. However, the narrowing of the line width observed in these data appears much more extreme than expected. This can be explained by the field limit of the MicroESR system. As illustrated by fig.6.16a, the resonance at angles close to the out-of-plane orientation is pushed close to the upper field limit, often with the absorbed power not able to return to zero. Without this return to zero absorbed power, the background

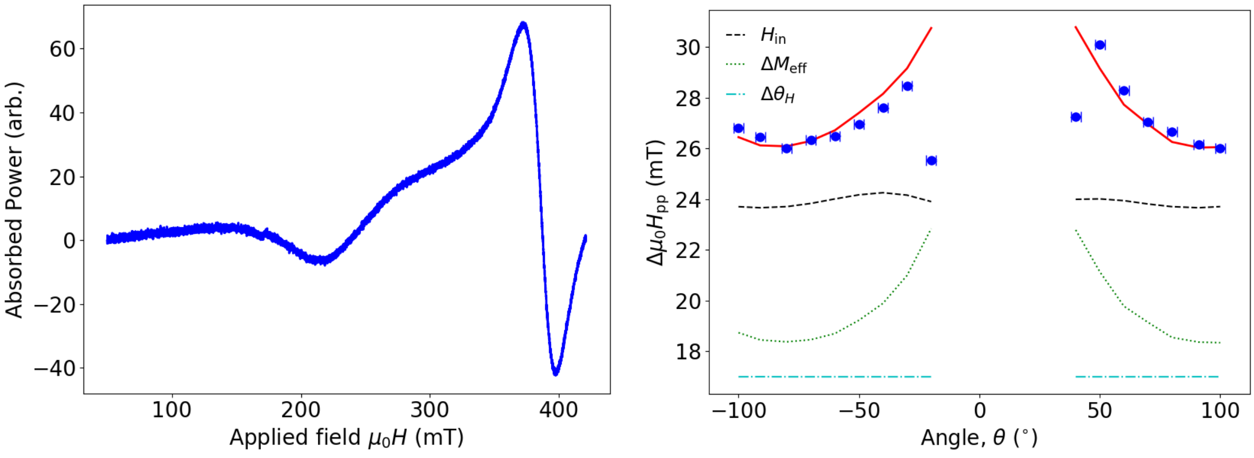

(a) (b)

Figure 6.16: a) Ferromagnetic resonance curve for applied field at -20°. The limited field range prevents the curve from returning to zero after the dip in absorbed power. b) Peak-to-peak data including angles at which the full curve could not be obtained, as well as the behaviour of the three components of the fit at these angles. Components shifted vertically upwards for clarity of form.

correction performed by the MicroESR system may introduce errors or may not be implemented correctly, resulting in the significantly smaller peak-to-peak width at these angles. Fig.6.16b shows these points at -20° and +30° and the corresponding fit judged best to the data. Looking at only the intrinsic component of this fit (black dashed line), there is a downturn expected at these angles, though not as steep as the one observed experimentally. For these reasons, it was determined that the low values of $\mu_0\Delta H_{pp}$ close to 0° was an artefact of the limited field range and therefore detrimental to the fit. By removing these points, the best fit could be found by minimising χ^2.

For samples 1320 ($d_{\mathrm{U}} = 0.6\,\mathrm{nm}$), χ^2 as a function of each the three parameters can be seen in fig.6.17. Comparing the three, it appears that χ^2 is most strongly dependent on the damping parameter α, then on ΔM_{eff}. Finally, while there appears to be little contribution from $\Delta\theta_H$, there is some dependence of the fit on this parameter. For each of these three parameters, the error was determined a the value required to change χ^2 by 5%, as with M_{eff} and g, with the exception of sample 1321 which will be discussed further on in this chapter.

Fig.6.18 shows how χ^2 of the total fit depends on the presence of the extrinsic parameters. The upper panel displays χ^2 when all three fitting parameters are involved, The middle panel looks at χ^2 when $\Delta\theta_H = 0$ and, finally the bottom panel only contains the intrinsic contribution.

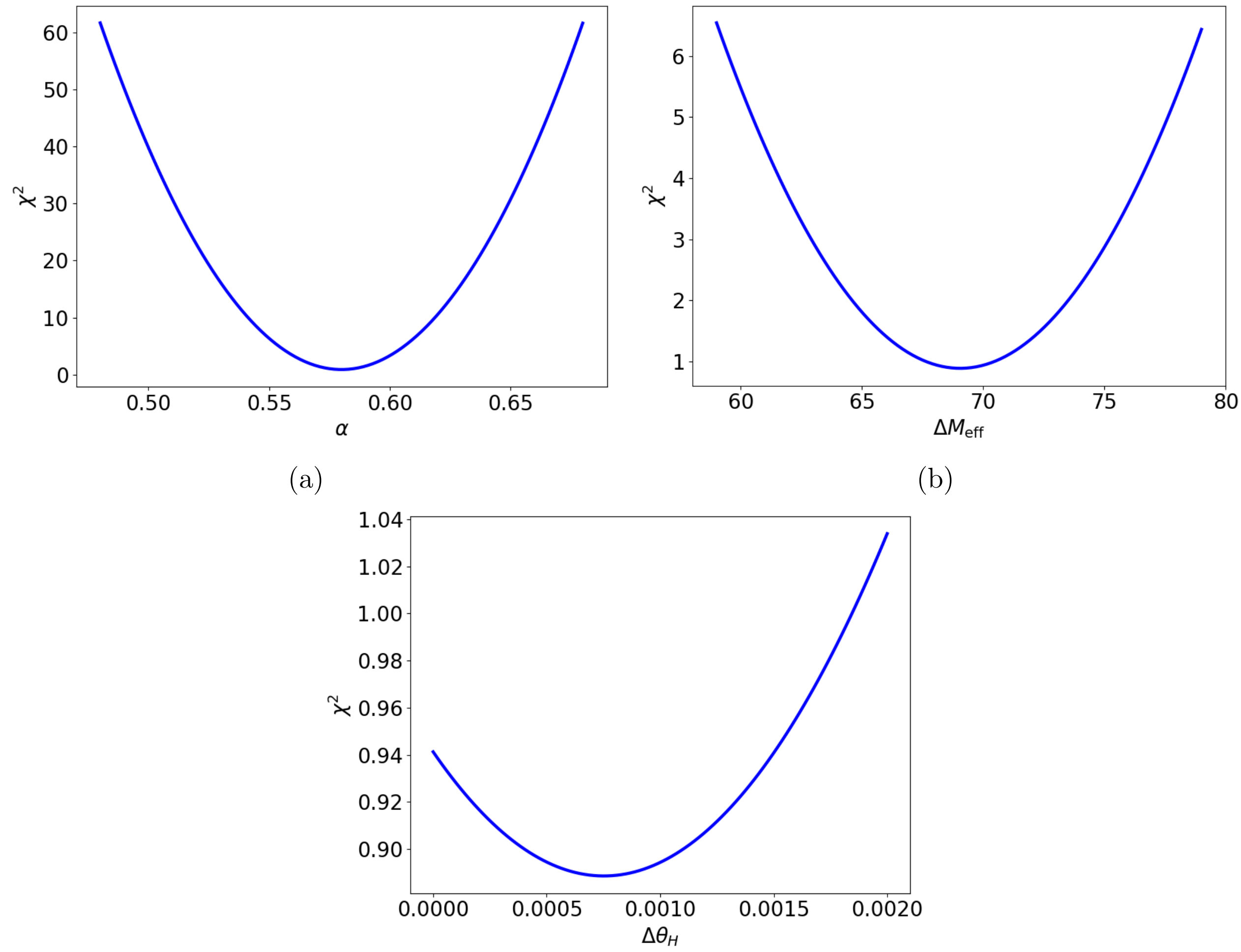

(a)

(b)

(c)

Figure 6.17: Variation of χ^2 with each of the three parameters required for a complete fit while other parameters remain constant. a) α varied with ΔM_{eff} $=5.49\times10^4\,\mathrm{Am}^{-1}$ and $\Delta\theta_H$ $=0.0008°$ b) ΔM_{eff} with α = 0.058 and $\Delta\theta_H$ $=0.0008°$ c) $\Delta\theta_H$ with α = 0.0058 and ΔM_{eff} $=5.49\times10^4\,\mathrm{Am}^{-1}$.

When comparing the three there is little obvious difference between the upper and middle panels at the scale shown. Overall, there is a slight increase in χ^2 when $\Delta\theta_H$ is not included. On comparison with the bottom graph, it is clear that the inclusion of ΔM_{eff} alters the fit dramatically. Without this parameter, the damping parameter must be increased significantly to minimise χ^2. Fig.6.19 shows that α must be increase to around 0.79 in order to minimise χ^2. Though when the only the intrinsic contribution is included, the minimised fit is highly unsuitable as expected, shown in fig.6.19b.

Before a discussion of the evolution of these parameters as a function of d_{U}, it is important

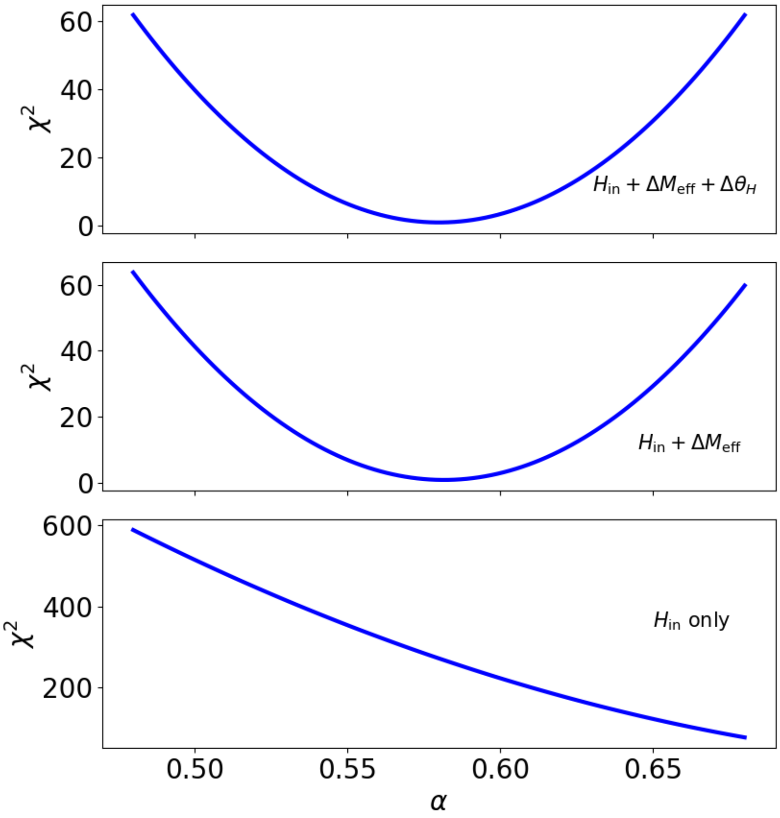

Figure 6.18: χ^2 as parameters are removed from peak-to-peak width fit. Upper panel: χ^2 for a fit containing all required parameters. Middle panel: $\Delta\theta_H = 0$. Bottom panel: Fit containing only the intrinsic contribution.

to mention sample 1321, $d_{\text{U}} = 1.5\,\text{nm}$. When looking at the peak-to-peak width, one half of the data does not display the expected behaviour. The data taken at negative angles displays no apparent pattern, and overall decreases as the samples is rotated towards zero. The positive angle data, however, behaves exactly as expected. Fitting both halves of the data resulted in a large χ^2 with the best fit being judged by eye. This was deemed a poor way of determining the damping, so the fit was constrained to one side of the data, which is shown in fig.6.20. When fitting just one side, χ^2 was reduced from around 8 to 0.052. Due to the fact that only half the data was included in the fit, the resultant errors in the fitting parameters were increased to account for this.

The fitting parameters associated with the extrinsic contribution to the ferromagnetic resonance linewidth can be seen in fig.6.21 for each sample. For ΔM_{eff}, there is an initial drop with the introduction of uranium, though after this point it is roughly linear. This drop is

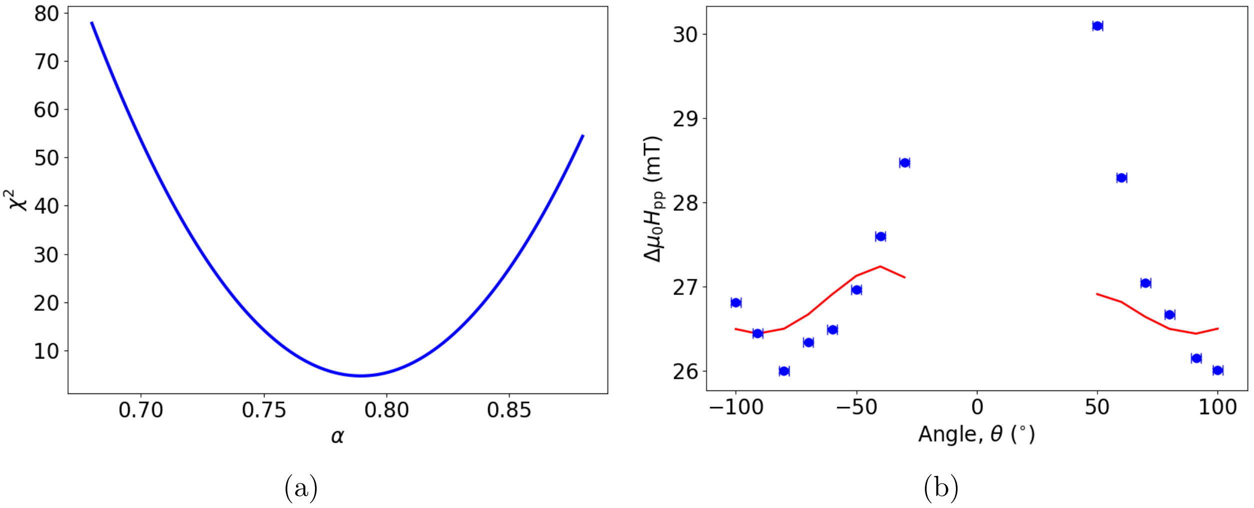

(a) (b)

Figure 6.19: Optimisation of fitting when only the intrinsic contribution is considered. a) χ^2 as a function of α for an H_{in} only fit. α is shifted to much larger values to achieve minimum χ^2 than for a full fit. b) H_{in} only fit to data for samples 1320.

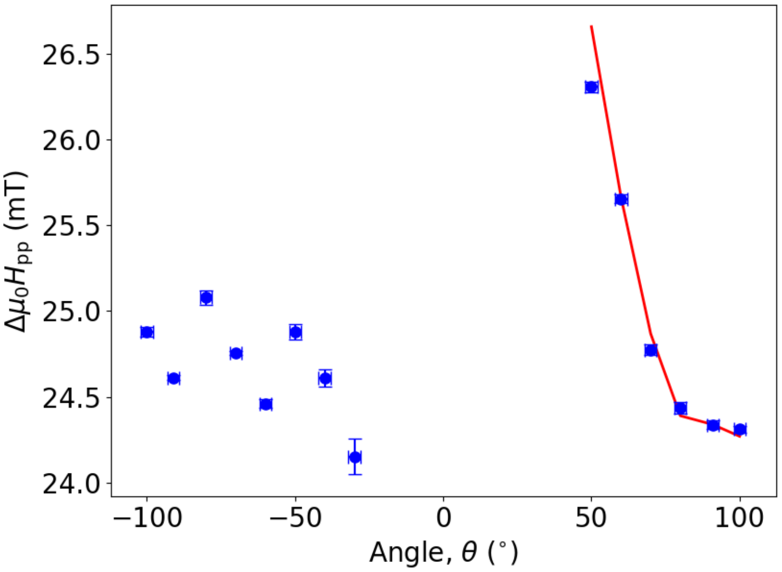

Figure 6.20: Fitting to positive angle peak-to-peak width for $d_{\mathrm{U}} = 1.5\,\mathrm{nm}$. Negative angle data does not follow the expected trend and is excluded from the fit.

most likely from the difference in structure of the films where niobium is and is not in direct contact with the nickel layer. Fluctuations in ΔM_{eff} are generally related to fluctuations in the thickness of the nickel layer [137]. Largely, there is little variation in $\Delta\theta_H$, with the exception of $d_{\mathrm{U}} = 2.9\,\mathrm{nm}$ which is due to the fit trying to compensate for noise in the data for that particular sample. $\Delta\theta_H$ is expected to increase with an increase of the interfacial roughness of the normal metal. From chapter 3, the roughness only shows small variations with d_{U} explaining the mostly linear behaviour of $\Delta\theta_H$ observed here.

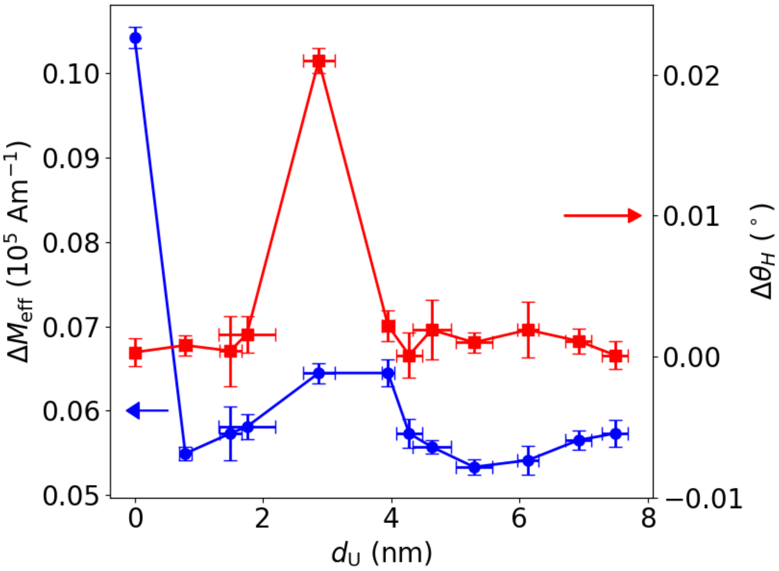

Figure 6.21: ΔM_{eff} (blue circles) and $\Delta\theta_H$ (red squares) taken from fitting the ferromagnetic linewidths of each sample.

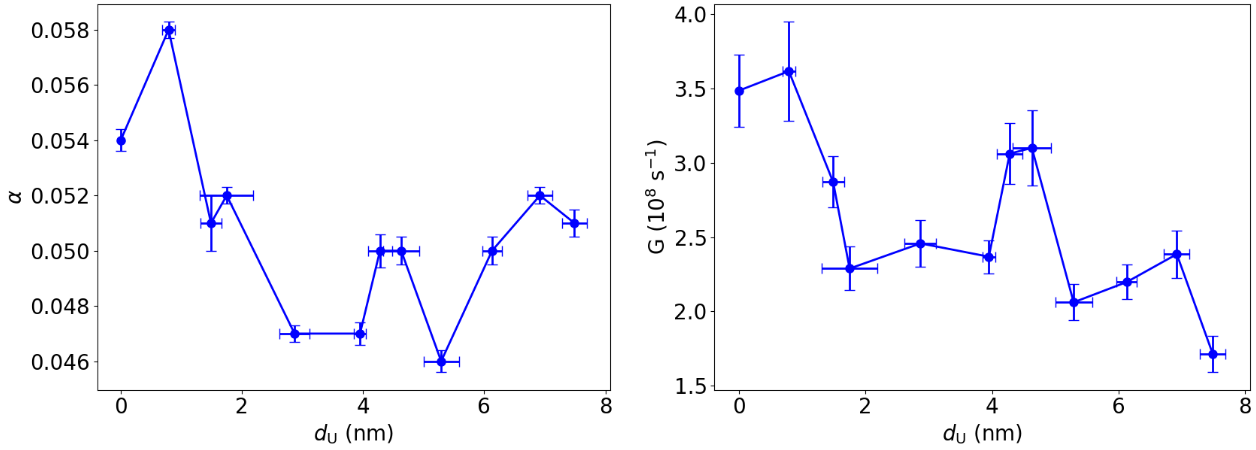

(a) (b)

Figure 6.22: Damping of Ni/U bilayers with increasing d_{U}. Both parameters show oscillations in damping. a) Damping parameter α. b) Gilbert damping parameter G.

The damping parameter α as a function of uranium thickness can be found in fig.6.22a. This has a similar form to the in-plane peak-to-peak widths in fig.6.8. However, unlike in fig.6.8, there appears to be an initial increase in damping when a thin layer of uranium is grown on the nickel. Other variations in the functional form of α in comparison to the in-plane peak-to-peak width may stem from the asymmetry of the linewidth around 0°. Beyond the thinnest U layer there appears to be oscillations in the damping with increasing d_{U} . Therefore, when compared with the form of α it appears that the in-plane peak-to-peak width can provide a reliable first estimate of the damping provided that the systems are of a similar structure.

From α the Gilbert damping coefficient, $\mathrm{G} = \alpha\gamma M_s$, was determined. For this, M_s was taken from the 0° VSM measurement from chapter 6.13. The form of G with d_{U} can be seen in fig.6.22b. G appears to show oscillations with the same periodicity as α. However, over the series, there is an overall decrease in G with thickness. While it is unusual that the form of α does not follow G more closely, this is likely due to non-linear variations in M_s with increasing d_{U} , as seen in fig.6.13b.

Comparing α for Ni/U with Py(=10 nm)/NM(=0.5 nm) films [137], the damping for Ni/U is increased by a factor of ~2. This may be caused by the large Z of the of U. To comment on the SOC, G may be a better comparison as it is dependent on g. For $d_{\mathrm{U}} = 0.6$, the value of G is slightly larger than that of Py(=10 nm)/Pt(=0.5 nm), $\mathrm{G}_{\mathrm{U}} \sim 3.5 \times 10^8$ whereas $\mathrm{G}_{\mathrm{Pt}} \sim 3 \times 10^8$, suggesting that the heavier U layer does cause an increase in damping due to the larger SOC. However, for Ni/Nb it may be expected that α and G would both be significantly lower than for of Ni/U. In comparison with all samples except d_{U} =0.6 nm, α and G are both greater for the Ni/Nb system. The in-plane ΔH_{pp} for samples in this work is about as twice as large that Py(=10 nm)/NM(=0.5 nm) films, even at $d_{\mathrm{U}} = 0$ nm, suggesting that the values of α for all samples are of the correct order. The Ni layer at $d_{\mathrm{U}} = 0$ nm is slightly thicker than for the Ni/U series. The increase in d_{Ni} would be expected to result in a reduction of both damping parameters [137]. It may be that this unexpected enhancement of the damping is a result of interfacial differences between Ni/Nb and Ni/U. If Ni/Nb were to have a greater interface transparency than Ni/U, then more spins would be able to flow into Nb than U. This would result in an increase in damping due to the increased transfer of angular moment. Additionally, there may be formation of a Ni/Nb alloy at the interface. These thin layers of alloys have been found to improved the interface transparency [142]. While alloys of UNi_2 are also expected, the thickness of these layers may be different between Ni/Nb and Ni/U, which may also effect the transparency.

As the Ni layer is a roughly constant thickness across the samples series, the change in damping with d_{U} should arise from the spin pumping across the Ni/U interface and any subsequent scattering. It may be possible that initial variations in the damping are due to changing alloy layers as d_{U} increases but over the complete series these oscillations may be attributed to quantum well states. Work by Montoya *et al.* observed oscillations in the damping due to spin pumping α_{sp} in Fe/Au/Pd systems with increasing d_{Au}. These oscillations were observed over a range of around 20 nm with the two oscillations period of around ~ 0.6 nm and ~ 2 nm [143]. These oscillations periods coincide with the length scales of quantum well state oscillations for k vectors which span different sections of the Au Fermi surface, and are therefore attributed to quantum well states. As QWSs were predicted from both the measurements by VSM and AMR in the previous chapters, it seems most likely that QWSs are responsible for both the oscillations in the perpendicular anisotropy and the damping. Theoretical studies by Mills in ref. [144] attempts to explain the effect of quantum well states on the damping of a ferromagetic/normal metal system. Within the ferromagnet, angular momentum is transferred between the local spins and the conduction electrons. Due to the presence of the normal metal, there are a continuum of states which overlap with the initial spin state band which allows the flip, resulting in an increase of damping [2] [144]. These relative position of these states will alter with the width of the ferromagnetic layer as QWSs alters its DOS. The thickness dependent contribution to the damping was determined to be

$$\Delta G = \frac{\mu_0^2 k_{\uparrow}(E_F) k_{\downarrow}(E_F)}{8\pi^2 \hbar D} f(D), \tag{6.9}$$

where D is the film thickness and $f(D)$ is a dimensionless function which approaches 1 in the thick film limit. It seems that this argument could be easily transferred to QWSs due to increasing overlayer thickness. In this case, the overlap of states will alter on the side of the normal metal.

It is likely that the general decrease in damping with increased thickness is a result of spin backflow from Nb/U interface. If the U layer was capped with a spin sink material, it would be expected that the damping would increase asymptotically with d_{U}, but in the absence of such a material the damping will decrease [143].

---

[2] Though later theoretical studies suggested this interpretation overestimates the oscillation size transition metal band structures, suggesting no significant contribution from QWSs [145], and therefore it is possible that there is another QWSs related mechanism driving the oscillations observed here.

6.4 Conclusion

The full series of Ni/U bilayers were studied using ferromagnetic resonance in order to study the damping induced by the U overlayer. Studying the angular dependence of the resonance field and linewidths of the results FMR curves allowed information about the perpendicular magnetic anisotropy and damping of the samples to be determined. Both the perpendicular anisotropy and the damping parameters appear to oscillate with increasing U thickness. This most likely due to quantum well states within the U layer.

Issues with this analysis come from the limited field range of the MicroESR system. Expanding the field range would allow for more certainty in the fits, particularly for the linewidths. Typically, it has become more common to measure the FMR linewidth at a number of microwave frequencies. The damping parameter α can then be determined using

$$\Delta H_{pp}(\omega) = \alpha \frac{\omega}{\gamma} + \Delta H_{pp}(0), \tag{6.10}$$

where $\Delta H_{pp}(0)$ is the linewidth at $\omega = 0$ [143]. This provides a much simpler analysis which does not require the full angular dependence of the film with respect to the applied field to be measured. This would be a more reliable method given the limited field range accessible. However, a system in which the frequency can be altered is required, which is not within the capabilities of the MicroESR system.

Ideally, Fe/U samples would also be measured using FMR, in order to understand how the presence of an induced magnetic moment affects the spin pumping and the overall damping of the systems. Comparisons with iron would also allow exploration of the effects of strong hybridisation on damping. These samples unfortunately could not be studied as iron did not adhere well to the suprasil, and most likely would require a buffer layer for future studies.

Chapter 7

Alloys

The study of bilayers explored how bulk uranium impacted the magnetic properties of a ferromagnet. The study of dilute alloys can also provide interesting insights and phenomena for spintronics applications, in particular, the extrinsic spin Hall effect. Work by Niimi *et al.* observed that the presence of Ir and Bi in a Cu layer resulted in the extrinsic spin Hall effect, with Ir impurities resulting in a spin Hall angle of 2.1% and CuBi giving -11% [80, 81]

Theoretical studies of $5d$ impurities in copper determined that the spin Hall angle is related to the spin-orbit coupling of the impurity [146, 147], shown in fig.7.1a. However the spin Hall angle, is also dependant on the host element [146]. This dependence can be seen in fig.7.1, which compares the spin Hall angles of impurities in a copper and platinum hosts, fig.7.1a and fig.7.1b respectively. In studies of dilute alloys, it is the "effective SOC" which is important for the SHE, i.e. the difference in SOC between the host and impurity elements [148]. For this reason, large SOC impurities in a large SOC host does not provide a large spin Hall angle. For the study of heavy elements such as uranium, copper is an appropriate choice of host.

While traditionally the spin Hall effect is only associated with non-magnetic materials, there has been experimental evidence of SHE in ferromagnetic materials [149, 150]. In a ferromagnet the mechanisms by which the extrinsic SHE occur are closely linked to those behind the anomalous Hall effect, a phenomenon also strongly dependant on SOC [148]. Theoretical calculations found that in ferromagnetic alloys, magnetic impurities in a non-magnetic host, that the spin Hall angle and anomalous Hall angle followed each other closely, shown in fig.7.2.

The samples investigated in this chapter were grown as part of a collaboration with the Japan Atomic Energy Agency which aims to look at dilute uranium alloys, where uranium impurities were implanted in both copper and nickel hosts[1]. As discussed in section sec:alloy, these samples

---

[1] It should be mentioned that iron was not included in these studies due to the expected presence of proximity

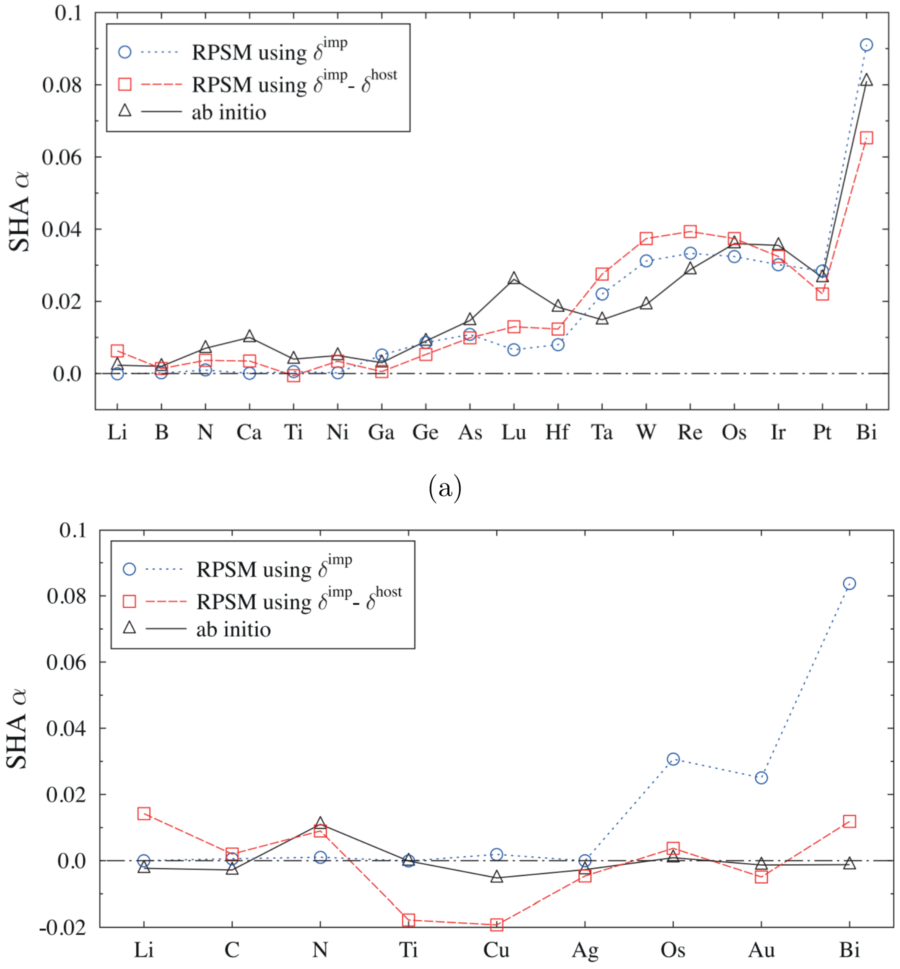

(a)

(b)

Figure 7.1: Calculated spin Hall angle for 1% impurities in a) copper and b) platinum. Taken from ref. [146].

are composed of a) 10 nm Si buffer on glass, 10 nm Ni, 20 nm Cu-U of varying U concentration, and a 10 nm Si cap or b) 10 nm Si buffer on glass, 20 nm Ni-U of varying U concentration, and a 10 nm Si cap. The concentration of uranium in each series was varied from 1 at.% to 12 at.%, as detailed in chapter 3, which was chosen so as to follow the work on Cu-Ir by Niimi *et al.* [80]. The alloy samples were studied using both transport and ferromagnetic resonance measurements. This work is ongoing and the following sections presents preliminary measurements carried out at the University of Bristol which aimed to provide an initial understanding of the transport properties and magnetisation dynamics of these systems, for future comparison with theoretical

---

induced moments.

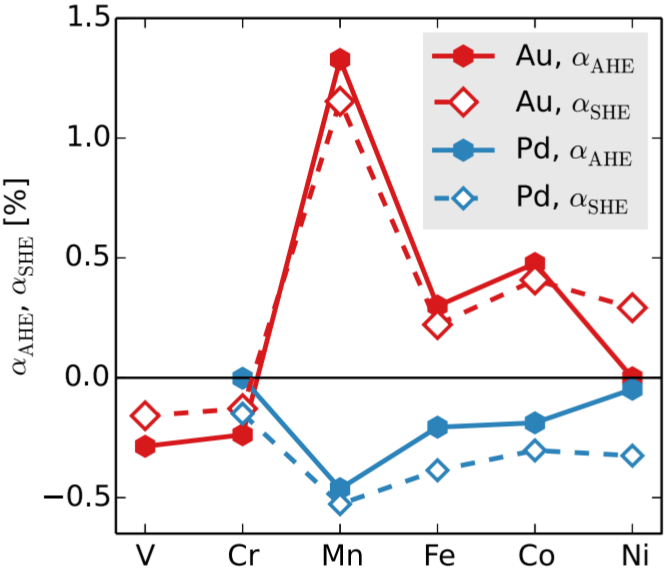

Figure 7.2: Calculations of the spin Hall and anomalous Hall angles for 1% magnetic impurities in Au and Pt hosts. Taken from [148].

studies.

7.1 Transport

Samples were sectioned into 5 mm × 5 mm pieces and secured to the same type of 8-pin DIP adapters used for transport measurements in chapter 5. The samples were then bonded at each corner to allow the resistivity to be determined using the Van der Pauw method at both room temperature and 4 K. In a addition to the Van der Pauw measurements, the resistance of each samples was studied as a function of temperature. This was carried out using a dip-probe lowered into liquid helium.

The purpose of these resistivity measurements was to provide a comparison with theoretical calculations, which can be used to determine the spin Hall resistivity, and subsequently the spin Hall angle, of these dilute U alloys.

The resistivity for the U alloy layers can be seen in fig.7.3. For Cu-U, the initial addition of uranium causes an increase in ρ. However, beyond 6% the resistivity plateaus and possibly dips at 12%. This is mirrored in both the room temperature and 4 K data, with the dip at 12% being more pronounced at 4 K. The presence of uranium in the nickel layer has a very different effect on the resistivity than for Cu-U. In Ni-U, the presence of any uranium results in a large increase in ρ. This stays roughly constant until 12%, where it increases again. Again, this behaviour can be seen in both data sets. However, in the Ni-U case, the 4 K data is initially lower than its room temperature counterpart but there is a crossover around 3% at which it becomes greater.

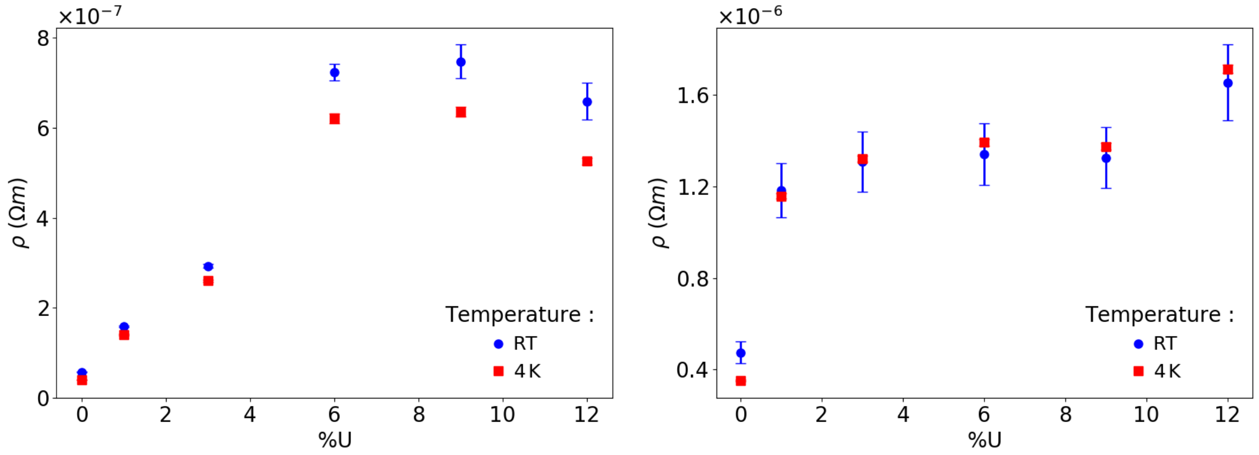

(a) (b)

Figure 7.3: Resistivity as a function of atomic percentage of uranium at both room temperature and 4 K. a) Cu-U systems show a linear increase, followed by a plateau around 6%. b) Ni-U alloys which appears to plateau as U is added.

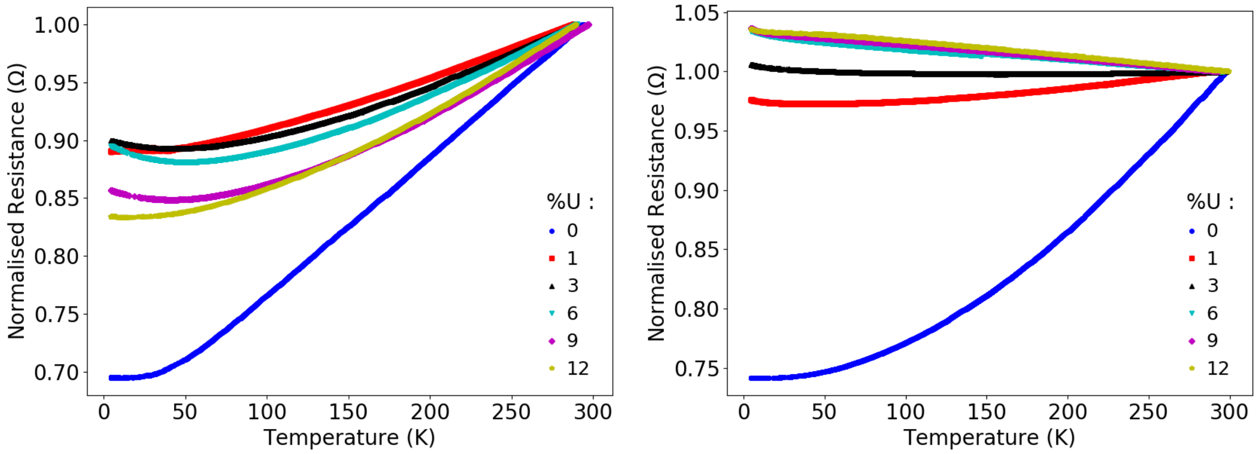

(a) (b)

Figure 7.4: RT measurements normalised to the room temperature resistance of each sample. a) Cu-U samples generally exhibiting the expected metallic behaviour for all U percentages. b) Ni-U alloys appear to transition away from the traditional metallic behaviour above 3%.

Fig.7.4 presents normalised resistance-temperature measurements from room temperature down to 4 K. For most copper samples the behaviour of the resistance as a function of temperature is as expected for a metal, with a slight upturn at in the resistance at low temperature for %U $> 1\%$. This increase is most prominent for 3%, 6%, and 9% but is also visible, though less pronounced, at 12%U. For Ni alloys, the presence of uranium causes the resistivity to increase with decreasing temperature, with up-turns in resistance at low temperatures for all samples, including 0%U. The low temperature behaviour of Cu-U and Ni-U may stem from 2D localisation effects. Given the sheet resistance of both alloy types, shown in fig.7.5, it is mostly likely weak localisation effects which result in the increase in resistance. Weak localisation is caused by quantum interference effects at low temperatures [151]. As a conduction electron travels through the metal, it will be scattered from non-magnetic impurities. In momentum space, the scattering amplitudes for an electron moving from state k in to $-k$ through equal but opposite paths is the same, resulting in an increased probability of the electron being scattered to $-k$. In real space, this is an increased probability for the electron returning to its initial position which translates to an increase in resistance. When spin-orbit impurities are present in the system, weak localisation breaks down as the the amplitude is no longer equal for scattering in opposite directions, which is known as weak anti-localisation. In the Cu-U case, the introduction of low percentages of U may serve only to increase the disorder in the system, resulting in the increase in resistivity due to weak localisation. However, as the U content is increase above 6% it is possible that the spin-orbit coupling of U begins to play a larger role and the system moves towards weak anti-localisation, resulting in the decreased up-turn in resistance. However, it is also possibly that above a certain concentration there is clustering of the U atoms, which may influence the resistance, though the contribution this may make is unclear. By a series of magnetoresistance measurement the presence of weak localisation and anti-localisation could be confirmed. Weak localisation breaks down when a magnetic field is applied perpendicular to the plane of the film, resulting in a negative magnetoresistance. However, weak anti-localisation results in an initial positive magnetoresistance at fields close to zero [151]. Fitting these data allows for the determination of the spin-orbit scattering time τ_{SO} [152].

Weak-localisation can also be present in ferromagnetic films, despite the expectation that the internal magnetic field would result in the destruction of the interference effects responsible [153]. The up-turns in the Ni alloy systems are largely masked by the unusual non-metallic behaviour exhibited at higher temperatures, but the slope of the resistance increase does change at low temperatures, which may be related to weak localisation and anti-localisation, though the distinction between the two may be more difficult to determine. Theoretical studies by Dugaev

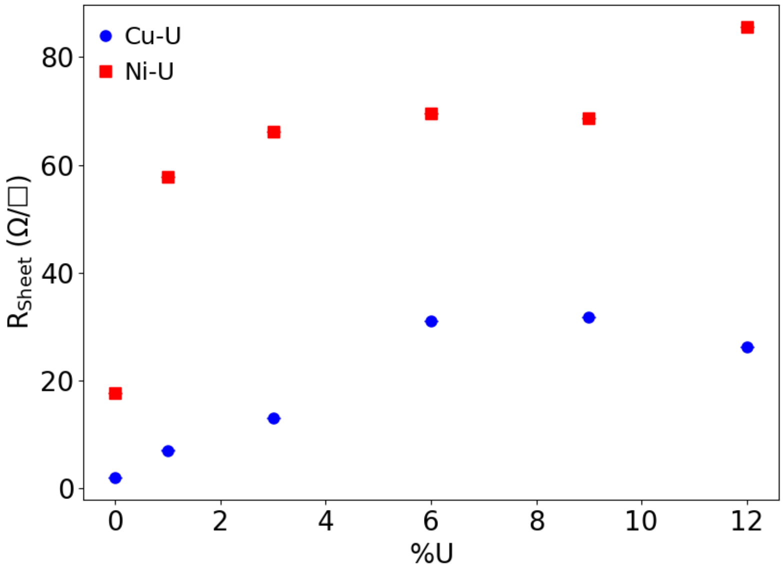

Figure 7.5: Sheet resistance at 4K for both Cu-U (blue circles) and Ni-U (red squares) alloys. For both alloys, these values are within the expected range for weak localisation effects.

et al. determined that the positive magnetoresistance associated with weak anti-localisation due to the presence of spin orbit scattering impurities does not occur in ferromagnets [154]. The origin of increase in resistance for U% > 1% at low temperatures is unclear from the current experimental data. Given the sheet resistance remains of the order of 10 Ω for all U concentrations it is possible that this non-metallic behaviour does not originate from 2D effects. While magnetoresistance measurement may not indicated the presence of weak anti-localisation, they may be useful in understanding the higher temperature behaviour.

7.2 Ferromagnetic Resonance

Ferromagnetic resonace measurements of the alloy samples were carried out in the same MicroESR system used for bilayer studies in chapter 6. The samples were studied in the in-plane orientation to provide initial information about the spin dynamics of these systems.

Fig.7.6 displays a selection of FMR curves for both Cu and Ni hosts. For Cu, fig.7.6a, there is a shift in position with %U. However, these shifts are small, so resonance can be observed for all samples in the series. The Ni host samples exhibit a much larger shift in position with the addition of U, as well an noticeable increase in linewidth. Beyond 1%, resonance could not be accessed with the given field range.

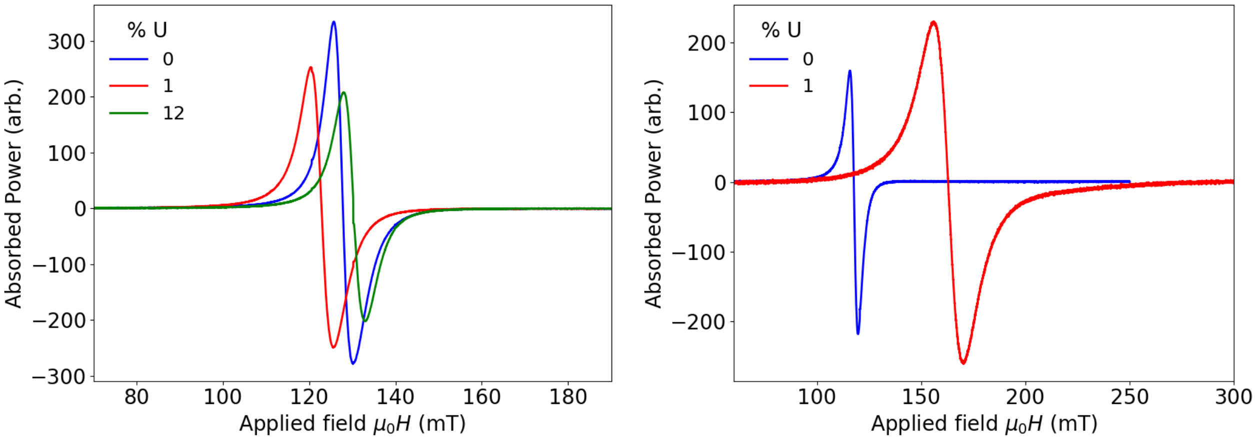

(a)

(b)

Figure 7.6: Raw FMR data for both host element types. a) Cu-U curves for Cu only (blue), 1% (red), and 12% (green). b) FMR curves for Ni only (blue) and 1% U (red). Alloys with U concentration above 1% could not be studied with the MicroESR system due to an insufficient field range.

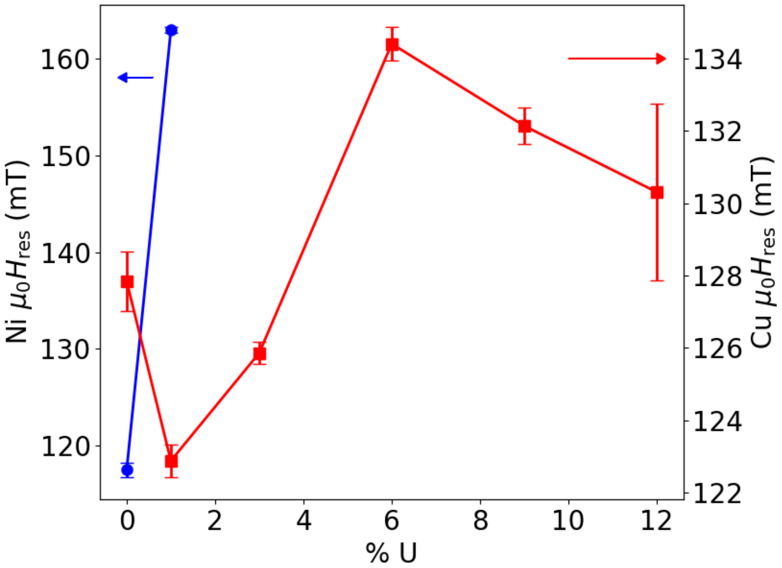

Figure 7.7: Resonance field dependence on %U for both Ni (blue) and Cu (red) alloy samples. The accessible field range was insufficient for Ni samples above 1%. The copper samples exhibit non-monotonic behaviour with uranium percentage

From the available data, the resonance field as function of uranium percentage for both copper and nickel samples can be seen in fig.7.7. As with the bilayer data, the resonance field was determined by a linear fit to the region between the positive and negative absorption peaks.

For the copper sample series, the dependence of $\mu_0 H_{\mathrm{res}}$ on %U appears to be non monotonic, with $\mu_0 H_{\mathrm{res}}$ peaking at 6%. It is possible that the presence of uranium within the copper is altering quantum well states set up in the copper over-layer. As the percentage of uranium is increased, the quantum well states within change or are disrupted and alter the DOS and consequently the magnetic anisotropy of the nickel underlayer.

In Ni-U, the introduction of a small volume of U the resonance field increases by a third. Introducing uranium into the magnetic layer clearly increases the resonance field, and consequently the perpendicular anisotropy field, of the system. It may be that the introduction of uranium dramatically increases the disorder of the system

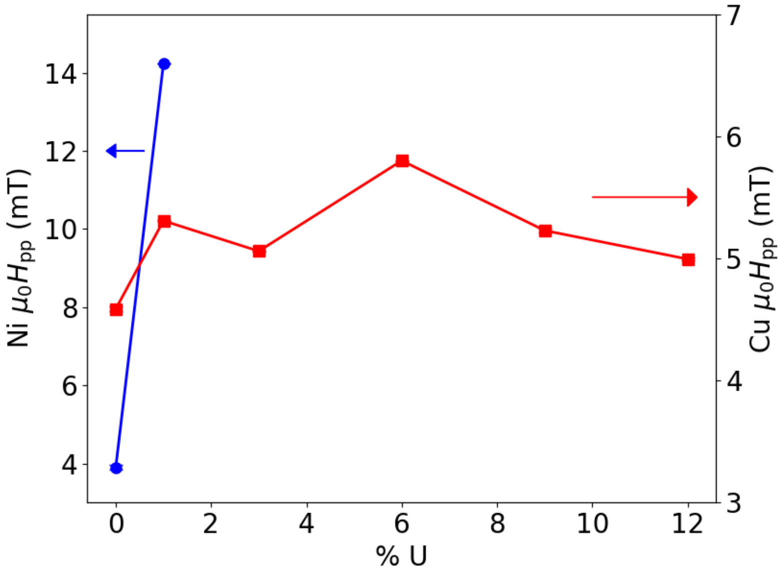

Figure 7.8: Changes in FMR peak-to-peak width as a function of %U for Ni (blue) and Cu (red) alloy samples. For Cu-U this is roughly linear but increases rapidly for Ni.

The peak-to-peak width, which can provide information about the damping of the systems, can be seen in fig.7.8. There appears to be little change in damping across the Cu-U series. There is a slight increase in $\mu_0 H_{\mathrm{pp}}$ from the pure copper system to those containing uranium. The presence of uranium is expected to result in some spin flip scattering, which accounts for the initial broadening, but the further increase in uranium detailed here may not significantly increase the linewidth as concentration is low and therefore the probability of scattering remains low. Small variations in the peak-to-peak width beyond 1% appear to follow the trend set out by the resonance field and may result from QWSs and the altered DOS as discussed. However, the changes in broadening are not significant enough to definitively attribute this behaviour to QWSs and ultimately may be related to minute changes in the magnetic layers for U concentrations >1 at.%.

As with the resonance field, when uranium is introduced into the nickel layer, the peak to peak width increases substantially. The presence of even a small number of uranium atoms clearly disrupts the precession of the magnetisation within the nickel. It is possible that the uranium atoms are acting as a spin sink which results in an increase of damping within the Ni layer. This would be an extrinsic damping contribution as the magnetic layer is no longer homogeneous. Extended field FMR studies would be required to determine the functional form of the in-plane peak-to-peak width, and therefore the damping.

7.3 Conclusions

Dilute Cu-U and Ni-U alloys were studied using transport and ferromagnetic resonance to provide preliminary data for theoretical calculations of the spin Hall angle. From resistance-temperature measurements, both alloy systems shows an increase in resistivity at low temperatures. This behaviour may be a result of weak-localisation. As U is expected to be a large SO scattering impurity, there may also be a weak anti-localisation contribution. The presence of these phenomena should be investigated through magnetoresistance measurements.

However, in addition to the increased low temperature resistance, Ni-U appears to deviate away from metallic behaviour as %U increases. The origin of this behaviour is not well understood and will require subsequent investigations.

The resonance fields of the Cu-U series display non-monotonic behaviour which is likely associated with a changing perpendicular magnetic anisotropy field. This may originate from the inclusion of uranium resulting in a change in QWSs in the Cu layer and therefore altering the Cu DOS and subsequently the DOS of the nickel underlayer. On the other hand, the peak-to-peak width remains relatively constant with increasing U concentration. In contrast, the Ni-U films exhibit a large increase in both the resonance field and the peak-to-peak widths. Both are likely a result of the Ni layers becoming highly disordered with added U impurities.

Chapter 8

Conclusion & Outlook

In this thesis, a series of studies on U/FM and dilute U alloy thin films using magnetometry, transport and ferromagnetic resonance measurements were presented, with main aim of this work to understand and separate the roles of the large spin orbit coupling and induced magnetic moments in heavy metals. Vibrating sample magnetometry measurements in chapter 6.13 show what appear to be oscillations of the effective in-plane magnetic anisotropy in both Fe/U and Ni/U bilayers systems as a function of uranium thickness. These oscillations have been attributed to quantum well states in the uranium overlayers and variations in strength and periodicity between the two sample sets is likely due to the difference in $3d$-$5f$ orbital hybridisation of iron and nickel with uranium. These quantum well states are thought to be independent in origin to the induced magnetic moment observed in Fe/U structures by previous XMCD measurements, but are likely the driving force behind the oscillations of the moment. The suggested presence of these quantum well states is corroborated by the anisotropic magnetoresistance measurements. Typically, QWSs cannot be observed by AMR at room temperature, as illustrated by the Ni/U series, however, oscillations in both the peak position and the anisotropic magnetoresistance were found for the Fe/U series. This is, as with the VSM data, thought to be a result of the strong hybridisation of iron with uranium, in comparison to the weaker hybridisation of nickel and uranium. Though it is possible that in this case the U induced moment also enhances the presence of these oscillations at room temperature. Ferromagnetic resonance measurements found additional periodic behaviour of the perpendicular magnetic anisotropy field and the damping parameters of Ni/U bilayers. Once again, these phenomena are likely driven by quantum well states in the uranium overlayer. The more obvious oscillations in the magnetic properties of these this films at room temperature in comparison with studies of other metals may be a result of the large SOC or the $5f$ electrons associated with U. Further investigation would be required to determine if this is the case. From these results, there is no clear contribution related directly to the spin-orbit coupling, and further exploration would be required to separate the spin-orbit coupling from the proximity induced moment.

Preliminary measurements on dilute uranium alloys provide important information for experimental and theoretical studies of the extrinsic spin Hall effect. These measurements also show evidence of weak localisation and anti-localisation physics. Additionally, Ni-U alloys show an unexpected transition away from metallic behaviour when investigating resistance as a function of temperature.

As this field is largely unexplored, there are a number of directions which could be taken in the future. Exploration through Brillouin light scattering or magnetic imaging techniques on Fe/U samples may shine light on the possibility of interfacial Dzyaloshinskii-Moriya interaction and potential spin textures. Understanding the perpendicular magnetic anisotropy (PMA) changes through further out-of-plane measurements, including angular VSM and FMR, of these sample may also provide new insights into the ferromagnetic thickness limit traditionally required for PMA. Measurements such as spin Hall magnetoresistance or FMR-STT would provide information about the SOC in conjunction with the induced magnetisation, which would help explore the relationship of the two, though these techniques would required nanofabrication. SOC could also be investigated through ARPES, which would provide details of the band structures of these systems. Comparisons with theoretical calculations would then provide a measure of the SOC. However, this technique requires single crystal samples, and therefore an additional and more complex growth process. It may also be of interest to investigate FM/thorium systems. In the case of Th, there is still expected to be a large spin-orbit coupling due to its large Z, but it does not have the same $5f$ character at the Fermi energy. This would allow any contributions from the U $5f$ electrons to be disentangled from those of SOC, and in particular their contribution to quantum well states.

For dilute alloys, experimental investigations into the SHE will be carried out by collaborators at the Japan Atomic Energy Association. However, the low temperature behaviour is also of interest. The localisation behaviour could be examined through low temperature magnetoresistance measurements. It may also be of interest to study the magnetic behaviour of the potentially highly disordered Ni-U systems through VSM or other magnetometry techniques.

Uranium remains a promising candidate for evaluation the the roles of spin-orbit coupling and proximity induced moments for spintronic applications with further investigation. The measurements presented in this work also indicate the presence of interesting and unexpected phenomena which would benefit from more detailed examination.

Bibliography

[1] M. N. Baibich, J. M. Broto, A. Fert, F. Nguyen Van Dau, and F. Petroff. Giant Magnetoresistance of (001)Fe/(001)Cr Magnetic Superlattices. *Physical Review Letters*, 61(21):2472–2475, 1988.

[2] G. Binash, P. Grünberg, F. Saurenbach, and W. Zinn. Enhanced magnetoresistance in layered magnetic structures with antiferromagnetic interlayer exchange. *Physical Review B*, 39(7):4828–4830, 1989.

[3] S. S. P. Parkin, N. More, and K. P. Roche. Oscillations in Exchange Coupling and Magnetoresistance in Metallic Superlattice Structures: Co/Ru, Co/Cr, and Fe/Cr. *Physical Review Letters*, 64(19):2304–2307, 1990.

[4] S. S. P. Parkin, B. Bhadra, and K. P. Roche. Oscillatory Magnetic Exchange Coupling through Thin Copper Layers. *Physical Review Letters*, 66(16):2151–2155, 1991.

[5] S. S. P. Parkin. Systematic Variation of the Strength and Oscillation Period of Indirect Magnetic Exchange Coupling through the $3d$, $4d$, and $5d$ Transition Metals. *Physical Review Letters*, 67(25):3598–3601, 1991.

[6] H. J. G. Draaisma, W. J. M. De Jonge, and F. J. A. Den Broeder. Magnetic interface anisotropy in Pd/Co and Pd/Fe multilayers. *Journal of Magnetism and Magnetic Materials*, 66(3):351–355, 1987.

[7] The Application of Spintronics. `https://www.ibm.com/ibm/history/ibm100/us/en/icons/spintronics/`. Accessed: 2020-01-30.

[8] Toshiba Leads Industry in Bringing Perpendicular Data Recording to HDD–Sets New Record for Storage Capacity With Two New HDDs. `http://www.toshiba.co.jp/about/press/2004_12/pr1401.htm`. Accessed: 2014-02-04.

[9] D. Sander, S. O. Valenzuela, D. Makarov, C. H. Marrows, E. E. Fullerton, P. Fischer, J. McCord, P. Vavassori, S. Mangin, P. Pirro, et al. The 2017 magnetism roadmap. *Journal of Physics D: Applied Physics*, 50(36):363001, 2017.

[10] R. L. Stamps, S. Breitkreutz, J. Åkerman, A. V. Chumak, Y. Otani, G. E. W. Bauer, J.-U. Thiele, M. Bowen, S. A. Majetich, M. Kläui, et al. The 2014 magnetism roadmap. *Journal of Physics D: Applied Physics*, 47(33):333001, 2014.

[11] J. Sinova and I. Žutić. New moves of the spintronics tango. *Nature Materials*, 11(5):368–371, 2012.

[12] S. Y. Huang, X. Fan, D. Qu, Y. P. Chen, W. G. Wang, J. Wu, T. Y. Chen, J. Q. Xiao, and C. L. Chien. Transport Magnetic Proximity Effects in Platinum. *Physical Review Letters*, 109:107204, 2012.

[13] F. Wilhelm, N. Jaouen, A. Rogalev, W. G. Stirling, R. Springell, S. W. Zochowski, A. M. Beesley, S. D. Brown, M. F. Thomas, G. H. Lander, S. Langridge, R. C. C. Ward, and M. R. Wells. X-ray magnetic circular dichroism study of uranium/iron multilayers. *Physical Review B*, 76(024425), 2007.

[14] R. Springell, F. Whilhelm, A. Rogalev, W. G. Stirling, R. C. C. Ward, M. R. Wells, S. Langridge, S. W. Zochowski, and G. H. Lander. Polarization of U $5f$ states in uranium multilayers. *Physical Review B*, 77(064423), 2008.

[15] S. Blundell. *Magnetism in Condensed Matter.* Oxford University Press, 2014.

[16] C. Kittel. *Introduction to Solid State Physics.* Wiley, 8th edition, 2012.

[17] S. Chikazumi. *Physics of Ferromagnetism.* Oxford University Press, 2nd edition, 1999.

[18] A. Aharoni. *Introduction to the Theory of Ferromagnetism.* Oxford University Press, 1998.

[19] F. Brailsford. *Physical Principles of Magnetism.* D. Van Nostrand Company Ltd., 1966.

[20] M. T. Johnson, P. J. H. Bloemen, F. J. A. Den Broeder, and J. J. De Vries. Magnetic anisotropy in metallic multilayers. *Reports on Progress in Physics*, 59(11):1409, 1996.

[21] S. Iwasaki, K. Ouchi, and N. Honda. Studies of the perpendicular magnetization mode in Co-Cr sputtered films. *IEEE Transactions on Magnetics*, 16(5):1111–1113, 1980.

[22] P. F. Carcia, A. D. Meinhaldt, and A. Suna. Perpendicular magnetic anisotropy in Pd/Co thin film layered structures. *Applied Physics Letters*, 47(2):178–180, 1985.

[23] H. J. G. Draaisma, F. J. A. Den Broeder, and W. J. M. De Jonge. Perpendicular anisotropy in Pd/Co multilayers. *Journal of Applied Physics*, 63(8):3479–3481, 1988.

[24] S. Hashimoto, Y. Ochiai, and K. Aso. Perpendicular magnetic anisotropy and magnetostriction of sputtered Co/Pd and Co/Pt multilayered films. *Journal of Applied Physics*, 66:4909–4916, 1989.

[25] G. Lugert and G. Bayreuther. Evidence for perpendicular magnetic anisotropy in Fe (110) epitaxial films in the monolayer range on gold. *Thin Solid Films*, 175:311–316, 1989.

[26] D. O. Smith. Static and dynamic behavior of thin permalloy films. *Journal of Applied Physics*, 29(3):264–273, 1958.

[27] M. Takahashi, D. Watanabe, T. Sasagawa, S. Ogawa, et al. Magnetic Anisotropy of Evaporated Films. I. Iron Films Formed in Magnetic Field. *Journal of the Physical Society of Japan*, 16(10):1913–1923, 1961.

[28] T. G. Knorr and R. W. Hoffman. Dependence of geometric magnetic anisotropy in thin iron films. *Physical Review*, 113(4):1039, 1959.

[29] D. O. Smith, M. S. Cohen, and G. P. Weiss. Oblique-incidence anisotropy in evaporated permalloy films. *Journal of Applied Physics*, 31(10):1755–1762, 1960.

[30] M. Takahashi. Induced magnetic anisotropy of evaporated films formed in a magnetic field. In *Proceedings of the Seventh Conference on Magnetism and Magnetic Materials*, pages 1101–1106. Springer, 1962.

[31] N. Chowdhury and S. Bedanta. Controlling the anisotropy and domain structure with oblique deposition and substrate rotation. *AIP advances*, 4(2):027104, 2014.

[32] B. A. Belyaev, A. V. Izotov, and P. N. Solovev. Competing magnetic anisotropies in obliquely deposited thin permalloy film. *Physica B: Condensed Matter*, 481:86–90, 2016.

[33] I. Dzyaloshinsky. A thermodynamic theory of “weak” ferromagnetism of antiferromagnetics. *Journal of Physics and Chemistry of Solids*, 4(4):241–255, 1958.

[34] T. Moriya. New mechanism of anisotropic superexchange interaction. *Physical Review Letters*, 4(5):228, 1960.

[35] T. Moriya. Anisotropic superexchange interaction and weak ferromagnetism. *Physical Review*, 120(1):91, 1960.

[36] F. Hellman, A. Hoffmann, Y. Tserkovnyak, G. S. D. Beach, E. E. Fullerton, C. Leighton, A. H. MacDonald, D. C. Ralph, D. A. Arena, H. A. Dürr, et al. Interface-induced phenomena in magnetism. *Reviews of Modern Physics*, 89(2):025006, 2017.

[37] M. Belmeguenai, M. S. Gabor, Y. Roussigné, A. Stashkevich, S. M. Chérif, F. Zighem, and C. Tiusan. Brillouin light scattering investigation of the thickness dependence of Dzyaloshinskii-Moriya interaction in $\mathrm{Co}_{0.5}\mathrm{Fe}_{0.5}$ ultrathin films. *Physical Review B*, 93(17):174407, 2016.

[38] M. Belmeguenai, J.-P. Adam, Y. Roussigné, S. Eimer, T. Devolder, J.-V. Kim, S. M. Cherif, A. Stashkevich, and A. Thiaville. Interfacial Dzyaloshinskii-Moriya interaction in perpendicularly magnetized Pt/Co/AlO_x ultrathin films measured by Brillouin light spectroscopy. *Physical Review B*, 91(18):180405, 2015.

[39] K. Di, V. L. Zhang, H. S. Lim, S. C. Ng, M. H. Kuok, J. Yu, J. Yoon, X. Qiu, and H. Yang. Direct observation of the Dzyaloshinskii-Moriya interaction in a Pt/Co/Ni film. *Physical Review Letters*, 114(4):047201, 2015.

[40] A. Hrabec, N. A. Porter, A. Wells, M. J. Benitez, G. Burnell, S. McVitie, D. McGrouther, T. A. Moore, and C. H. Marrows. Measuring and tailoring the Dzyaloshinskii-Moriya interaction in perpendicularly magnetized thin films. *Physical Review B*, 90(2):020402, 2014.

[41] M. Bode, M. Heide, K. Von Bergmann, P. Ferriani, S. Heinze, G. Bihlmayer, A. Kubetzka, O. Pietzsch, S. Blügel, and R. Wiesendanger. Chiral magnetic order at surfaces driven by inversion asymmetry. *Nature*, 447(7141):190, 2007.

[42] S. Heinze, K. Von Bergmann, M. Menzel, J. Brede, A. Kubetzka, R. Wiesendanger, G. Bihlmayer, and S. Blügel. Spontaneous atomic-scale magnetic skyrmion lattice in two dimensions. *Nature Physics*, 7(9):713, 2011.

[43] L. Udvardi and L. Szunyogh. Chiral asymmetry of the spin-wave spectra in ultrathin magnetic films. *Physical Review Letters*, 102(20):207204, 2009.

[44] D. Cortés-Ortuño and P. Landeros. Influence of the Dzyaloshinskii–Moriya interaction on the spin-wave spectra of thin films. *Journal of Physics: Condensed Matter*, 25(15):156001, 2013.

[45] H. T. Nembach, J. M. Shaw, M. Weiler, E. Jué, and T. J. Silva. Linear relation between Heisenberg exchange and interfacial Dzyaloshinskii–Moriya interaction in metal films. *Nature Physics*, 11(10):825, 2015.

[46] S. Tacchi, R. E. Troncoso, M. Ahlberg, G. Gubbiotti, M. Madami, J. Åkerman, and P. Landeros. Interfacial Dzyaloshinskii-Moriya Interaction in Pt/CoFeB films: Effect of the heavy-metal thickness. *Physical Review Letters*, 118:147201, Apr 2017.

[47] J. H. E. Griffiths. Anomalous high-frequency resistance of ferromagnetic metals. *Nature*, 158(4019):670–671, 1946.

[48] C. Kittel. Interpretation of anomalous Larmor frequencies in ferromagnetic resonance experiment. *Physical Review*, 71(4):270, 1947.

[49] C. Kittel. On the theory of ferromagnetic resonance absorption. *Physical Review*, 73(2):155, 1948.

[50] H. Suhl. Ferromagnetic resonance in nickel ferrite between one and two kilomegacycles. *Physical Review*, 97(2):555, 1955.

[51] Y. Tserkovnyak, A. Brataas, and G. E. W. Bauer. Enhanced Gilbert damping in thin ferromagnetic films. *Physical Review Letters*, 88(11):117601, 2002.

[52] A. Brataas, Y. Tserkovnyak, G. E. W. Bauer, and B. I. Halperin. Spin battery operated by ferromagnetic resonance. *Physical Review B*, 66(6):060404, 2002.

[53] S. S. P. Parkin, M. Hayashi, and L. Thomas. Magnetic domain-wall racetrack memory. *Science*, 320(5873):190–194, 2008.

[54] H. Arava, P. M. Derlet, J. Vijayakumar, J. Cui, N. S. Bingham, A. Kleibert, and L. J. Heyderman. Computational logic with square rings of nanomagnets. *Nanotechnology*, 29(26):265205, 2018.

[55] M. Romera, P. Talatchian, S. Tsunegi, F. A. Araujo, V. Cros, P. Bortolotti, J. Trastoy, K. Yakushiji, A. Fukushima, H. Kubota, et al. Vowel recognition with four coupled spin-torque nano-oscillators. *Nature*, 563(7730):230–234, 2018.

[56] A. Fuß, S. Demokritov, P. Grünberg, and W. Zinn. Short-and long period oscillations in the exchange coupling of Fe across epitaxially grown Al-and Au-interlayers. *Journal of Magnetism and Magnetic Materials*, 103(3):L221–L227, 1992.

[57] M. D. Stiles. Interlayer exchange coupling. *Journal of Magnetism and Magnetic Materials*, 200:322–337, 1999.

[58] P. Bruno and C. Chappert. Oscillatory coupling between ferromagnetic layers separated by a nonmagnetic metal spacer. *Physical Review Letters*, 67(12):1602, 1991.

[59] P. Bruno and C. Chappert. Ruderman-Kittel theory of oscillatory interlayer exchange coupling. *Physical Review B*, 46(1):261, 1992.

[60] P. Bruno. Theory of interlayer magnetic coupling. *Physical Review B*, 52(1):411, 1995.

[61] F. J. Himpsel, T. A. Jung, and P. F. Seidler. Electronic states in magnetic nanostructures. *IBM Journal of Research and Development*, 42(1):33–42, 1998.

[62] J. E. Ortega and F. J. Himpsel. Quantum well states as mediators of magnetic coupling in superlattices. *Physical Review Letters*, 69(5):844, 1992.

[63] F. J. Himpsel. Fe on Au (100): Quantum-well states down to a monolayer. *Physical Review B*, 44(11):5966, 1991.

[64] J. W. Knepper and F. Y. Yang. Oscillatory interlayer coupling in Co/ Pt multilayers with perpendicular anisotropy. *Physical Review B*, 71(22):224403, 2005.

[65] M. A. Tomaz, W. J. Antel, W. L. O'Brien, and G. R. Harp. Orientation dependence of interlayer coupling and interlayer moments in Fe/Cr multilayers. *Physical Review B*, 55(6):3716, 1997.

[66] M. Cinal. Analysis of magnetocrystalline anisotropy oscillations in Co/Pd thin films. *Journal of Physics: Condensed Matter*, 13(5):901, 2001.

[67] P. Bruno. Interlayer exchange coupling: a unified physical picture. *Journal of Magnetism and Magnetic Materials*, 121(1-3):248–252, 1993.

[68] P. Bruno. Oscillations of interlayer exchange coupling vs. ferromagnetic-layers thickness. *EPL (Europhysics Letters)*, 23(8):615, 1993.

[69] M. Przybylski, M. Dąbrowski, U. Bauer, M. Cinal, and J. Kirschner. Oscillatory magnetic anisotropy due to quantum well states in thin ferromagnetic films (invited). *Journal of Applied Physics*, 111(7):07C102, 2012.

[70] S. Manna, P. L. Gastelois, M. Dąbrowski, P. Kuświk, M. Cinal, M. Przybylski, and J. Kirschner. Effect of quantum well states in Cu overlayer on magnetic anisotropy of Fe and Co films revisited. *Physical Review B*, 87(13):134401, 2013.

[71] Ch. Würsch, C. Stamm, S. Egger, D. Pescia, W. Baltensperger, and J.S. Helman. Quantum oscillations in a confined electron gas. *Nature*, 389(6654):937, 1997.

[72] J. Li, M. Przybylski, F. Yildiz, X. D. Ma, and Y. Z. Wu. Oscillatory magnetic anisotropy originating from quantum well states in Fe films. *Physical Review Letters*, 102(20):207206, 2009.

[73] J. Li, M. Przybylski, Y. He, and Y. Z. Wu. Experimental observation of quantum oscillations of perpendicular anisotropy in Fe films on Ag (1,1,10). *Physical Review B*, 82(21):214406, 2010.

[74] Y. Dahmane, C. Arm, S. Auffret, U. Ebels, B. Rodmacq, and B. Dieny. Oscillatory behavior of perpendicular magnetic anisotropy in Pt/Co/Al(O_x) films as a function of Al thickness. *Applied Physics Letters*, 95(22):222514, 2009.

[75] Y. Tserkovnyak, A. Brataas, G. E. W. Bauer, and B. I. Halperin. Nonlocal magnetization dynamics in ferromagnetic heterostructures. *Reviews of Modern Physics*, 77(4):1375, 2005.

[76] D. C. Ralph and M. D. Stiles. Spin transfer torques. *Journal of Magnetism and Magnetic Materials*, 320(7):1190–1216, 2008.

[77] J. Sinova, S. O. Valenzuela, J. Wunderlich, C. H. Back, and T. Jungwirth. Spin Hall effects. *Reviews of Modern Physics*, 87(4):1213, 2015.

[78] J. E. Hirsch. Spin Hall effect. *Physical Review Letters*, 83(9):1834, 1999.

[79] S. Maekawa, S.O. Valenzuela, E. Saitoh, and T. Kimura. *Spin Current*, volume 22. Oxford University Press, 2017.

[80] Y. Niimi, M. Morota, D. H. Wei, C. Deranlot, M. Basletic, A. Hamzic, A. Fert, and Y. Otani. Extrinsic spin hall effect induced by iridium impurities in copper. *Physical Review Letters*, 106:126601, 2011.

[81] Y. Niimi, Y. Kawanishi, D. H. Wei, C. Deranlot, H. X. Yang, M. Chshiev, T. Valet, A. Fert, and Y. Otani. Giant spin hall effect induced by skew scattering from bismuth impurities inside thin film CuBi alloys. *Physical Review Letters*, 109:156602, 2012.

[82] C.-F. Pai, L. Liu, Y. Li, H. W. Tseng, D. C. Ralph, and R. A. Buhrman. Spin transfer torque devices utilizing the giant spin Hall effect of tungsten. *Applied Physics Letters*, 101(12):122404, 2012.

[83] E. Sagasta, Y. Omori, M. Isasa, M. Gradhand, L. E. Hueso, Y. Niimi, Y. Otani, and F. Casanova. Tuning the spin Hall effect of Pt from the moderately dirty to the superclean regime. *Physical Review B*, 94(6):060412, 2016.

[84] A. Hoffmann. Spin Hall effects in metals. *IEEE Transactions on Magnetics*, 49(10):5172–5193, 2013.

[85] L. Liu, T. Moriyama, D. C. Ralph, and R. A. Buhrman. Spin-torque ferromagnetic resonance induced by the spin Hall effect. *Physical Review Letters*, 106(3):036601, 2011.

[86] H. Nakayama, M. Althammer, Y.-T. Chen, K. Uchida, Y. Kajiwara, D. Kikuchi, T. Ohtani, S. Geprägs, M. Opel, S. Takahashi, et al. Spin Hall magnetoresistance induced by a nonequilibrium proximity effect. *Physical Review Letters*, 110(20):206601, 2013.

[87] Y. K. Kato, R. C. Myers, A. C. Gossard, and D. D. Awschalom. Observation of the spin Hall effect in semiconductors. *Science*, 306(5703):1910–1913, 2004.

[88] L. Liu, C.-F. Pai, Y. Li, H. W. Tseng, D. C. Ralph, and R. A. Buhrman. Spin-torque switching with the giant spin Hall effect of tantalum. *Science*, 336(6081):555–558, 2012.

[89] T. Funk, A. Deb, S. J. George, H. Wang, and S. P. Cramer. X-ray magnetic circular dichroism—a high energy probe of magnetic properties. *Coordination Chemistry Reviews*, 249(1-2):3–30, 2005.

[90] F. Wilhelm, P. Poulopoulos, G. Ceballos, H. Wende, K. Baberschke, P. Srivastava, D. Benea, H. Ebert, M. Angelakeris, N. K. Flevaris, et al. Layer-resolved magnetic moments in Ni/Pt multilayers. *Physical Review Letters*, 85(2):413, 2000.

[91] M. G. Samant, J. Stöhr, S. S. P. Parkin, G. A. Held, B. D. Hermsmeier, F. Herman, M. Van Schilfgaarde, L.-C. Duda, D. C. Mancini, N. Wassdahl, et al. Induced spin polarization in Cu spacer layers in Co/Cu multilayers. *Physical Review Letters*, 72(7):1112, 1994.

[92] G. A. Held, M. G. Samant, J. Stöhr, S. S. P. Parkin, B. Do Hermsmeier, M. van Schilfgaarde, and R. Nakajimas. X-ray magnetic circular dichroism study of the induced spin polarization of Cu in Co/Cu and Fe/Cu multilayers. *Zeitschrift für Physik B Condensed Matter*, 100(3):335–341, 1997.

[93] N. Nakajima, T. Koide, T. Shidara, H. Miyauchi, H. Fukutani, A. Fujimori, K. Iio, T. Katayama, M. Nŷvlt, and Y. Suzuki. Perpendicular magnetic anisotropy caused by interfacial hybridization via enhanced orbital moment in Co/Pt multilayers: Magnetic circular x-ray dichroism study. *Physical Review Letters*, 81(23):5229, 1998.

[94] W. J. Antel Jr, M. M. Schwickert, Tao Lin, W. L. O'Brien, and G. R. Harp. Induced ferromagnetism and anisotropy of Pt layers in Fe/Pt (001) multilayers. *Physical Review B*, 60(18):12933, 1999.

[95] F. Wilhelm, P. Poulopoulos, H. Wende, A. Scherz, K. Baberschke, M. Angelakeris, N. K. Flevaris, and A. Rogalev. Systematics of the induced magnetic moments in $5d$ layers and the violation of the third Hund's rule. *Physical Review Letters*, 87(20):207202, 2001.

[96] T. Kikkawa, M. Suzuki, J. Okabayashi, K. Uchida, D. Kikuchi, . Qiu, and E. Saitoh. Detection of induced paramagnetic moments in Pt on $Y_3Fe_5O_{12}$ via x-ray magnetic circular dichroism. *Physical Review B*, 95(21):214416, 2017.

[97] J. Okabayashi, T. Koyama, M. Suzuki, M. Tsujikawa, M. Shirai, and D. Chiba. Induced perpendicular magnetization in a Cu layer inserted between Co and Pt layers revealed by x-ray magnetic circular dichroism. *Scientific Reports*, 7:46132, 2017.

[98] H. Yamada, J. Inoue, K. Terao, S. Kanda, and M. Shimizu. Electronic structure and magnetic properties of YM2 compounds (M= Mn, Fe, Co and Ni). *Journal of Physics F: Metal Physics*, 14(8):1943, 1984.

[99] G. H. Lander, E. S. Fisher, and S. D. Bader. The solid-state properties of uranium a historical perspective and review. *Advances in Physics*, 43(1):1–111, 1994.

[100] R. Springell, B. Detlefs, G. H. Lander, R. C. C. Ward, R. A. Cowley, N. Ling, W. Goetze, R. Ahuja, W. Luo, and B. Johansson. Elemental engineering: Epitaxial uranium thin films. *Physical Review B*, 78(19):193403, 2008.

[101] S. Singh, M. Anguera, E. del Barco, R. Springell, and C. W. Miller. Moderate positive spin Hall angle in uranium. *Applied Physics Letters*, 107(23):232403, 2015.

[102] K. T. Moore and G. van der Laan. Nature of the $5f$ states in actinide metals. *Reviews of Modern Physics*, 81(1):235, 2009.

[103] N. Stojić, J. W. Davenport, M. Komelj, and J. Glimm. Surface magnetic moment in α-uranium by density-functional theory. *Physical Review B*, 68(9):094407, 2003.

[104] S. D. Brown, A. Beesley, A. Herring, D. Mannix, M. F. Thomas, P. Thompson, L. Bouchenoire, S. Langridge, G. H. Lander, W. G. Stirling, et al. Resonant magnetic reflectivity from U/Fe multilayers. *Journal of Applied Physics*, 93(10):6519–6521, 2003.

[105] S. D. Brown, L. Bouchenoire, P. Thompson, R. Springell, A. Mirone, W. G. Stirling, A. Beesley, M. F. Thomas, R. C. C. Ward, M. R. Wells, et al. Profile of the U $5f$ magnetization in U/Fe multilayers. *Physical Review B*, 77(1):014427, 2008.

[106] L. Severin, L. Nordström, M. S. S. Brooks, and B. Johansson. Theoretical study of the ferromagnetism in UNi_2. *Physical Review B*, 44(17):9392, 1991.

[107] O. Hellwig, G. Song, H. Zabel, H. W. Becker, and A. Birkner. Oxidation of epitaxial Nb (110) films on a-plane sapphire substrates: An x-ray study. *Materialwissenschaft und Werkstofftechnik: Materials Science and Engineering Technology*, 31(9):856–859, 2000.

[108] M. Björck. GenX V2.4.9. `http://genx.sourceforge.net/`, 2008–2018.

[109] M. Björck and G. Andersson. *GenX*: an extensible X-ray reflectivity refinement program utilizing differential evolution. *Journal of Applied Crystallography*, 40(6):1174–1178, Dec 2007.

[110] L. G. Parratt. Surface studies of solids by total reflection of x-rays. *Physical Review*, 95(2):359, 1954.

[111] R. Springell. *Growth and characterisation of uranium multilayers.* PhD thesis, University of London, 2008.

[112] J. Als-Nielson and D. McMorrow. *Elements of Modern X-ray Physics.* Wiley, Second edition, 2011.

[113] H. P. Myers. *Introductory Solid State Physics.* CRC Press, 1997.

[114] W. T. Eeles and A. L. Sutton. X-ray determination of the atomic positions in α-uranium at 22°C and 600°C. *Acta Crystallographica*, 16(6):575–575, 1963.

[115] A. M. Beesley, M. F. Thomas, A. D. F. Herring, R. C. C. Ward, M. R. Wells, S. Langridge, S. D. Brown, S. W. Zochowski, L. Bouchenoire, W. G. Stirling, et al. Magnetism of uranium/iron multilayers: I. Fabrication and characterization. *Journal of Physics: Condensed Matter*, 16(47):8491, 2004.

[116] R. Springell, S. W. Zochowski, R. C. C. Ward, M. R. Wells, S. D. Brown, L. Bouchenoire, F. Wilhelm, S. Langridge, W. G. Stirling, and G. H. Lander. A study of uranium-based multilayers: I. fabrication and structural characterization. *Journal of Physics: Condensed Matter*, 20(21):215229, 2008.

[117] S. Foner. Vibrating sample magnetometer. *Review of Scientific Instruments*, 27(7):548–548, 1956.

[118] S. Foner. Versatile and sensitive vibrating-sample magnetometer. *Review of Scientific Instruments*, 30(7):548–557, 1959.

[119] A. Zieba and S. Foner. Detection coil, sensitivity function, and sample geometry effects for vibrating sample magnetometers. *Review of Scientific Instruments*, 53(9):1344–1354, 1982.

[120] Y.-P. Zhao, R. M. Gamache, G.-C. Wang, T.-M. Lu, G. Palasantzas, and J. Th. M. De Hosson. Effect of surface roughness on magnetic domain wall thickness, domain size, and coercivity. *Journal of Applied Physics*, 89(2):1325–1330, 2001.

[121] M.-H. Wu and M. Gradhand. Personal Communication.

[122] B. N. Engel, C. D. England, R. A. Van Leeuwen, M. H. Wiedmann, and C. M. Falco. Interface magnetic anisotropy in epitaxial superlattices. *Physical Review Letters*, 67:1910–1913, Sep 1991.

[123] K.-S. Ryu, S.-H. Yang, L. Thomas, and S. S. P. Parkin. Chiral spin torque arising from proximity-induced magnetization. *Nature Communications*, 5:3910, 2014.

[124] H. Yang, A. Thiaville, S. Rohart, A. Fert, and M. Chshiev. Anatomy of Dzyaloshinskii-Moriya interaction at Co/Pt interfaces. *Physical Review Letters*, 115(26):267210, 2015.

[125] R. M. Rowan-Robinson, A. A. Stashkevich, Y. Roussigné, M. Belmeguenai, S.-M. Chérif, A. Thiaville, T. P. A. Hase, A. T. Hindmarch, and D. Atkinson. The interfacial nature of proximity-induced magnetism and the Dzyaloshinskii-Moriya interaction at the Pt/Co interface. *Scientific Reports*, 7(1):16835, 2017.

[126] A. Belabbes, G. Bihlmayer, F. Bechstedt, S. Blügel, and A. Manchon. Hund's Rule-Driven Dzyaloshinskii-Moriya Interaction at $3d$-$5d$ Interfaces. *Physical Review Letters*, 117(24):247202, 2016.

[127] T. R. McGuire and R. I. Potter. Anisotropic Magnetoresistance in Ferromagnetic $3d$ Alloys. *IEEE Transactions on Magnetics*, 11(4):1018–1038, 1975.

[128] J. Smit. Magnetoresistance of ferromagnetic metals and alloys at low temperatures. *Physica*, 17(6):612–627, 1951.

[129] R. I. Potter. Magnetoresistance anisotropy in ferromagnetic NiCu alloys. *Physical Review B*, 10(11):4626, 1974.

[130] R. P. Van Gorkom, J. Caro, T. M. Klapwijk, and S. Radelaar. Temperature and angular dependence of the anisotropic magnetoresistance in epitaxial Fe films. *Physical Review B*, 63(13):134432, 2001.

[131] M. B. Brodsky, N. J. Griffin, and M. D. Odie. Electrical Resistivity of Alpha Uranium at Low Temperatures. *Journal of Applied Physics*, 40(2):895–897, 1969.

[132] S. S.-L. Zhang, G. Vignale, and S. Zhang. Anisotropic magnetoresistance driven by surface spin-orbit scattering. *Physical Review B*, 92(2):024412, 2015.

[133] J. Aarts, C. Attanasio, C. Bell, C. Cirillo, M. Flokstra, and J. M. vd Knaap. Superconductor/ferromagnet hybrids: bilayers and spin switching. In *Nanoscience and Engineering in Superconductivity*, pages 323–347. Springer, 2010.

[134] Y. S. Gui, N. Mecking, A. Wirthmann, L. H. Bai, and C.-M. Hu. Electrical detection of the ferromagnetic resonance: Spin-rectification versus bolometric effect. *Applied Physics Letters*, 91(8):082503, 2007.

[135] J. X. Li, M. W. Jia, Z. Ding, J. H. Liang, Y. M. Luo, and Y. Z. Wu. Pt-enhanced anisotropic magnetoresistance in Pt/Fe bilayers. *Physical Review B*, 90(21):214415, 2014.

[136] J. X. Li, M. W. Jia, L. Sun, Z. Ding, B. L. Chen, and Y. Z. Wu. Oscillatory anisotropic magnetoresistance arising from quantum well states in Au/Fe (001) bilayers. *IEEE Magnetics Letters*, 6:1–4, 2015.

[137] S. Mizukami, Y. Ando, and T. Miyazaki. The study on ferromagnetic resonance linewidth for NM/80NiFe/NM (NM = Cu, Ta, Pd and Pt) films. *Japanese Journal of Applied Physics*, 40(2R):580, 2001.

[138] S. Mizukami, Y. Ando, and T. Miyazaki. Effect of spin diffusion on Gilbert damping for a very thin permalloy layer in Cu/permalloy/Cu/Pt films. *Physical Review B*, 66:104413, 2002.

[139] C. Bell, S. Milikisyants, M. Huber, and J. Aarts. Spin Dynamics in a Superconductor-Ferromagnet Proximity System. *Physical Review Letters*, 100:047002, 2008.

[140] W. S. Ament and G. T. Rado. Electromagnetic effects of spin wave resonance in ferromagnetic metals. *Physical Review*, 97(6):1558, 1955.

[141] C. Chappert, K. Le Dang, P. Beauvillain, H. Hurdequint, and D. Renard. Ferromagnetic resonance studies of very thin cobalt films on a gold substrate. *Physical Review B*, 34(5):3192, 1986.

[142] L. Zhu, D. C. Ralph, and R. A. Buhrman. Enhancement of spin transparency by interfacial alloying. *Physical Review B*, 99(18):180404, 2019.

[143] E. Montoya, B. Heinrich, and E. Girt. Quantum well state induced oscillation of pure spin currents in Fe/Au/Pd (001) systems. *Physical Review Letters*, 113(13):136601, 2014.

[144] D. L. Mills. Ferromagnetic resonance relaxation in ultrathin metal films: The role of the conduction electrons. *Physical Review B*, 68(1):014419, 2003.

[145] M. Zwierzycki, Y. Tserkovnyak, P. J. Kelly, A. Brataas, and G. E. W. Bauer. First-principles study of magnetization relaxation enhancement and spin transfer in thin magnetic films. *Physical Review B*, 71(6):064420, 2005.

[146] A. Johansson, C. Herschbach, D. V. Fedorov, M. Gradhand, and I. Mertig. Validity of the relativistic phase shift model for the extrinsic spin hall effect in dilute metal alloys. *Journal of Physics: Condensed Matter*, 26(27):274207, 2014.

[147] C. Herschbach, D. V. Fedorov, I. Mertig, M. Gradhand, K. Chadova, H. Ebert, and D. Ködderitzsch. Insight into the skew-scattering mechanism of the spin Hall effect: Potential scattering versus spin-orbit scattering. *Physical Review B*, 88(20):205102, 2013.

[148] B. Zimmermann, K. Chadova, D. Ködderitzsch, S. Blügel, H. Ebert, D. V. Fedorov, N. H. Long, P. Mavropoulos, I. Mertig, Y. Mokrousov, et al. Skew scattering in dilute ferromagnetic alloys. *Physical Review B*, 90(22):220403, 2014.

[149] D. H. Wei, Y. Niimi, B. Gu, T. Ziman, S. Maekawa, and Y. Otani. The spin Hall effect as a probe of nonlinear spin fluctuations. *Nature Communications*, 3(1):1–5, 2012.

[150] B. F. Miao, S. Y. Huang, D. Qu, and C. L. Chien. Inverse spin hall effect in a ferromagnetic metal. *Physical Review Letters*, 111(6):066602, 2013.

[151] G. Bergmann. Weak localization in thin films: a time-of-flight experiment with conduction electrons. *Physics Reports*, 107(1):1–58, 1984.

[152] S. Maekawa and H. Fukuyama. Magnetoresistance in two-dimensional disordered systems: effects of Zeeman splitting and spin-orbit scattering. *Journal of the Physical Society of Japan*, 50(8):2516–2524, 1981.

[153] R. Misra, A. F. Hebard, K. A. Muttalib, and P. Wölfle. Spin-wave-mediated quantum corrections to the conductivity of thin ferromagnetic films of gadolinium. *Physical Review B*, 79(14):140408, 2009.

[154] V. K. Dugaev, P. Bruno, and J. Barnaś. Weak localization in ferromagnets with spin-orbit interaction. *Physical Review B*, 64(14):144423, 2001.